Electrochemical Energy Reviews (2020) 3:286–343
https://doi.org/10.1007/s41918-020-00064-5

REVIEW ARTICLE

Defect Engineering in Titanium-Based Oxides for Electrochemical Energy Storage Devices

Zhong Su[1] · Jiahua Liu[2] · Meng Li[1] · Yuxuan Zhu[1] · Shangshu Qian[1] · Mouyi Weng[2] · Jiaxin Zheng[2] · Yulin Zhong[1] · Feng Pan[2] · Shanqing Zhang[1]

Received: 6 August 2019 / Revised: 28 September 2019 / Accepted: 20 January 2020 / Published online: 28 February 2020

Abstract

Defect engineering involves the manipulation of the type, concentration, mobility or spatial distribution of defects within crystalline structures and can play a pivotal role in transition metal oxides in terms of optimizing electronic structure, conductivity, surface properties and mass ion transport behaviors. And of the various transition metal oxides, titanium-based oxides have been keenly investigated due to their extensive application in electrochemical storage devices in which the atomic-scale modification of titanium-based oxides involving defect engineering has become increasingly sophisticated in recent years through the manipulation of the type, concentration, spatial distribution and mobility of defects. As a result, this review will present recent advancements in defect-engineered titanium-based oxides, including defect formation mechanisms, fabrication strategies, characterization techniques, density functional theory calculations and applications in energy conversion and storage devices. In addition, this review will highlight trends and challenges to guide the future research into more efficient electrochemical storage devices.

Keywords Defect engineering · Ti-based oxides · Optimized intrinsic properties · Electrochemical energy storage

1 Introduction

The increasing prominence of local and global environmental challenges has stimulated growing demand for clean, renewable energy sources [1, 2]. To address this demand, electrochemical energy conversion and storage devices have been recognized as ideal alternatives to traditional fossil fuels because they are environmentally friendly, inexpensive, portable and scalable [3, 4]. And of these devices, lithium-ion batteries [5–7], metal-ion (Na^+, Mg^{2+} and Al^{3+}) batteries [8, 9] and electrochemical supercapacitors [10, 11] have all become significant energy storage systems that have been successfully applied in portable devices. However, these systems often suffer from low energy storage efficiency and struggle to meet the demands of high energy-consuming devices such as electric and hybrid electric vehicles. To address these problems, great efforts have been devoted to developing low-cost novel oxide nanomaterials to improve electrochemical energy storage performance metrics such as energy density, power density and cycle life spans. And among various oxides, Ti-based oxides have been extensively studied as multifunctional materials for electrochemical energy storage devices [12, 13] as well as for water splitting, solar cells, hydrogen energy and rechargeable battery/supercapacitor applications due to their natural abundance, lack of toxicity and low costs [14–17].

As an important class of Ti-based oxides, titanium dioxide (TiO_2) has attracted extensive attention as an important semiconductor material after being initially reported by Fujishima et al. [18] for water splitting in which anatase, rutile, brookite and TiO_2(B) (bronze) all show potential in electrochemical energy storage applications regardless of being in bulk or nanostructured forms [19–26]. In addition, anatase and bronze phases are more electrochemically

Zhong Su and Jiahua Liu have contributed equally to this work.

✉ Feng Pan
panfeng@pkusz.edu.cn

✉ Shanqing Zhang
s.zhang@griffith.edu.au

1 Centre for Clean Environment and Energy, School of Environment and Science, Griffith University, Gold Coast Campus, Gold Coast, QLD 4222, Australia

2 School of Advanced Materials, Peking University Shenzhen Graduate School, Shenzhen 518055, Guangdong, China

active for Li^+ intercalation due to their open crystal structure and low Li^+ diffusion energy barrier. However, TiO_2 also suffers from poor electron and Li^+ conductivity and tends to display large polarization, irreversible capacity loss and poor cyclic stability. Here, researchers suggest that higher specific surface areas, nanoparticle sizes and special nanostructures can alleviate these issues. For example, Li et al. [27] synthesized TiO_2(B) nanowires with an ultrahigh surface area of 210 $m^2\ g^{-1}$ through a facile hydrothermal route and reported that rapid Li^+ insertion/extraction can be achieved if the nanowires were used as anodes in LIBs in which high BET surface areas can provide larger reaction areas and promote charge transfer and collection, thus increasing battery rate performance. In another example, Rai et al. [28] prepared extremely small TiO_2 nanoparticles (8.6 nm) through a simple urea-assisted auto-combustion synthesis method under different calcination temperatures and reported that the resulting small particle size was able to provide a larger contact surface area with the electrolyte to enhance Li^+ de-intercalation and therefore improve Li storage capability. Aside from these examples, an array of TiO_2 nanostructures including 0D nanoparticles [14], 1D nanowires and nanotubes [29], 2D nanosheets [30] and 3D hierarchical structures [31] have also been investigated over the years with studies ranging from preparation techniques and material characterizations to implementation in energy storage applications, resulting in outstanding electrochemical performances due to large reaction areas and rapid Li^+ transport pathways as provided by corresponding nanostructures. (The methods to construct nanostructures and composite materials to enhance the conductivity, reaction area and Li^+ transport in electrode materials have been discussed and reviewed). Despite these promising results however, fundamental drawbacks of TiO_2 such as slow charge carrier transfer rates and wide band gaps (3.2 eV) remain unchanged and seriously hinder development and application [32].

As another important class of Ti-based oxides, $Li_4Ti_5O_{12}$ (LTO) is widely considered to be a promising anode material in Li batteries due to its structural stability with "zero strain" in its lattice parameter during charge/discharge [33–35] and a higher flat Li insertion/extraction potential at ~ 1.55 V, which enhances safety in LTO-based LIBs by avoiding Li dendrite formation. In addition, wide operating temperatures and high reversibility make LTO practical in various energy storage systems. And as a result of these desirable characteristics, LTO-based LIBs have been successfully commercialized and applied to portable energy storage devices. Despite this, the further development of LTO in LIBs is severely constrained by its lower theoretical capacity (175 mAh g^{-1}) as well as its low electronic conductivity and Li^+ diffusion coefficient [12]. Here, great efforts have been devoted to resolving these issues, including the development of novel nanostructures [36], carbon or oxide coatings [37] and composites [38]. For example, He et al. [39] prepared ultrathin LTO hierarchical microspheres composed of nanosheets through a simple hydrothermal procedure and reported that the resulting ultrathin nanosheets possessed larger reaction areas and enhanced Li^+ and electron transport. In another example, Shen et al. [40] synthesized mesoporous LTO/C nanocomposites using nanocasting technology with a porous carbon material (CMK-3) as a hard template and reported that the interpenetrating conductive carbon network of the CMK-3 can serve as a carrier to effectively promote electron transfer and improve the utilization of active materials. Furthermore, Wang et al. [41] synthesized a well-defined LTO nanosheet coating with a rutile-TiO_2 layer using a facile solution-based method and reported that as compared with a carbon layer, the resulting rutile-TiO_2 nanocoating layer can enhance the kinetic performance of LTO for rapid Li^+ de-intercalation. Similar to TiO_2 however, these methods can only alleviate and improve the properties of LTO electrode materials and cannot resolve the underlying issues of LTO (lower electron and ionic conductivity) (Fig. 1).

Based on the above discussions, the empty 3d orbital of Ti^{4+} in TiO_2 and LTO lattices appears to be the root cause of poor electron and ion conductivity, limiting application in energy storage devices. For example, Li^+ charge storage in Ti-based oxides involves charge-transfer reactions occurring at the interface and bulk accompanied by electron and ion diffusion kinetics. Here, numerous studies have suggested that the introduction of defects is the most effective method to enhance ionic diffusion and electronic conductivity in TiO_2 and LTO [42–45] in which the introduction of defects can narrow band gaps and provide additional energy levels (the intermediate band), thus expanding light absorption to longer wavelengths. In addition, defects can alter the electronic structure of TiO_2/LTO and optimize electron and ion transport kinetics. Moreover, the formation of disorder layers can modify the surface properties of Ti-based oxides (e.g., ion adsorption and surface activity) and enhance ion desolvation in electrolytes to improve kinetic performance in charge storage processes. Overall, the modified inherent properties of Ti-based oxides as induced by defects offer enormous potential for electrochemical energy storage applications. As a result, defect structures in Ti-based oxides have been widely investigated both experimentally and theoretically in which the defect type, concentration and distribution are important factors that determine the activity and selectivity of ion adsorption and storage, whereas the intrinsic properties of Ti-based oxides determine the formation condition, the location and property of defects.

In this review, recent advances in defective Ti-based oxides and their application in electrochemical energy storage devices will be summarized and discussed. In addition, the types of defects in Ti-based oxides including intrinsic defects [46–48], extrinsic defects [49–52] and

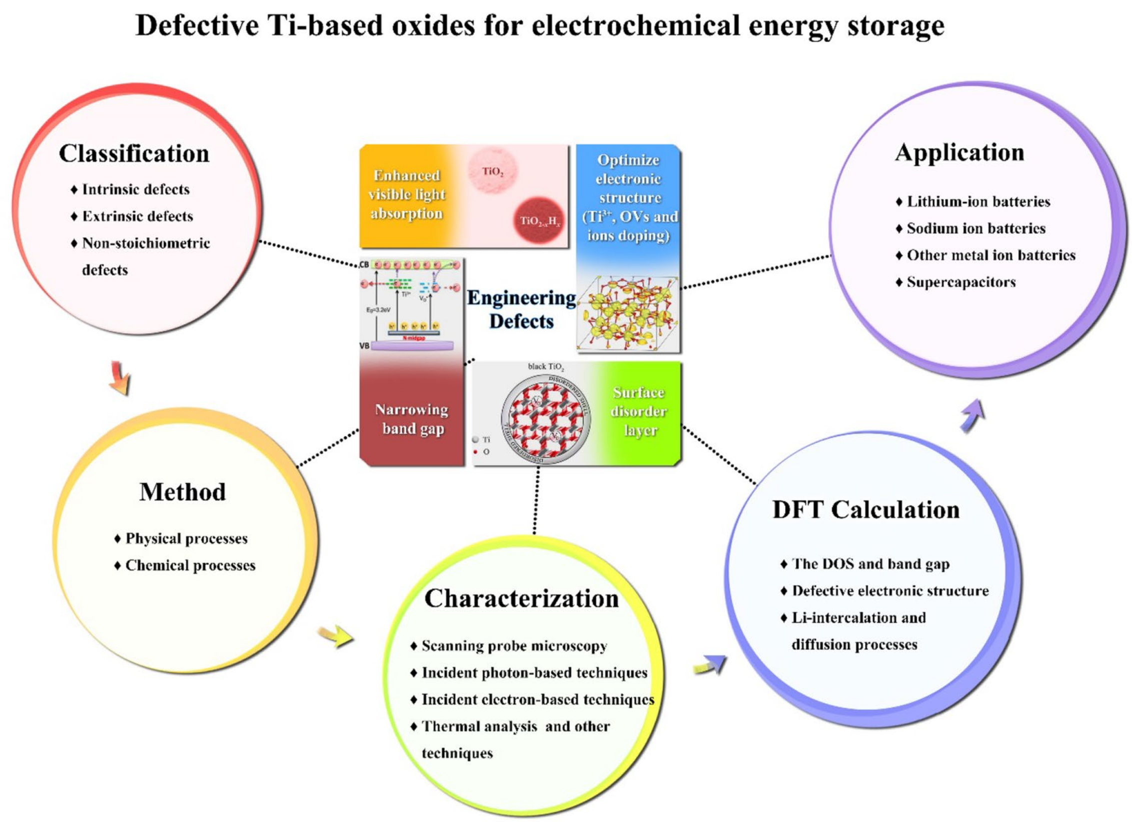

Fig. 1 Overview of key topics in Ti-based oxide defect chemistry for electrochemical energy storage

non-stoichiometric defects [53–56] will be introduced and their methods of preparation will be discussed. Furthermore, modified inherent properties such as optimized electronic structures, enhanced visible light absorptions, narrowed band gaps and surface disordered layers will also be discussed along with various techniques for characterization. Subsequently, density functional theory (DFT) calculations that provide theoretical explanations for these modified intrinsic properties and their effects on electrochemical energy storage will be outlined. Overall, this review will provide new insights into the role of defects in Ti-based oxides and facilitate their expansion into other fields.

2 Classification

Defect structures in metal oxides include intrinsic [46–48], extrinsic [49–52] and non-stoichiometric defects [53–56]. Of these defects, intrinsic defects (point defects) consist of lattice vacancies and do not alter the composition or stoichiometry of the overall crystal but affect the atoms around the vacancies and cause local lattice relaxation. Alternatively, extrinsic defects involve foreign atoms or ions being forced into crystal lattices to break the original atomic arrangement and induce partial lattice distortion, which can cause charge redistribution and the modification of electronic structures. Here, extrinsic defect concentrations can be controlled and material properties can be optimized by adjusting the number of doped heteroatoms. As for non-stoichiometric defects, these can alter both the composition and structure of crystals and exist mainly in compounds containing volatile elements such as oxides, sulfides and chlorides and are greatly affected by ambient atmosphere and temperature. In addition, non-stoichiometric defects tend to be found at the surface of lattices and can alter inherent properties such as electronic structure, optical absorption, ionic adsorption and surface activity.

2.1 Intrinsic Defects

Intrinsic defects (point defects) are the most frequently studied in Ti-based oxides and can serve as charge carrier traps, important adsorption and active sites and can affect the kinetics of electron and ion transport in electrochemical applications. And of the various point defects, Frenkel and Schottky defects (Fig. 2) are two main types that have been studied in detail.

Schottky defects normally occur if smaller size differences exist between cations and anions and involve cation and anion pairs being forced to leave original lattice

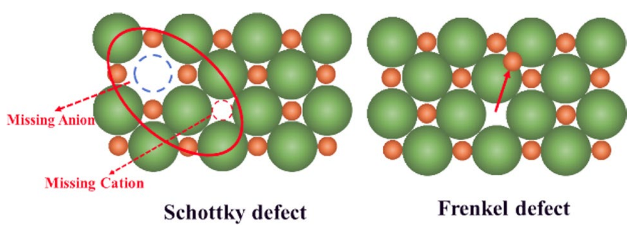

Fig. 2 Typical intrinsic defects: the Schottky defect and the Frenkel defect

Table 1 Defects in TiO_2 lattices and corresponding Kröger–Vink valence notation. Reprinted (adapted) with permission from Ref. [59], copyright (2011) American Chemical Society

Description	Kröger–Vink notation
Ti^{4+} ions in TiO_2 lattice sites	$Ti_{Ti}^{\times}$
Ti^{3+} ions in TiO_2 lattice sites (quasi-free electrons)	e'
Titanium vacancies	V_{Ti}''''
Ti^{3+} ions in TiO_2 lattice interstitial sites	$Ti_i^{\cdot\cdot\cdot}$
Ti^{4+} ions in TiO_2 lattice interstitial sites	$Ti_i^{\cdot\cdot\cdot\cdot}$
O^{2-} ions in oxygen lattice sites	$O_o^{\times}$
Oxygen vacancies	$V_o^{\cdot\cdot}$
O^- ions in oxygen lattice sites (quasi-free electrons)	$h^{\cdot}$

positions to create lattice vacancies (Fig. 2) [57]. In addition, Schottky defects do not affect the stoichiometry or overall neutral charge in corresponding crystal lattices. As for Frenkel defects, these usually occur if large size differences exist between cations and anions because smaller ions (usually cations) can easily migrate from original lattice sites to interstitial positions, leaving vacancies in original locations and forming interstitial defects in new positions [58]. And in terms of Ti-based oxides, Frenkel and Schottky defects do not alter crystal structures but will lead to electron redistribution. For example, defect equilibria can be used to describe the formation of defects in TiO_2 (Tables 1, 2) [59] in which oxygen vacancies (OVs), Ti^{3+} and Ti^{4+} ions in interstitial sites are prone to form in TiO_2 lattices (Eqs. 1–3, 5 in Table 2). Furthermore, the formation of Ti vacancies is a slow process (Eq. 4), illustrating that defect formation is a complex process usually accompanied by oxygen vacancies, interstitial defects and quasi-free electrons.

2.2 Extrinsic Defects

In contrast to intrinsic defects, extrinsic defects (doping defects) are caused by external atoms or ions entering the crystal lattice to replace original atoms or entering interstitial positions, resulting in local lattice distortion [48, 60–62]. Furthermore, corresponding charge compensation will occur in defective structures to maintain electrical neutrality if the valence state of impurity atoms is different from replaced atoms. Here, the concentration of extrinsic defects can be controlled by adjusting the number of heteroatoms to optimize material properties, and based on the properties of doped ions, extrinsic defects can be classified as either anion or cation doping defects. For example, metal cation doping defects in TiO_2 can introduce additional dopant-induced impurity energy levels within band gaps, which reduces the energy required for electronic excitation in which Carneiro et al. [63] studied Fe-doped TiO_2 and reported that two configuration energy levels were formed within the TiO_2 band gap by introducing Fe ions as a dopant. Here, these researchers suggested that because the oxidation level of Fe^{3+}/Fe^{4+} exceeded the valence band edge of TiO_2 and the reduction level of Fe^{3+}/Fe^{2+} was lower than the conduction energy level of TiO_2, the formation of electron–hole pairs can be facilitated through the capture and loss of electrons in the conduction band and valence band edge of TiO_2 (Fig. 3a). Researchers have also reported that other high-valence doping cations (V^{5+}, Sn^{4+} and Co^{3+}) can also adjust the band gap of TiO_2 and reduce the energy required for electronic excitation [56–58].

Compared with cation doping, the aim of anion doping is to overlap the S and P orbitals of anions with the intrinsic conduction and valence bands of TiO_2 to reduce band gaps and produce highly active electron–hole pairs on the surface [64–66]. For example, Czoska et al. [49] reported that in F-doped TiO_2, the exotic substitution of an O atom with a F atom can introduce an excess electron that reduces Ti^{4+} to Ti^{3+} and proposed two F-TiO_2 models in which one involves

Table 2 Basic defect reactions in TiO_2 (n and p denote the concentration of electrons and electron holes, respectively). Reprinted (adapted) with permission from Ref. [59], copyright (2011) American Chemical Society

	Defect reaction	Constant	$\Delta H°$ (kJ mol^{-1})	$\Delta S°$ [J (mol K)$^{-1}$]
1	$O_o^{\times} \leftrightarrow V_o^{\cdot\cdot} + 2e' + 1/2O_2$	$K_1 = [V_o^{\cdot\cdot}]n^2p(O_2)^{1/2}$	493.1	106.5
2	$Ti_{Ti}^{\times} + 2O_o^{\times} \leftrightarrow Ti_i^{\cdot\cdot\cdot} + 3e' + O_2$	$K_2 = [Ti_i^{\cdot\cdot\cdot}]n^3p(O_2)$	879.2	190.8
3	$Ti_{Ti}^{\times} + 2O_o^{\times} \leftrightarrow Ti_i^{\cdot\cdot\cdot\cdot} + 4e' + O_2$	$K_3 = [Ti_i^{\cdot\cdot\cdot\cdot}]n^4p(O_2)$	1025.8	238.3
4	$O_2 \leftrightarrow V_{Ti}'''' + 4h^{\cdot} + 2O_o^{\times}$	$K_4 = [V_{Ti}'''']p^4p(O_2)^{-1}$	354.5	–202.1
5	$nil \leftrightarrow e' + h^{\cdot}$	$K_i = np$	222.1	44.6
	$\ln K = [(\Delta S°)/R] - [(\Delta H°)/RT]$			

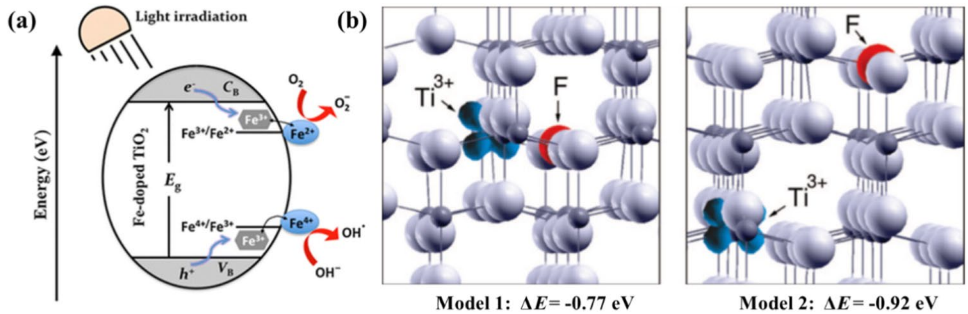

Fig. 3 **a** Diagram of the different energy levels for Fe–TiO_2. C_B and V_B correspond to the conduction and valence bands of the semiconductor. Reprinted with permission from Ref. [63], copyright (2014) Springer Nature. **b** Ball and stick models for F-doped anatase TiO_2. The left panel: a Ti^{3+} cation directly neighboring a F dopant. The right panel: a Ti^{3+} cation at ~7 Å distance from a F dopant. Reprinted with permission from Ref. [49], copyright (2008) American Chemical Society

a Ti^{3+} atom adjacent to a F atom (Model 1), whereas the other involves Ti^{3+} being separated from the F atom (Model 2) (Fig. 3b). Here, the relative position (ΔE) of the defect Ti 3d_{xz} state in Model 1 is much smaller than that in Model 2, indicating that excess electrons from F atoms can reduce neighboring Ti^{4+} to maintain a stable structure. Researchers have also introduced a series of nonmetallic elements such as B, C, N and S to replace O or to enter interstitial sites in TiO_2 lattices based on the valence and the radius of the doping atom [14, 67, 68] and have reported that multi-ion doping can generate additional synergistic effects to further optimize impurity energy levels and defect structures to improve performance in energy storage applications [69, 70].

Overall in TiO_2, metal cation doping can cause lattice distortion and reduce electron–hole pair formation to improve photon utilization, whereas nonmetallic anion doping can alter the response to visible light absorption and optimize quantum efficiency by reducing the band gap width and utilizing energy level staggered coupling.

2.3 Non-stoichiometric Defects

Different from intrinsic defects, non-stoichiometric defects can alter structural and stoichiometric compositions by creating sufficient vacancies and interstitial defects [53, 54]. Non-stoichiometric defects are also more prevalent in Ti-based oxides (e.g., LTO and TiO_2) because their oxygen atoms are more prone to be removed at low oxygen activities. In addition, non-stoichiometric defects are usually accompanied by the formation of intrinsic defects (Frenkel and Schottky defects). For example, Zhen et al. [71] compared stoichiometric and non-stoichiometric TiO_2 through calcination in air and Ar gas and reported that the ratio of O to Ti on the surface (1.98–1.78) calcined in air was near a perfect stoichiometric value of 2, whereas the ratio (1.70–1.67) prepared in Ar was below ideal stoichiometry, suggesting that lower oxygen pressures in Ar can result in the loss of lattice oxygen (Fig. 4). Researchers have also reported that non-stoichiometric TiO_{2-x} possesses a complex defect structure and can demonstrate excellent adsorption properties and electrochemical activities due to an amorphous surface layer with abundant defective sites such as reduced Ti^{3+}, Ti^{4+} interstitials and OVs. However, non-stoichiometric defects can also gradually be repaired in higher oxygen activity atmospheres at high temperatures, leading to the recovery of a stoichiometric structure.

3 Engineering of Defects

Methods to engineer defects in Ti-based oxides can be divided into physical and chemical processes (Fig. 5). In terms of physical processes, the creation of high activation energy and the doping of foreign atoms are important methods to achieve lattice distortion and deformation. Here, corresponding changes include the introduction of OVs, interstitial defects and the partial reduction of Ti^{4+} to Ti^{3+} [49, 72–74]. And although the lower defect concentrations associated with physical methods are undesirable

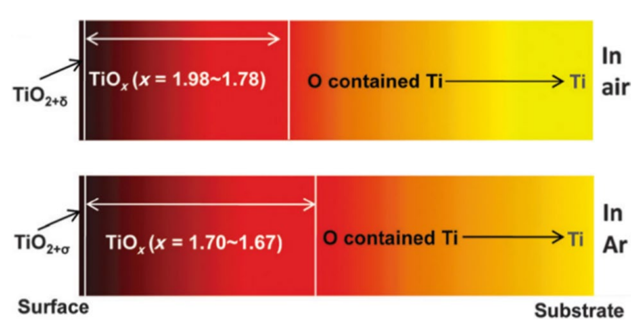

Fig. 4 Schematic showing compositional changes from the surface to the substrate in TiO_2 during calcination in air or Ar. Reprinted with permission from Ref. [71], copyright (2013) Royal Society of Chemistry

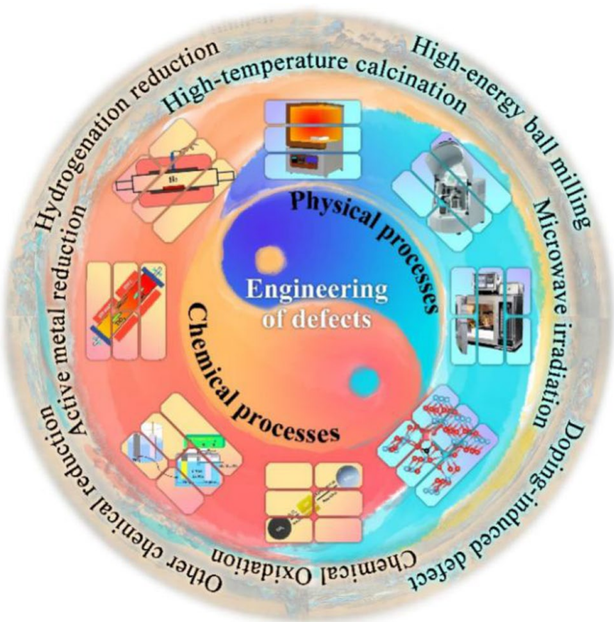

Fig. 5 Methods for engineering defects

in terms of improving the intrinsic properties of Ti-based oxides, the reduction of high-valence state Ti from Ti^{4+} to Ti^{3+} or Ti^{2+} and the oxidization of low-valence state Ti from Ti^{2+} or Ti^{3+} to Ti^{4+} are reported to be effective chemical methods to induce high defect concentrations in Ti-based oxides [44, 75–77]. Despite this, specific conditions in terms of temperature, pressure and atmosphere are required for these redox reactions to occur. Therefore, the formation of defects is a complex physicochemical process and detailed understandings of these methods can elucidate defect formation mechanisms and allow for the optimization of intrinsic properties associated with various applications.

3.1 Physical Processes

3.1.1 High-Temperature Calcination

Although intrinsic defects (Frenkel and Schottky defects) are found in low concentrations, defect density can usually be controlled by adjusting temperature [72, 78]. Equation (1) summarizes the relationship between structural defect concentration and temperature:

$$\frac{N_{\mathrm{v}}}{N} = \exp\left(-\frac{Q_{\mathrm{v}}}{k_{\mathrm{B}}T}\right) \tag{1}$$

In which N_v is the number of defects in the lattice, N is the number of potential defect sites, Q_v is the activation energy for vacancy formation, k_B is the Boltzmann's constant, and T is the temperature. And because defect concentrations increase exponentially with temperature, calcination is considered to be an effective method to create structural defects in Ti-based oxides in which oxygen atoms in Ti-based oxides tend to diffuse to the surface or the subsurface layer and thereby form OVs [79]. However, these OVs are unstable and can easily be refilled by oxygen in air or H_2O [80]. For example, Ghosh et al. [81] analyzed the evolution of OVs in TiO_2 calcined in air and Ar atmospheres (Fig. 6) and reported obvious structural defects or lattice imperfections in TiO_2 samples calcined at 300 °C in air, whereas samples gradually evolved into single crystalline phases as

Fig. 6 TEM micrographs of TiO_2 nanoparticles annealed at different temperatures in **a**, **b** air or **c**, **d** Ar gas. Inset (i) HRTEM images (white circles indicate lattice defects) and (ii) corresponding selected area electron diffraction (SAED) patterns. Reprinted with permission from Ref. [81], copyright (2013) American Chemical Society

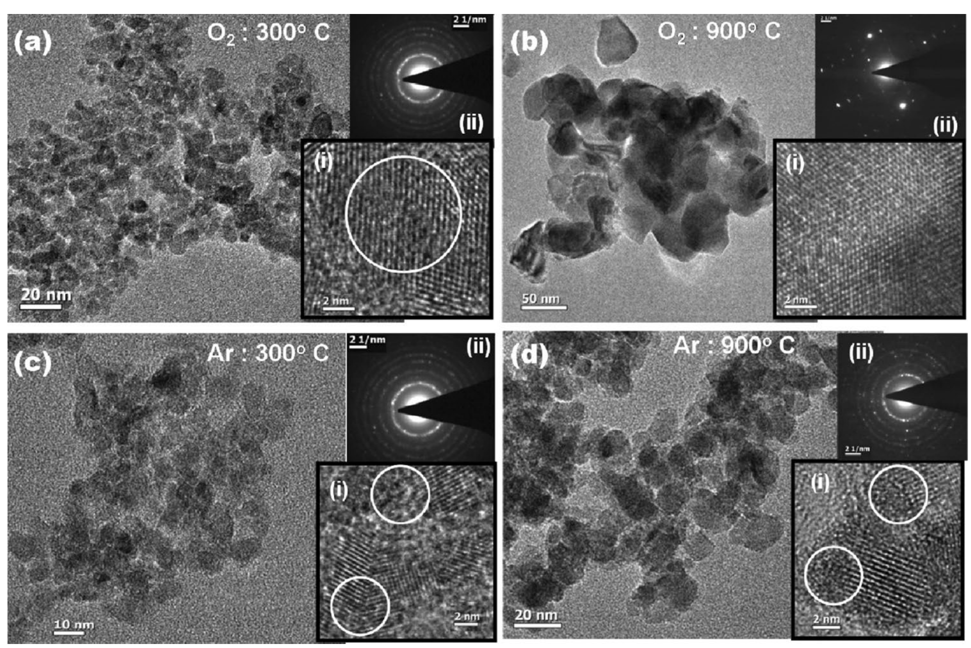

annealing temperatures reached 900 °C (Fig. 6a, b), demonstrating that high temperature calcinations in the presence of sufficient oxygen can repair partial OVs and increase crystallinity. Alternatively, these researchers reported different results in Ar-annealed samples in which defects or imperfections were still present after annealing at 300 and 900 °C (Fig. 6c, d), which may be explained with reference to the balance between surface oxygen in TiO_2 and oxygen in the atmosphere (Eq. 2) in which not only are OVs in TiO_2 unable to receive enough replenishing oxygen in a severely oxygen-deficient atmosphere, but high temperatures can also tilt the balance toward producing more OVs.

$$O_O\,(\text{surface}) \xrightarrow{\Delta} V_O^{\cdot\cdot}\,(\text{surface}) + 2e' + \frac{1}{2}O_2\,(\text{surface}) \qquad (2)$$

Researchers have also studied oxygen-deficient atmospheres including Ar, N_2, He or vacuum to create OVs in Ti-based oxides during calcination at high temperatures [81–84]. For example, Xia et al. [82, 83] prepared vacuum-treated TiO_2 to analyze the effects of vacuum heating and reported that the vacuum-treated TiO_2 was yellow in color (Fig. 7a) and that its absorption range for visible light was extended from the original 400–1100 nm (Fig. 7b) in which a disordered amorphous shell formed at the edge of the crystalline region after vacuum treatment (Fig. 7c, d). Guillemot et al. [84] also reported that TiO_2 exhibited a typical n-type defective structure (TiO_{2-x}) if calcined in vacuum and similarly; Chen et al. [85] reported that $Li_4Ti_5O_{12-y}$ can be synthesized through calcination in N_2 atmosphere at 500 °C for 2 h. Overall, defect concentrations increase with calcination temperature in vacuum.

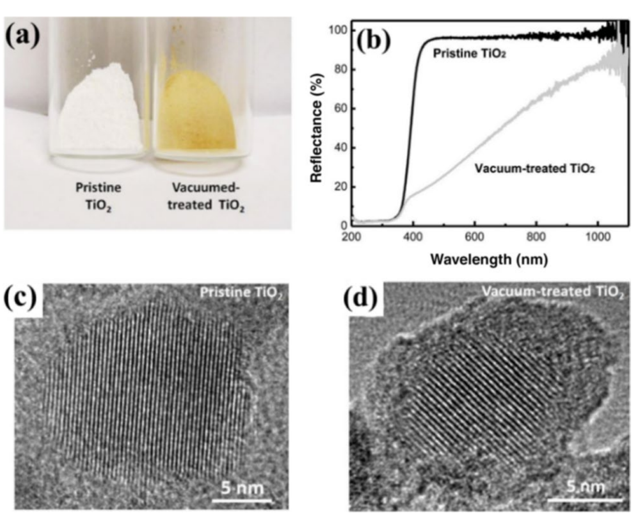

Fig. 7 **a** Digital image, **b** UV–Vis reflectance spectra, **c**, **d** HRTEM images of pristine and vacuum-treated TiO_2. Reprinted with permission from Ref. [83], copyright (2013) John Wiley and Sons

3.1.2 High-Energy Ball Milling

In addition to providing activation energy for the formation of defects through high temperatures, high-energy ball milling is another efficient method to gain grain refinement, defects and lattice distortions through repetitive deformation, fragmentation and cold welding under mechanical activation [73, 86–90]. Here, high-energy ball milling is an extensively investigated mechanochemical reaction technique in which a ball and powder are confined in a closed container and subjected to mechanical revolution and rotation, resulting in kinetic energy and mechanical stress, which leads to particle pulverization, lattice distortion and structural defects. For example, Indris et al. [89] dry-milled TiO_2 using a SPEX8000 ball mill in air for up to 4 h and reported that the partial Ti–O bonds at the surface of TiO_2 can be broken through mechanical activation to release oxygen atoms as O_2, thus forming OVs and allowing for a transition from Ti^{4+} to Ti^{3+} in the TiO_2 lattice (Eq. 3 and 4):

$$TiO_2 \rightleftharpoons TiO_{2-x} + xO\,(\text{break Ti–O bonds}) \qquad (3)$$

$$TiO_{2-x} + xO \rightleftharpoons TiO_{2-x} + V_o + x/2O_2 \qquad (4)$$

These researchers also studied the influence of high-energy ball milling on TiO_2 by examining XPS Ti 2p spectra (Fig. 8a) and reported that milled TiO_2 presented an additional peak at 456.9 eV that can be attributed to Ti^{3+}. In addition, EPR measurements were taken in this study to confirm the formation of Ti^{3+} after milling (Fig. 8b) in which a narrow signal at $g=1.96$ was observed in the un-milled TiO_2 that gradually increases in intensity with increasing milling times. More importantly, the results showed that a broad peak related to Ti^{3+} at $g=2.42$ started to appear after milling for 2 h. Overall, both the XPS and EPR results in this study demonstrated that high-energy ball milling can create lattice distortions and generate OVs and Ti^{3+} in TiO_2 lattices.

Milling atmosphere also has important effects on high-energy ball milling induced defects. For example, Pan et al. [87] prepared milled TiO_2 at 220 rpm for 40 h in air and nitrogen atmospheres and found that the low oxygen pressure in the nitrogen atmosphere can affect the balance of defect reactions in Eqs. 3 and 4 and was more conducive to the formation of oxygen defects during high-energy ball milling.

3.1.3 Microwave Irradiation

Compared with conventional heating, microwave irradiation is a more rapid heating method that can generate spin among polar molecules through an electromagnetic field and convert electromagnetic energy into thermal

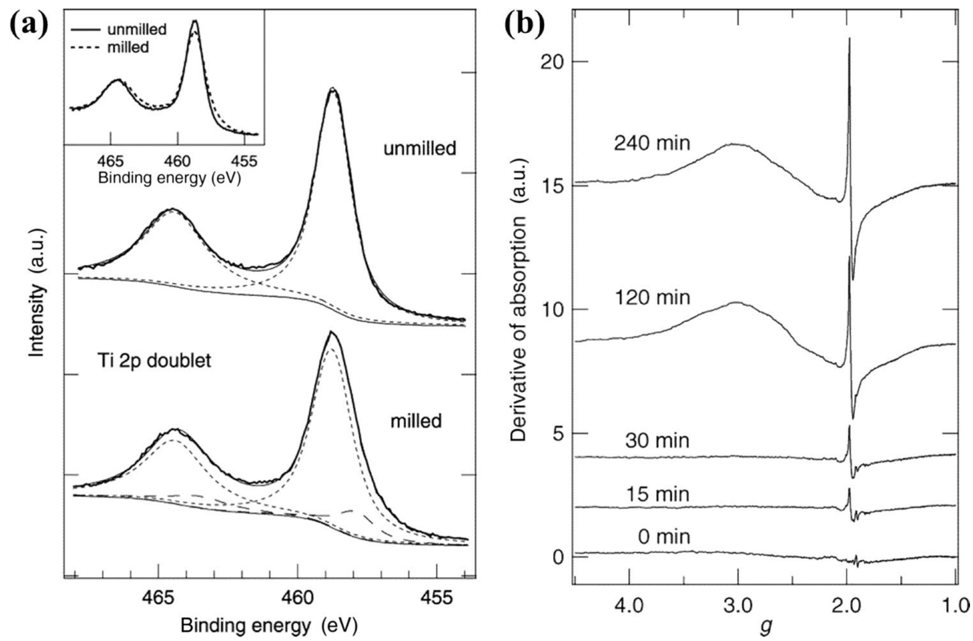

Fig. 8 **a** XPS spectra of unmilled anatase and anatase milled for 4 h at 100 K. **b** EPR spectra of ball-milled TiO_2 (rutile). Reprinted with permission from Ref. [89], copyright (2005) American Chemical Society

energy. In addition, the molecular vibration caused by microwave radiation can break the ionic bonds in TiO_2 and help to form defect structures [91–93]. For example, Ishida et al. [93] synthesized black TiO_2 powder by subjecting a water-soluble Ti complex to microwave-induced plasma at 100 W for 60 min and reported strong absorption in all visible light regions (Fig. 9a). Marinel et al. [91] also reported the dielectric properties of microwave-treated TiO_2 in which their microwave-treated TiO_2 was synthesized through the manual grinding of TiO_2 powder in an agate mortar and pressed into a disk through uniaxial pressing (90 MPa) followed by microwave treatment (200 W), resulting in the color of the TiO_2 disk to change from white to yellowish brown (Fig. 9b).

3.1.4 Doping-Induced Defect Processes

Ion doping in Ti-based oxide lattices is an effective method to achieve lattice distortion and introduce impurity states in band gaps, thereby extending absorption into the visible light region [49, 74, 94–97]. Overall, interstitial and substitutional dopings in TiO_2 lattices are complex processes and metal and nonmetal doping processes are discussed in this section to illustrate the formation of doping-induced defect structures. In general, nonmetal atoms (B, N, S, F, etc.) can replace O atoms and metal atoms can displace Ti ions in doping processes. This is generally accompanied by large amounts of ions entering interstitial positions, resulting in corresponding charge compensation in doping areas and the reorganization of electronic structures.

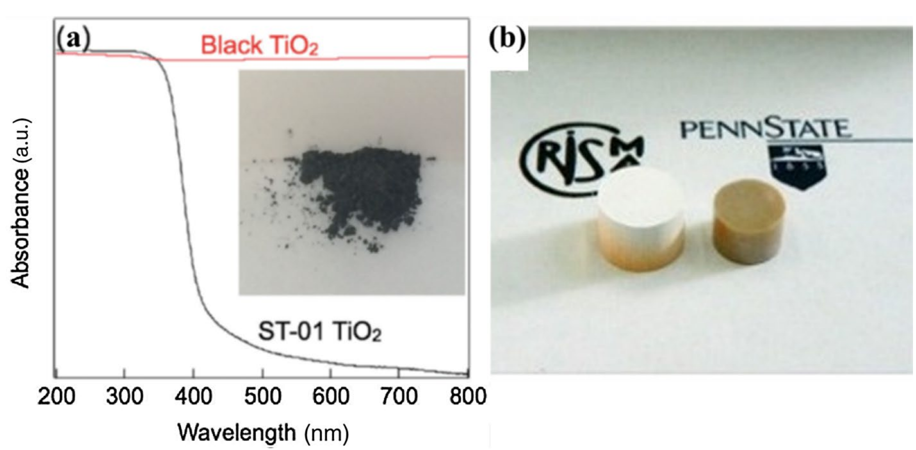

Fig. 9 **a** UV–Vis spectra of black and white TiO_2 nanoparticles (the inset: a photo of black TiO_2 powder). Reprinted with permission from Ref. [93], copyright 2015, Chemical Society of Japan(CSJ). **b** Picture of white TiO_2 turning to yellowish brown after microwave treatment. Reprinted with permission from Ref. [91], copyright 2013, Elsevier

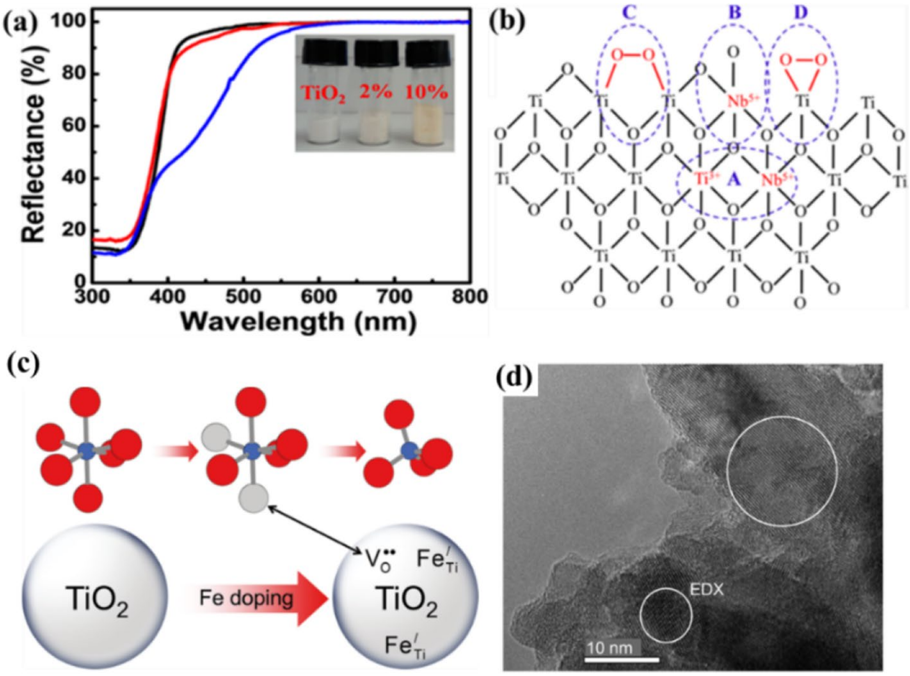

Fig. 10 **a** UV–Vis diffuse reflectance spectra of undoped and Nb-doped TiO_2 samples and **b** the defect structure of Nb-doped TiO_2: A = the Ti^{3+} and Nb^{5+} defect couple, B = surface Nb^{5+} defects, C and D = surface peroxide defects. Reprinted with permission from Ref. [52], copyright (2015) American Chemical Society. **c** Transformation from octahedral to tetrahedral-coordinated Ti^{4+} in Fe–TiO_2 and **d** high-resolution TEM image of 10% Fe/TiO_2 after annealing in air. Reprinted with permission from Ref. [74], copyright (2012) American Chemical Society

3.1.4.1 Metal Ion Doping In one study, Kong et al. [52] obtained defect-induced yellow TiO_2 by introducing Nb to partially replace Ti and reported that the color of the solution gradually deepened to yellow with increasing Nb concentrations (Fig. 10a), which these researchers attributed to the fact that the introduced Nb^{5+} can not only replace Ti^{4+} but also lead to neighboring Ti^{4+} transitioning to Ti^{3+} in the TiO_2 lattice (Fig. 10b). In another study, Wu et al. [74] obtained defective TiO_{2-x} by introducing Fe^{3+} to replace Ti^{4+} in TiO_2 lattices corresponding to the formation of OVs. Here, these researchers suggested that Fe^{3+} can serve as an acceptor-type dopant to partially remove and rearrange oxygen ions in TiO_6 octahedra and form OVs and TiO_4 tetrahedra (Fig. 10c). These researchers also observed an obvious amorphous region in the high-resolution TEM image of Fe-doped TiO_2 nanoparticles (Fig. 10d), which clearly revealed the formation of large numbers of OVs after the introduction of Fe^{3+} into TiO_2. In a further study, Pathak et al. [98] prepared Al-doped TiO_2 by replacing Ti^{3+} with Al^{3+} due to similar atomic radii as well as the instability of Ti^{3+}. And in addition to these mentioned cations, researchers have also reported that other cations such as Cu^{2+} [99], Zn^{2+} [100], Co^{2+} [101, 102], Cr^{3+} [94], Mn^{5+} [103, 104] and V^{5+} [105] can also be used as effective doping ions to create defective TiO_2 structures. Here, researchers suggested that high-valence ions (M^{4+} or M^{5+}) can lead to the transition of neighboring Ti^{4+} to Ti^{3+} and contribute to the stabilization of Ti^{3+} but do not produce OVs, whereas low-valence ions (M^{1+}, M^{2+} or M^{3+}) can form OVs but are not conducive to the formation of Ti^{3+}.

3.1.4.2 Nonmetal Ion Doping Similar to metal-doping ions, nonmetal ions (B, C, N, S, etc.) have also been introduced to replace O atoms or into interstitial positions in TiO_2 lattices [49, 95, 106], resulting in the extension of the visible light absorption region of materials by narrowing band gaps, forming impurity energy levels and creating OVs. For example, Feng et al. [107] prepared B-TiO_{2-x} through a simple hydrolysis reaction and reported that the color of the TiO_2 changed from white to gray and subsequently to blue with the increasing B content (Fig. 11). In another example, Irie et al. [108] synthesized $TiO_{2-x}N_x$ nanoparticles through annealing at 550, 575 and 600 °C for 3 h under NH_3 atmos-

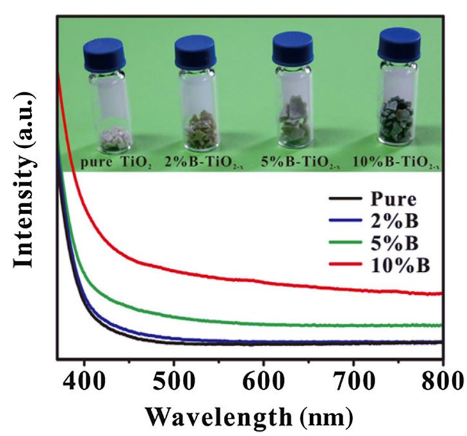

Fig. 11 UV–Vis absorption spectra of pure TiO_2 and B-TiO_{2-x} samples with various B-doping contents along with corresponding photographs. Reprinted with permissions from Ref. [107] under Creative Commons

phere and reported that the N concentration in TiO_{2-x} gradually increased with calcination temperatures. Moreover, Czoska et al. [49] prepared F-doped TiO_2 through a typical impregnation technique in which TiO_2 powder was placed in aqueous HF (1 L) with continuous stirring for 1 h followed by repeated washing with water and drying at 40 °C for 4 h and similarly, Qi et al. [109] prepared $Li_4Ti_5O_{12-x}Br_x$ samples through a conventional high-temperature solid-state reaction in which $LiOH·H_2O$, $LiBr·H_2O$ and TiO_2 were ground together for 1 h and heated at 900 °C for 12 h in air.

3.2 Chemical Processes

3.2.1 Hydrogenation Reduction

Because high-valence oxidation state Ti species are the main forms of Ti-based oxides, the partial reduction of Ti^{4+} to Ti^{3+} through chemical methods is an effective strategy to create defect structures. Here, hydrogenation is able to capture oxygen and maintain OVs in Ti-based oxides, corresponding to the incomplete reduction process from high-valence-state Ti species [44, 75]. Using the hydrogenation process of TiO_2 as an example, TiO_2 can exhibit different colors from white to blue to black with increasing defect concentrations and the hydrogenation process can be summarized as:

$$TiO_2 + H_2 \rightleftharpoons TiO_{2x} + TiO_{2-x}H_{2x} + V_o + H_2O \quad (5)$$

And although according to Eq. 5, hydrogenation should be simple, the full hydrogenation mechanism is actually complex and is affected by temperature, reaction time, pressure, H_2 partial pressure, hydrogen plasma and ion doping, all of which play a vital role in inducing TiO_2/LTO defect structures during hydrogenation. In addition, the defect concentrations and related physiochemical properties of TiO_2/LTO can exhibit different characteristics due to these conditions [110].

3.2.1.1 High-Temperature Hydrogenation As an example of high-temperature hydrogenation, Naldoni et al. [42] obtained black TiO_2 through hydrogen reduction at 500 °C for 1 h (Fig. 12a) and reported that although the Raman results of white and black TiO_2 both presented similar phase compositions, a smaller peak shift appeared in the black TiO_2 that can be attributed to the defect structure after hydrogenation (Fig. 12b). Jiang et al. [111] also reduced white P25 TiO_2 nanoparticles through annealing at 400 °C for 10 h under a pure hydrogen gas (99.99%) atmosphere to obtain a gray-colored H-P25 and attributed the different coloration to the cooling rate after hydrogenation.

Reaction times and calcination temperatures are also important factors affecting the hydrogenation effect. For example, Wang et al. [112] studied hydrogenated TiO_2 nanowire films synthesized at various temperatures from 300 to 550 °C for 0.5 h and found that white untreated TiO_2 turned yellowish green at 300 to 350 °C and finally black at 450 °C and up (Fig. 12c), suggesting that the increased visible light absorption is a result of high-temperature activation and hydrogenation. In another study, Yu et al. [44] also observed the gradual color change of TiO_2 from white to blue to gray by controlling annealing temperatures

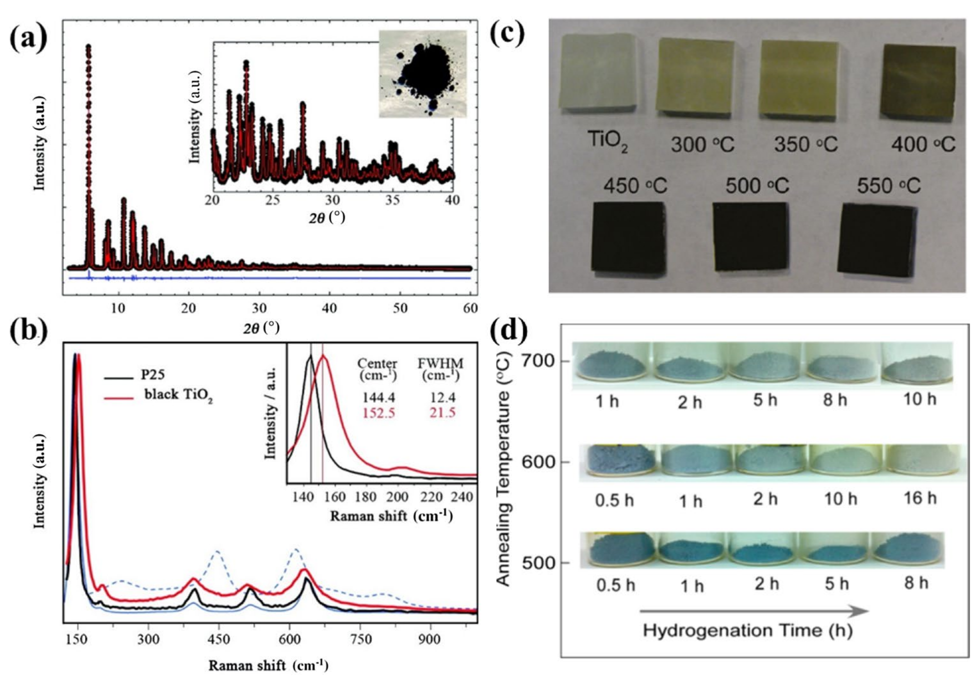

Fig. 12 **a** SXRPD pattern and photo of black TiO_2 and **b** micro-Raman spectra of P25 and black TiO_2. Reprinted with permission from Ref. [42], copyright (2012) American Chemical Society. **c** Photographs of pristine TiO_2 and H-TiO_2 nanowires annealed in hydrogen at various temperatures from 300 to 550 °C. **d** Gradual changes in the color of TiO_2 from blue to gray at different annealing temperatures and annealing times in a hydrogen atmosphere. Reprinted with permission from Ref. [44], copyright (2013) American Chemical Society

(500–700 °C) and hydrogenation times (0.5–16 h) in which white untreated TiO_2 turned blue at the starting stages (0.5–1 h) of hydrogenation and gradually turned gray with increasing hydrogenation times (8–16 h) (Fig. 12d). Here, these researchers reported that temperature can also determine color change to some extent in which blue TiO_2 can be retained longer (over 8 h) at 500 °C but turns to pale gray at 600 and 700 °C.

3.2.1.2 High-Pressure Hydrogenation As an example of high-pressure hydrogenation, Chen et al. [75] obtained black TiO_2 nanocrystals through calcination at 200 °C for 5 days under high pressure hydrogen (20.0 bar H_2) and reported that a thin amorphous layer formed on the crystalline TiO_2 after hydrogenation, resulting in an obvious color change from white to black (Fig. 13a–d). In addition, Qiu et al. [113] obtained blue rutile TiO_2 through typical hydrogenation at 450 °C for 1 h with 40 bar hydrogen pressure (Fig. 13e) and reported that their white and blue TiO_2 showed similar diffraction peaks, indicating that hydrogenation does not change the rutile framework and that color changes can be attributed to OVs. Qiu et al. [110] in another study also prepared hydrogenated LTO through calcination at 500 °C (50 °C min^{-1}) under 40 bar H_2 atmosphere for 1 h and reported that the color of the sample changed from white to blue as a result of OVs (Fig. 13f, g). Furthermore, Lu et al. [114] prepared multiple colors of TiO_2 based on different hydrogenation times at room temperature (35 bar H_2, 3–17 days) in which white TiO_2 shifted to pale yellow after 3 days and gradually changed into much deeper colors with increasing hydrogenated times (Fig. 13h). The resulting enhanced visible light absorption in this study was also confirmed by UV–Vis spectra (Fig. 13i).

3.2.1.3 Mixed Atmosphere Hydrogenation As for mixed atmosphere hydrogenation, Cai et al. [115] obtained hydrogenated TiO_2 through calcination in a mixed atmosphere (10 vol% H_2/N_2) at 650 °C for 5 h in which a disordered shell formed on the surface of TiO_2 during high-temperature hydrogenation accompanied by the transition of TiO_2(B)-anatase heterophase junctions (Fig. 14a). Su et al. [116] also prepared colored TiO_2 nanocrystals through hydrogen thermal treatments (1 °C min^{-1}) at 300, 400, 500 and 600 °C for 5 h under a mixed atmosphere (10% H_2 and 90% N_2) and suggested that the enhanced visible region absorbance associated with temperature was caused by OVs (Fig. 14b). These researchers also reported that band gap values decreased with increasing calcination temperatures and that the color of the sample gradually transformed from white to light yellow and subsequently to darker gray (Fig. 14c). In a further study, Wu et al. [117] compared the effects of different calcination atmospheres on TiO_2 including air, nitrogen (99.999%) and a hydrogen/nitrogen mixture (15% H_2–85% N_2) under various temperatures from 400 to 600 °C for 2 h and reported that white TiO_2 turned black in N_2 and H_2/N_2 mixed atmospheres at high temperatures (400 °C and above) (Fig. 14d). Liu et al. [118] also studied the effects of pressure and atmosphere on TiO_2 color under

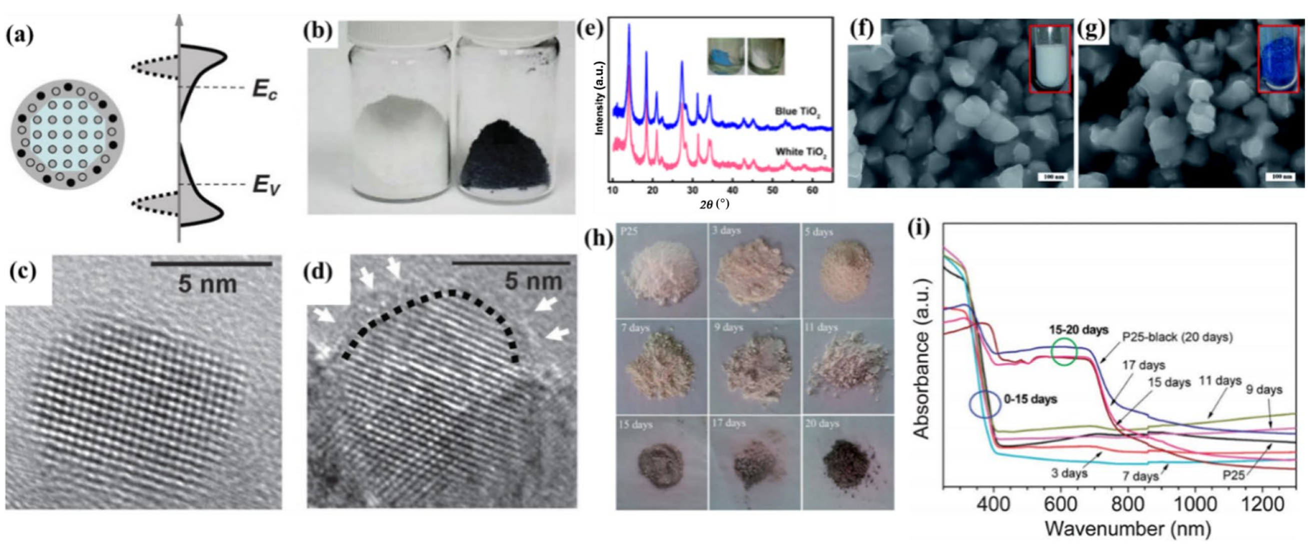

Fig. 13 **a** Schematic of the formation of black TiO_2. **b** Photographs of white and black TiO_2. **c**, **d** HRTEM images of white and black TiO_2 nanocrystals. Reprinted with permission from Ref. [75], copyright (2011) American Association for the Advancement of Science. **e** XRD spectra of blue and white TiO_2 along with corresponding photographs. Reprinted with permission from Ref. [113], copyright (2014) American Chemical Society. **f, g** SEM images of pristine and blue H-LTO. Reprinted with permission from Ref. [110], copyright (2014) Royal Society of Chemistry. **h** Photographs and **i** UV–Vis spectra of P25 treated at different hydrogenation times (35 bar, H_2) at room temperature. Reprinted with permission from Ref. [114], copyright (2014) Royal Society of Chemistry

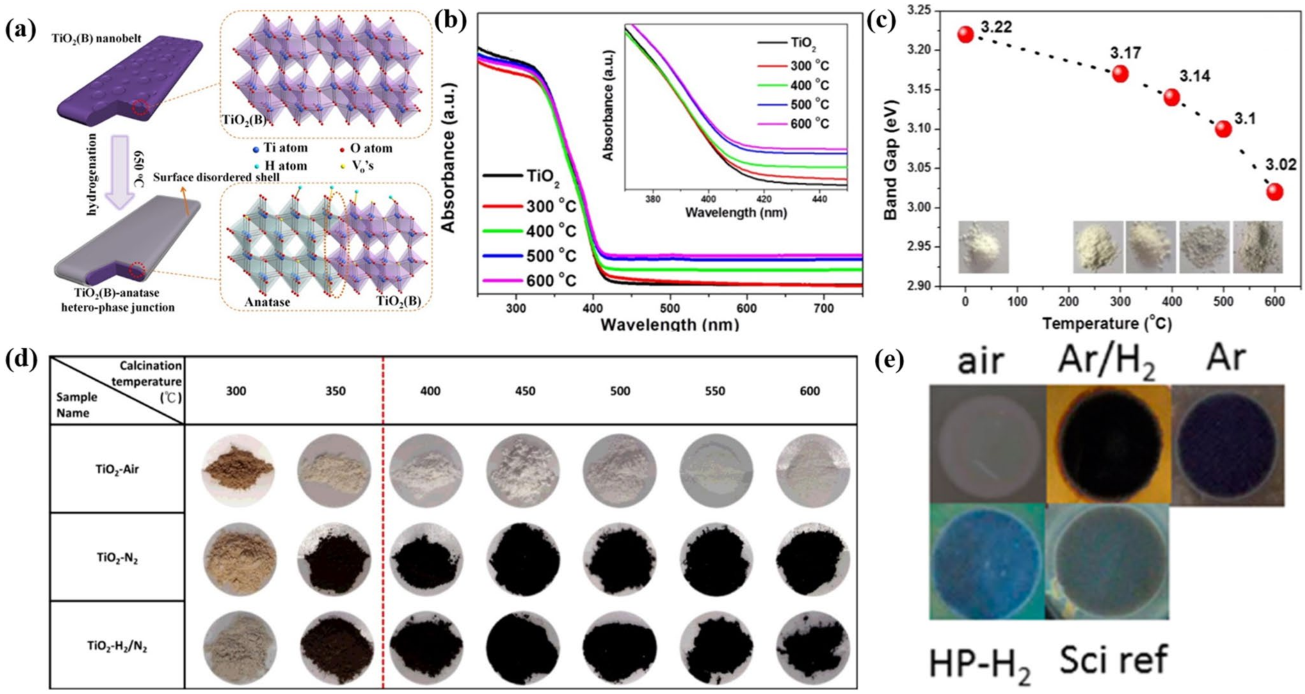

Fig. 14 **a** Simplified schematic showing defects and the TiO_2(B)-anatase heterophase junction. Reprinted with permission from Ref. [115], copyright (2015) American Chemical Society. **b** UV–Vis spectra of obtained samples and **c** band gap energy at different temperatures. Reprinted with permission from Ref. [116], copyright (2015) American Chemical Society. **d** Color change of TiO_2 nanocrystals calcined at various temperatures for 2 h under different atmospheres of air, nitrogen and a hydrogen/nitrogen mixture. Reprinted with permission from Ref. [117], copyright (2016) Elsevier. **e** TiO_2 nanotubes annealed in air, Ar/H_2 or high pressure H_2. Reprinted with permission from Ref. [118], copyright (2014) American Chemical Society

different hydrogenation conditions including calcination at 450 °C for 1 h in air, calcination in Ar(Ar) or H_2/Ar at atmospheric pressure, high-pressure H_2 treatment (20 bar, 500 °C for 1 h) and high pressure but low-temperature treatment (H_2, 20 bar, 200 °C for 5 d) and reported that white TiO_2 gradually turned black under Ar(Ar) or H_2/Ar atmospheres but was light blue in the high pressure H_2 treatment (20 bar, 500 °C for 1 h) and gray in the high pressure but low temperature atmosphere treatment (H_2, 20 bar, 200 °C for 5 d) (Fig. 14e).

3.2.1.4 Ion Doping Hydrogenation Ion doping has been reported to be able to modify band structures by producing additional dopant-induced impurity energy levels. And by combining hydrogenation with ion doping, band gap structures can be further optimized and visible light adsorption can be further enhanced. For example, Wang et al. [119] prepared a series of F-, NF-, HF- and NHF-doped TiO_2 through various processes, including the hydrothermal reaction of tetrabutyl titanate at 180 °C for 24 h with HF as an additive to produce TiO_2-F, the mixing of TiO_2-F with urea followed by calcination at 400 °C for 2 h in air to produce TiO_2-NF and the hydrogenation of TiO_2-F and TiO_2-NF at 400 °C for 2 h to produce TiO_2-HF and TiO_2-NHF and reported

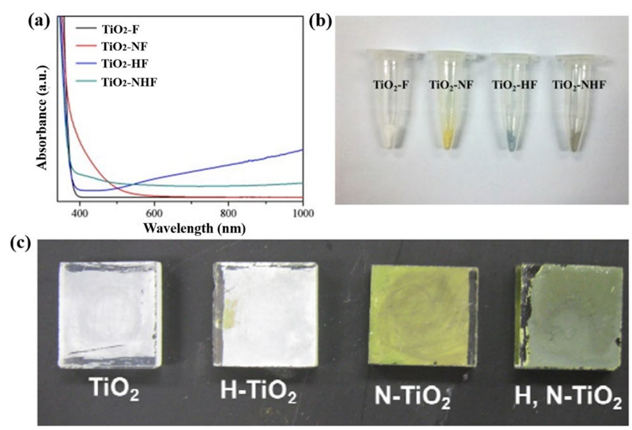

Fig. 15 **a** UV–Visible absorption spectra of TiO_2-N, TiO_2-NF, TiO_2-HF and TiO_2-NHF and **b** corresponding colors. Reprinted with permission from Ref. [119], copyright (2012) Elsevier. **c** TiO_2, H-TiO_2, N-TiO_2 and H, N-TiO_2 nanowire arrays. Reprinted with permission from Ref. [120], copyright (2012) American Chemical Society

that completely different visible light absorption spectra can be observed for each sample (Fig. 15a, b) in which TiO_2-F possessed a white color but changed to bright yellow and dark blue after N-doping and H-doping, respectively, before finally taking on a brown color as TiO_2-NHF. Here, these obvious color changes can be attributed to the modified band structures as induced by ion doping in which only a few F ions can enter the TiO_2-F lattice, resulting in a mild defect band state, whereas if N atoms were doped into the lattice, relatively serious structural distortions will occur, and Ti^{3+} and two independent N 2p defect states will form between the conduction band and the valence band. As for TiO_2-HF, H_2 can capture O and F atoms to generate large amounts of vacancies and corresponding Ti^{3+} in the TiO_2 lattice. Similarly, H_2 can react with N, F and O atoms in TiO_2-NF lattices and maintain the amount of OVs (N), OVs (F) and OVs (H) as well as different Ti^{3+}(N), Ti^{3+}(F), Ti^{3+}(H) and Ti^{3+}(H'), leading to a dark brown color. In another example, Hoang et al. [120] obtained TiO_2 nanowire arrays through calcination in various atmospheres including H-TiO_2 (500 °C in H_2/Ar for 1 h), N-TiO_2 (500 °C in NH_3 for 2 h) and H, N-TiO_2 (500 °C in H_2/Ar for 1 h followed by NH_3 at 500 °C for 2 h) and reported no obvious color change after hydrogenation as compared with pristine TiO_2 but that the color changed to green after nitridation and dark green after both nitridation and hydrogenation (Fig. 15c).

3.2.1.5 Plasma-Enhanced Hydrogenation For plasma-enhanced hydrogenation, Yan et al. [121] obtained various colored TiO_2 after treatment with hydrogen plasma in which white TiO_2 was treated by using an inductively coupled plasma instrument at 150 °C for 30 s, 1 min, 3 min, 5 min and 20 min and reported that the color of TiO_2 gradually deepened from white to blue (3 min) to dark blue (5 min) and finally to black (20 min) (Fig. 16) as confirmed by the increasing visible light absorbance in the UV–Vis spectra. Wu et al. [122] also prepared blue TiO_2 through hydrogen plasma treatment in which white TiO_2 was preheated in a vacuum at 320 °C for 0.5 h and subsequently treated with hydrogen plasma for 1.5 h under 50 Pa H_2 gas, and they observed a similar color evolution from white to blue.

3.2.2 Active Metal Reduction

Compared with hydrogen, metal elements such as Li, Al, Mg and Zn possess relatively high reducing activities and can partially capture oxygen atoms to leave OVs and Ti^{3+} centers in lattices [79, 123–126]. In addition, significant advantages such as low costs and simple and safe preparation methods have attracted widespread attention for metal reduced TiO_2.

3.2.2.1 Li-Based Reduction As an example of Li-based reduction, Ou et al. [79] obtained black TiO_2 through a simple grinding process in which the initial white TiO_2 turned blue with the addition of 1 wt% Li powder and subsequently changed to black as the amount of Li powder increased (Fig. 17a). Here, these researchers reported that this obvious color change did not affect the crystal structure of TiO_2

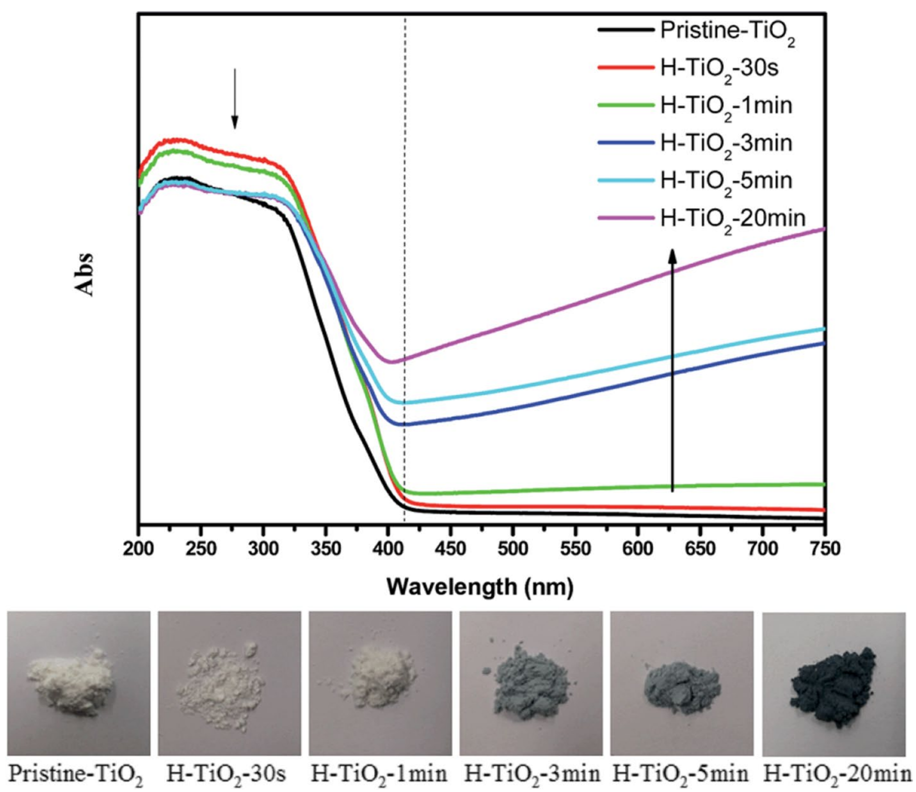

Fig. 16 UV–Vis absorption spectra and related photographs of obtained TiO_2 with H_2 plasma treatment for 30 s, 1 min, 3 min, 5 min and 20 min, respectively. Reprinted with permission from Ref. [121], copyright (2014) Royal Society of Chemistry

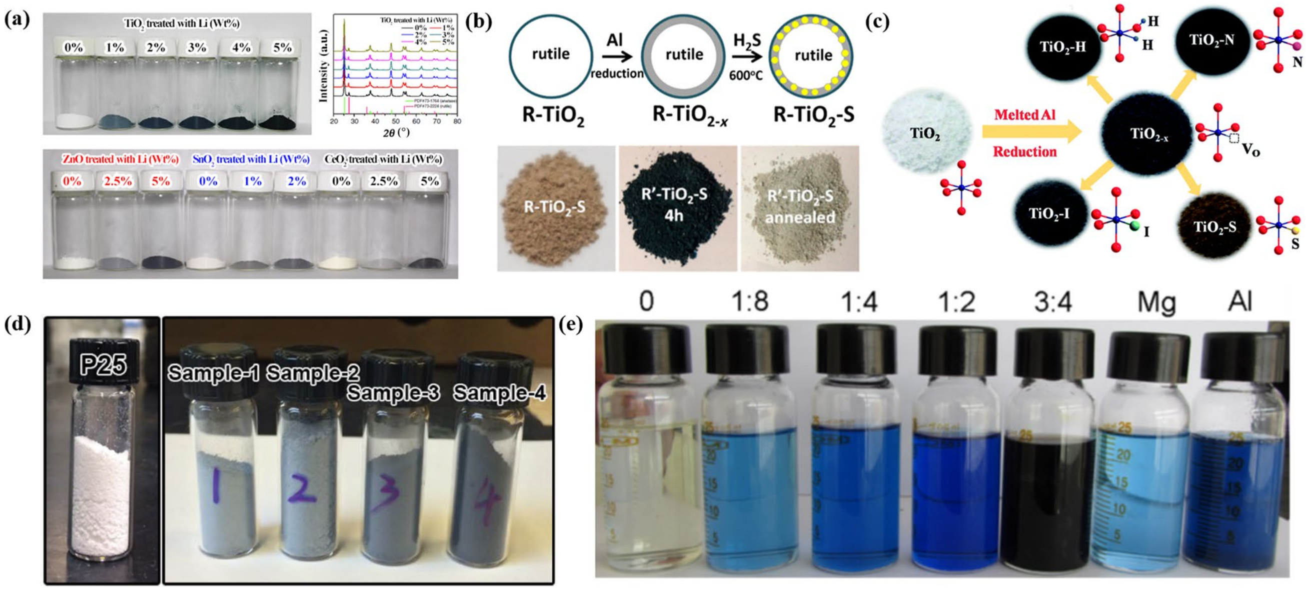

Fig. 17 **a** Photographs of pristine and Li-reduced oxide nanoparticles: TiO_2, ZnO, SnO_2 and CeO_2. Reprinted with permission from Ref. [79], copyright (2018) Springer Nature. **b** Schematic of the synthesis of rutile TiO_2 (R-TiO_2) with a sulfurized surface along with photographs of R-TiO_2-S, R'-TiO_2-S-4 h and R'-TiO_2-S annealed at 800 °C in an Ar atmosphere through Al reduction. Reprinted with permission from Ref. [123], copyright (2013) American Chemical Society. **c** Evolution from pristine TiO_2 to TiO_{2-x} and to x-doped TiO_{2-x} (x = H, N, S, I). Reprinted with permission from Ref. [124], copyright (2014) Royal Society of Chemistry. **d** TiO_2 obtained by adding 60 mg (sample 1), 120 mg (sample 2), 240 mg (sample 3) and 400 mg (sample 4) Mg powder. Reprinted with permission from Ref. [125], copyright (2017) John Wiley and Sons. **e** $TiCl_4$ solutions in ethanol after adding Zn powder at different ratios and Mg, Al powder (Mg/Al:$TiCl_4$ = 2:1). Reprinted with permission from Ref. [126], copyright (2013) Royal Society of Chemistry

as shown in XRD results and that this lithiation effect with TiO_2 can also occur for oxides such as ZnO, SnO_2 and CeO_2.

3.2.2.2 Al-Based Reduction As for Al-based reduction, Yang et al. [123] prepared a core–shell structured black TiO_2 through a two-step reducing process in which Al powder and pristine TiO_2 were separately placed in an evacuated two-zone furnace at 800 °C (Al) and 500 °C (TiO_2) for 6 h followed by reheating at 600 °C for 4 h under a H_2S atmosphere (1000 Pa) in which a surface disorder layer formed on rutile TiO_2 through the initial molten Al reductive treatment and S atoms were incorporated into the disordered shell under subsequent heating in a H_2S atmosphere (Fig. 17b). Here, these researchers reported that the sulfurized TiO_2 possessed a light brown or black color based on the TiO_2 surface phase and that the black rutile TiO_2-S returned to gray after annealing. Lin et al. [124] also obtained black TiO_2 through a two-step synthesis process involving Al-based reduction and ion doping in which black TiO_{2-x} was initially prepared through Al reduction in a two-zone evacuated furnace at 800 °C followed by reheating at 500 °C for 4 h in atmospheres of hydrogen plasma, S and I_2, and a mixed atmosphere of NH_3 and Ar (2:1) to form H-doped black titania (TiO_2-H), S- and I-doped black titania (TiO_2-S, I), and N-doped black titania (TiO_2-N), respectfully (Fig. 17c).

3.2.2.3 Mg-Based Reduction In terms of Mg-based reduction, Ye et al. [125] prepared colored TiO_{2-x} through calcination at 500, 600 and 700 °C in Ar atmosphere for 4 h under a controlled ratio of TiO_2 and Mg powder and reported that white TiO_2 (P25) gradually changed to gray, blue-gray, light black or dark black with increasing amounts of Mg powder (Fig. 17d). Sinhamahapatra et al. [127] also prepared black TiO_2 through a similar process in which mixed TiO_2 and Mg powder was transferred to a tube furnace and heated at 650 °C for 5 h under a 5% H_2/Ar atmosphere, and reported that the reduced TiO_2 presented different colors based on the amount of Mg powder added.

3.2.2.4 Zn-Based Reduction As an example of Zn-based reduction, Zheng et al. [126] synthesized Ti^{3+} self-doped TiO_2 through a facile Zn powder reduction process and reported that the solution color gradually changed from light blue to dark blue and to black based on the different Zn/$TiCl_4$ molar ratios of 0, 1:8, 1:4, 1:3, 1:2 or 3:4 (Fig. 17e). In addition, these researchers also used Mg and Al powders in place of Zn and reported that the resulting solutions turned light blue and dark blue, respectively. Here, these solutions were transferred into a Teflon autoclave and heated at 180 °C for 24 h to obtain Ti^{3+} self-doped TiO_2.

Table 3 Comparison of reducing agents in the induction of defect structures in TiO_2/LTO

Pristine TiO_2/LTO color	Reductant	Defect TiO_2/LTO color	References
White	$NaBH_4$	Gray and black	[128, 129]
White	C_2H_5OH	Blue or black	[130, 131]
White	CaH_2	Black	[132]
White	N_2H_4	Black	[133]
White	Diethylene glycol	Black	[134]
White	Imidazole	Gray	[135]
White	Electrochemical reduction	Brown or black	[136, 137]

3.2.3 Other Chemical Reduction Processes

In addition to H_2 and metal reducing agents, other reducing agents can also capture oxygen atoms and create defect structures in TiO_2/LTO, resulting in corresponding color changes from white to blue or black (Table 3).

3.2.3.1 $NaBH_4$ As an example of $NaBH_4$ as a reducing agent, Ariyanti et al. [128] prepared defective black TiO_2 through a sealing-transfer reduction process using $NaBH_4$ as a reducing agent followed by annealing at 300–450 °C under an Ar atmosphere for 1 h and reported that white TiO_2 gradually changed to gray and black with increasing temperatures (Fig. 18a). Similarly, Xu et al. [129] also prepared defective black TiO_2 through a $NaBH_4$ high-temperature reducing process at 425 °C for 2 h under an Ar atmosphere.

3.2.3.2 C_2H_5OH As for C_2H_5OH as a reducing agent, Chen et al. [130] were able to prepared black TiO_2 through a facile synthetic procedure in which TiO_2 nanoparticles (0.5 g) were dispersed in ethanol (50 mL) to form a milky-white suspension followed by heating at 400 °C for 3 h, which led to an obvious color change from white to black. Nasara et al. [131] also obtained highly oxygen-deficient $Li_4Ti_5O_{12}$ using a facile C_2H_5OH reducing strategy in which TiO_2 and Li_2CO_3 (a molar ratio of Ti/Li = 5:4) were mixed through wet ball milling and heated to 800 °C for 0–8 h under ambient atmosphere. Here, these researchers reported that anatase TiO_2 tended to transform into a rutile phase and

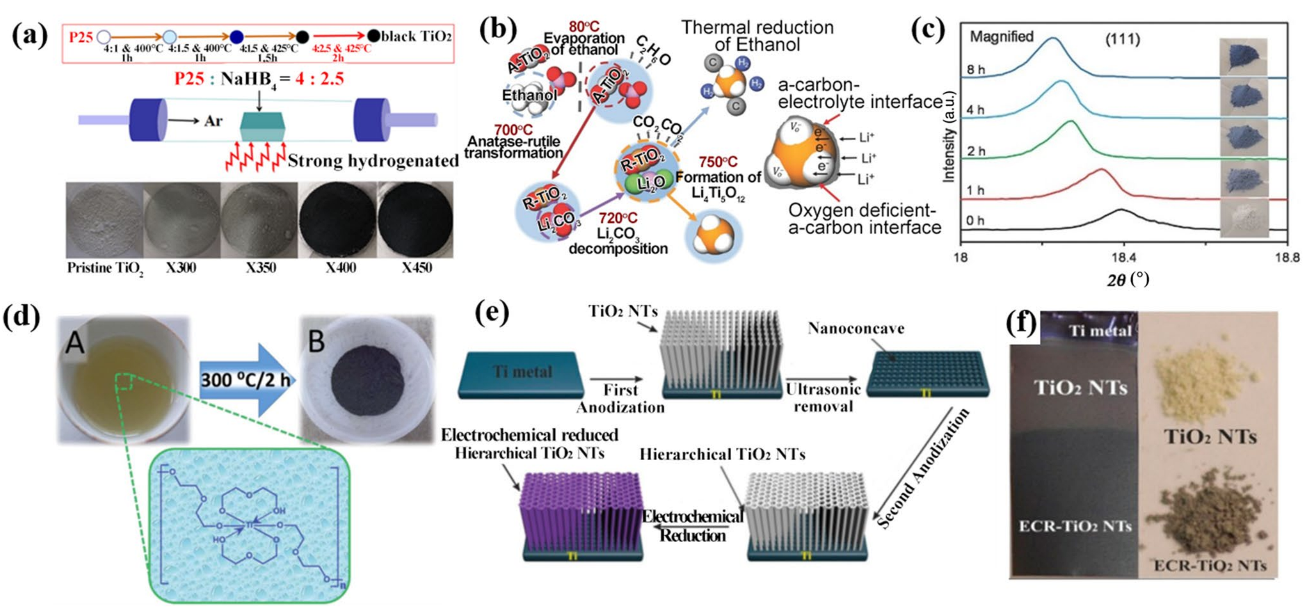

Fig. 18 **a** Schematic for the preparation of black TiO_2 and photographs of colored TiO_{2-x}. Reprinted with permission from Ref. [129], copyright (2017) IOP Publishing. **b** Formation mechanism of defective-LTO and **c** XRD of LTO calcined at 800 °C for various time periods. Reprinted with permission from Ref. [131], copyright (2017) John Wiley and Sons. **d** Photographs of (A) Ti glycolate gel and (B) black anatase TiO_{2-x} with the Ti glycolate gel structure highlighted. Reprinted with permission from Ref. [134], copyright (2016) Royal Society of Chemistry. **e** Ti^{3+} self-doped TiO_2 NT synthesis and **f** photographs of TiO_2 NTs and detached ECR-TiO_2 NT powders. Reprinted with permission from Ref. [136], copyright (2013) Royal Society of Chemistry

Li_2CO_3 will thermally decompose to form CO_2 and Li_2O at high temperatures (Fig. 18b), allowing Li_2O to react with TiO_2 to form $Li_4Ti_5O_{12}$ and the accelerated thermal reduction of C_2H_5OH with evolved CO_2 gas in which the reducing agent can capture oxygen atoms and form highly oxygen-deficient $Li_4Ti_5O_{12-x}$ (Eq. 6). And based on XRD results of LTO at 800 °C with different calcination times, the anatase and rutile-TiO_2 gradually disappeared and transformed into the LTO phase with increasing calcination times, corresponding to a change in the LTO color from light to dark blue (Fig. 18c).

$$C_2H_5OH\,(g) + \text{reducing agent} \xrightarrow{\text{Pressure}} 2C\,(g) + 3H_2\,(g) + \text{oxidized reducing agent} \quad (6)$$

3.2.3.3 CaH_2 In terms of CaH_2, Tominaka et al. [132] synthesized TiO_{2-x} through a simple CaH_2 reducing process involving the mixing of TiO_2 and CaH_2 at a weight ratio of 1:4 under an Ar atmosphere followed by heating at 350 °C for 15 days and the washing of the obtained product with NH_4Cl and drying in air.

3.2.3.4 N_2H_4 Using N_2H_4 as a reducing agent, Mao et al. [133] in their study were able to fabricate higher Ti^{3+} self-doping TiO_{2-x}. In this synthesis process, Ti foil was briefly soaked in an aqueous HCl solution and hydrothermally treated at 220 °C for 18 h. Subsequently, the sample was washed with water, dried in Ar gas and reheated at 550 °C for 150 min under Ar. Finally, the sample was placed in a N_2H_4 solution (20%, 10 mL), preheated at 220 °C for 20 h and washed with water to remove residual N_2H_4 to obtain the final TiO_{2-x}.

3.2.3.5 Organic Reducing Agents In terms of organic reducing agents, Ullattila et al. [134] reported that Ti^{3+} self-doped black TiO_2 can be prepared by using a gel combustion strategy in which by mixing 0.2 M Ti(IV), butoxide (6.8 g) and diethylene glycol (50 mL), a yellow ethyl glycolate gel can be formed. Deionized water (14.4 mL) can subsequently be added to form a hydrated Ti glycolate gel, which if heated in a muffle furnace at 300 °C for 2 h, can produce black TiO_2 (Fig. 18d). In another example, Zou et al. [135] reduced TiO_2 with imidazole in which TiO_2 (0.5 g), imidazole (1 g) and HCl (37 wt%, 3 mL) were mixed, heated at 450 °C for 6 h and cooled to room temperature to form defective TiO_2.

3.2.3.6 Electrochemical Reducing Agents As for electrochemical reducing agents, Zhang et al. [136] prepared Ti^{3+} self-doped TiO_2 through a two-step anodization and one-step reduction process. Here, a Ti sheet was anodized at 60 V for 30 min to remove the as-grown nanotube layer and the resulting nanoconcave Ti sheet was again anodized at 80 V for 5 min and heated at 450 °C for 1 h in air to obtain hierarchical TiO_2 nanotubes (TiO_2 NTs) (Fig. 18e). And during the electrochemical reduction process, the TiO_2 NTs were reduced at − 0.4 V in a 1 M Na_2SO_4 electrolyte for 30 min in which the Ti^{4+} in the TiO_2 NTs captured electrons and converted to Ti^{3+}, causing a color change from white to brown (Fig. 18f). Dong et al. [137] also prepared defective TiO_{2-x} through a similar anodization technique in which a TiO_2 layer was grown on Ti foil through a two-step anodization process at 60 V for 10 h followed by heating at 450 °C for 1 h in ambient atmosphere to obtain black TiO_{2-x}.

3.2.4 Chemical Oxidization

In addition to the reduction of Ti^{4+} to Ti^{3+}, the oxidization of low-valence state Ti (Ti^{2+} or Ti^{3+}) to Ti^{4+} and the maintenance of remaining partial low-valence states (Ti^{2+} or Ti^{3+}) in Ti-based oxides are also effective strategies to produce black defective TiO_{2-x}. Here, because low-valence state Ti (Ti^{2+} or Ti^{3+}) is relatively unstable and prone to being oxidized to Ti^{4+}, reducing agents are needed to ensure the formation of defective structures.

3.2.4.1 TiH_2 As an example of chemical oxidization by using TiH_2, Xin et al. [76] prepared Ti^{3+} self-doped black TiO_2 through a typical oxidization process in which TiH_2, H_2O and H_2O_2 were mixed to form a yellowish gel-like precursor followed by the addition of $NaBH_4$ and heating at 180 °C for 24 h to obtain light blue TiO_{2-x}. This TiO_{2-x} sample was subsequently heated at 300–700 °C for 3 h under a N_2 atmosphere to obtain various colors of TiO_{2-x} (Fig. 19). In other examples, Grabstanowicz et al. [138] conducted a similar oxidative conversion of TiH_2 to black TiO_{2-x} by adding H_2O_2 and Liu et al. [139] prepared Ti^{3+} self-doped TiO_{2-x} nanoparticles through a H_2O_2 oxidation-based method.

3.2.4.2 $TiCl_3$ As for $TiCl_3$, Chen et al. [77] obtained dark-colored rutile TiO_2 using a solvothermal method in which Mg powder, $TiCl_3$ and isopropanol were uniformly mixed and treated with a hydrothermal process at 180 °C for 6 h to form a dark-gray TiO_2 powder. Zhu et al. [140] also prepared blue TiO_{2-x} through a facile solvothermal method in which TiF_4 and $TiCl_3$ were briefly dissolved in anhydrous alcohol and treated with a hydrothermal process at 180 °C for 24 h. These researchers in the same study also prepared a series of Ti^{3+} self-doped TiO_{2-x} samples by controlling the molar ratio of TiF_4 to $TiCl_3$ at 0, 1 : 5, 1 : 20, 1 : 40, 1 : 80 and 1:120, and Zhao et al. [141] prepared blue TiO_{2-x} through a

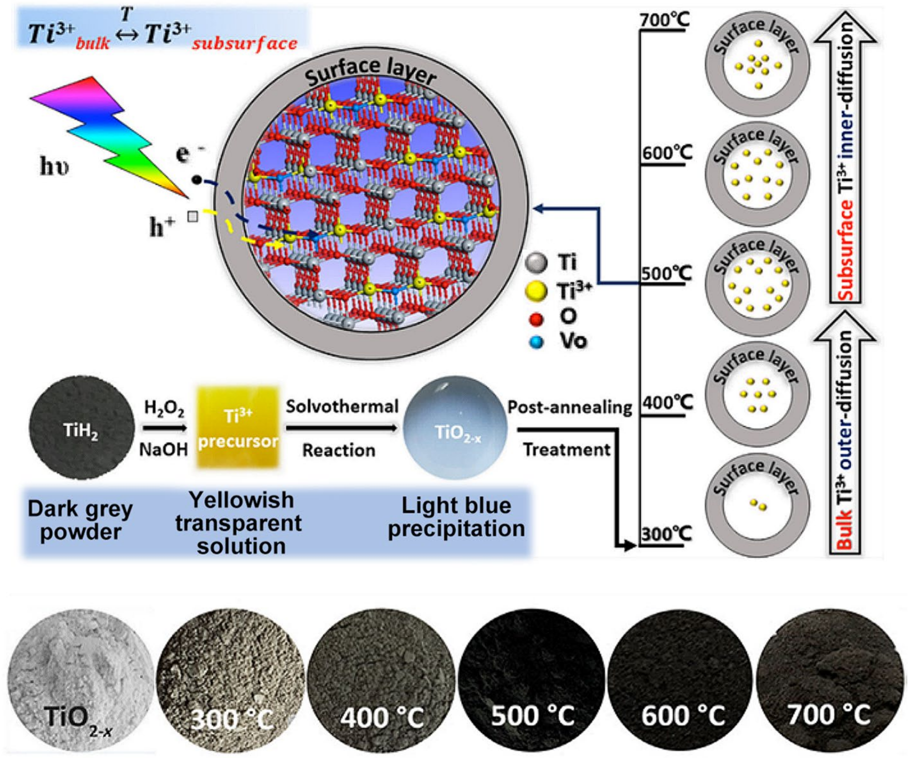

Fig. 19 Mechanism of Ti^{3+} distribution in as-prepared TiO_{2-x} and corresponding images of Ti^{3+} self-doped TiO_2 samples prepared with heating between 300 and 700 °C for 3 h in a N_2 gas flow. Reprinted with permission from Ref. [76], copyright 2015, Elsevier

hydrothermal reaction by mixing $TiCl_3$ with Zn powder in isopropanol.

3.2.4.3 TiO and Ti_2O_3 TiO and Ti_2O_3 can also be used for chemical oxidization. For example, Pei et al. [142] synthesized defective TiO_{2-x} through a simple hydrothermal process in which TiO and HCl solutions were mixed uniformly and treated with a hydrothermal process at 160 °C for 24 h. In another example, Dong et al. [143] prepared Ti^{3+} self-doped $Li_4Ti_5O_{12}$ through a novel solid-state strategy in which a stoichiometric ratio of Li_2CO_3 to Ti_2O_3 was mixed by ball milling for 4 h with ethanol as an additive and annealed at 800 °C for 6 h to obtain Ti^{3+} self-doped $Li_4Ti_5O_{12}$.

4 Characterization of Defects in TiO_2 and LTO

Nanoscale dimensions and extremely low concentrations of defects make their qualitative characterization and quantitative determination difficult. Overall, the most widely used characterization techniques for defects can be classified into scanning probe microscopy (SPM), incident photon-based techniques, incident electron-based techniques, thermal analysis and other techniques. Here, SPM can be directly used to visualize OVs at the nanoscale and molecular level and indirect detection techniques can be applied with the help of incident photons or electrons. However, semiconductors with OVs possess different magnetic and electronic properties, which can lead to changes in spectroscopic response. As for thermal analysis and other related techniques, these can be used to monitor weight changes and reaction products during defect-inducing processes. In general, characterization techniques are powerful tools to investigate the impact of defects on the properties of Ti-based oxides and will be briefly discussed in this session.

4.1 Scanning Probe Microscopy (SPM)

Scanning probe microscopy (SPM) includes a range of techniques that can image surfaces and structures down to the atomic level by using a physical probe to scan samples. During the scanning process, a computer is used to gather data concerning the interaction between probes and surface changes with position in which minor changes in surfaces can greatly alter surface properties and affect interactions, which is the basic mechanism underlying atomic resolutions. And of the various SPM techniques, scanning tunneling microscopy (STM) and atomic force microscopy (AFM) are among the most widely used. As for Ti-based oxides, the conduction and valence bands of TiO_2 are usually dominated by Ti-3d and O-2p orbitals, respectively, and under applied voltage, electrons from the tip of an STM first tunnel to

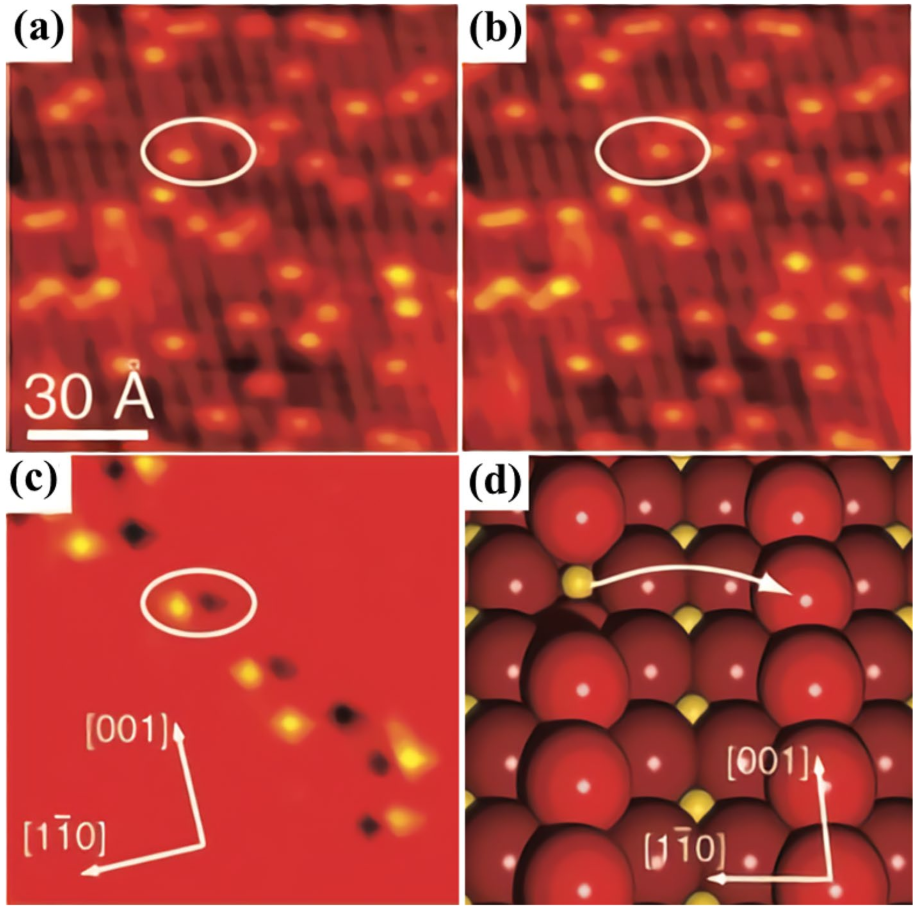

Fig. 20 **a**, **b** Consecutive STM images of TiO_2 with a bridging OV marked by a circle. **c** Difference image constructed by subtracting **b** from **a**. **d** Ball model for the TiO_2 (110) surface. The arrow represents an observed vacancy diffusion pathway. Reprinted with permission from Ref. [144], copyright (2003) American Association for the Advancement of Science

the Ti-3d orbital in the conduction band before being transported away, allowing for the detection of Ti and O atoms (typically represented by bright or dark colors, respectively). Furthermore, OVs can create shallow donor states in band gaps and the Fermi level is elevated next to the conduction band minimum (CBM), causing these defects to appear as bright spots between bright Ti rows. As an example, two STM micrographs of a rutile TiO_2 (110) surface can indicate the existence of a diffusion pathway for OVs, which becomes more evident in the corresponding difference image (Fig. 20a–c, the ball model of this process is presented in Fig. 20d) [144].

4.2 Incident Photon-Based Techniques

4.2.1 X-Ray Diffraction (XRD) Pattern Analysis

As a widely used technique, XRD can detect changes in crystal structure as induced by OVs and dopants in which defects can be confirmed by XRD peak shifts. And unlike techniques that measure properties that have a direct association with OVs, XRD results need to be confirmed with other techniques (XPS, EPR, etc.) to eliminate other possibilities and provide direct evidence of OVs. For example, Choudhury et al. [145] prepared Co-doped TiO_2 nanoparticles and found a slight shift of the (101) peak toward lower angles (Fig. 21a) as well as a larger full width at half maximum (FWHM) in which the decrease in peak intensity confirmed structural irregularity after doping. Here, the altered position of the diffraction peak can be explained by considering the different chemical valence states of Ti^{4+} and Co^{2+} in which as OVs are formed after doping to maintain charge neutrality, changes in the local structure surrounding Co^{2+} ions occur in accordance with other reported studies [146–148]. A similar phenomenon was also observed in defective LTO (Fig. 21b) in which the characteristic blue color as well as the shifting of (111) and (311) peaks toward lower angles was consistent with the presence of OVs as confirmed by XPS [131].

4.2.2 X-Ray Absorption Fine Structure (XAFS) Spectroscopy

The irradiation of samples with high intensity X-ray beams can cause sharp increases in absorption to produce absorption edges at certain energy. The oscillatory feature above the edge is called X-ray absorption fine structure (XAFS) and is caused by interferences between photoelectrons and surrounding atoms [149]. In addition, this energy-dependent

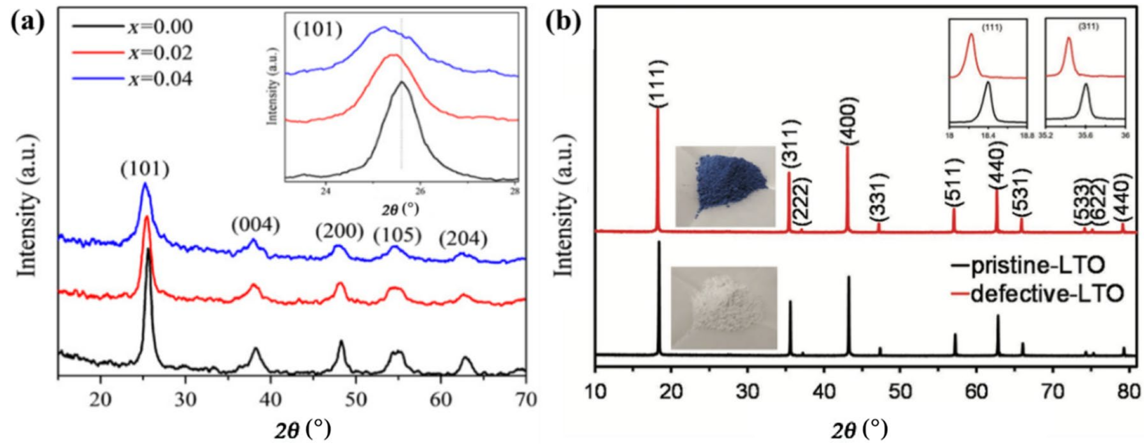

Fig. 21 **a** XRD patterns of undoped and Co-doped TiO_2 nanoparticles. Reprinted with permission from Ref. [145], copyright 2012, Elsevier. **b** Pristine and defective LTO synthesized in a reducing atmosphere at 800 °C under high pressure. Reprinted with permission from Ref. [131], copyright (2017) John Wiley and Sons

variation in the X-ray absorption spectrum can be divided into X-ray absorption near-edge spectroscopy (XANES) and extended X-ray absorption fine-structure spectroscopy (EXAFS) in which the former (from the edge to 30–50 eV) contains information concerning the electronic structure and the oxidation state of absorbing atoms, whereas the latter (from 30–50 eV to 1000 eV) is sensitive to the bond length, the coordination number and surrounding species of absorbing lattice atoms. Here, the presence of defects can change the coordination number and the chemical bond length of Ti–O to alter the chemical environment of nearby atoms, and therefore, XAFS can be an effective technique to investigate defects in TiO_x.

For example, Wu et al. [74] investigated the transformation of Ti^{4+} local structures induced by OVs using XANES and EXAFS and reported three low-density pre-edge peaks (A_1, A_2, A_3) characteristic of the octahedral coordination of Ti (Fig. 22a). Here, these researchers attributed this to the transition from the Ti 1s orbital to different molecular orbitals ($1t_{1g}$, $2t_{2g}$ and $3e_g$) [150, 151]. In addition, these researchers reported that as compared with pure TiO_2, a new absorption shoulder peak (T_{tet}) between A_1 and A_2

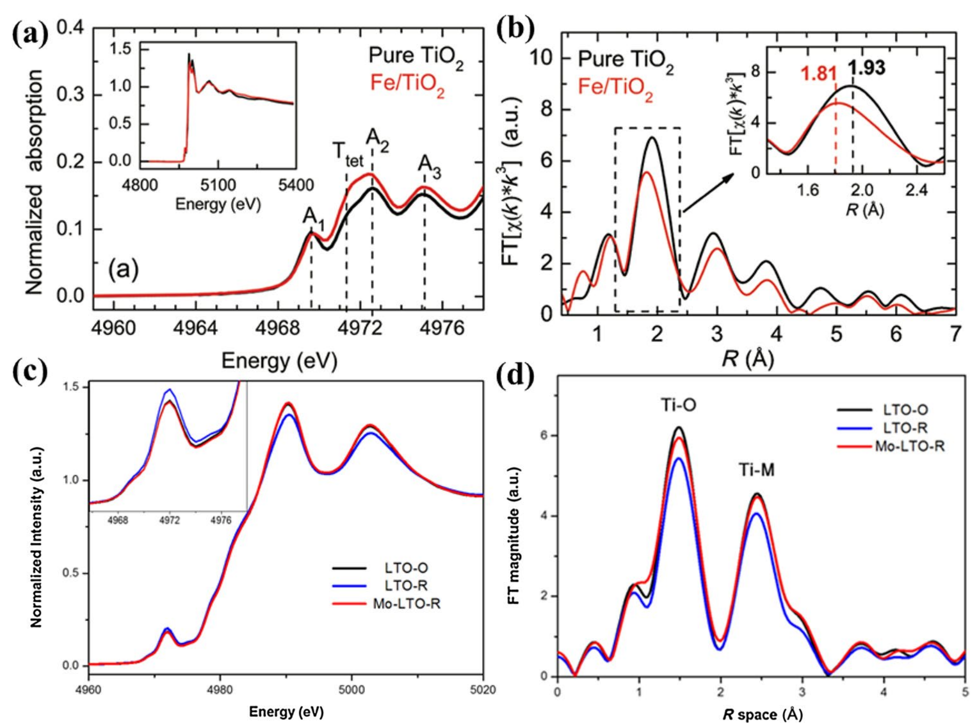

Fig. 22 **a** Ti K-edge XANES spectra and **b** the magnitude component of Fourier transformed k^3-weighted χ (k) of the Ti K-edge EXAFS spectra for pure TiO_2 and Fe-doped TiO_2. Reprinted with permission from Ref. [74], copyright (2012) American Chemical Society. **c** Ti K-edge XANES spectra and **d** EXAFS spectra of undoped $Li_4Ti_5O_{12}$ in an oxidizing atmosphere (LTO-O), undoped $Li_4Ti_5O_{12}$ in a reducing atmosphere (LTO-R) and Mo-doped $Li_4Ti_5O_{12}$ in a reducing atmosphere (Mo-LTO-R). Reprinted with permission from Ref. [155] under Creative Commons

can be observed for Fe-doped TiO_2, indicating the presence of tetrahedrally coordinated Ti ions in which Ti ions remained in the form of Ti^{4+} instead of Ti^{3+} because the first maximum of the first derivative for the main edge jump did not shift to lower energy [152, 153]. These researchers also reported that the Ti–O bond length shrank from 1.93 to 1.81 Å (Fig. 22b), which is close to the Ti–O distance in TiO_4 tetrahedra [150, 154], clearly providing evidence of the existence of tetrahedrally coordinated Ti^{4+}. In another example, Song et al. [155] used XANES to study changes in the OV concentration in $Li_4Ti_5O_{12}$ in which the obtained pre-edge peak centered at 4972 eV corresponded to the pure electric quadrupole 1s → 3d transition and the peak for LTO-R was found to be higher than that for LTO-O, indicating the increased distortion of the TiO_6 octahedral structure for LTO-R (Fig. 22c). Here, these researchers suggested that the intensity of the pre-edge peak was directly related to a break in central symmetry, which can be attributed to OVs, demonstrating that LTO-R possesses a higher OV content. The same conclusion was also drawn after analyzing the peak position at ~ 4990 eV, which represented the 1s → 4p transition in which the hybridization of Ti $p - t_{2g}$ orbitals was enhanced due to severer distortions, leading to the lower probability of 1s → 4p transition. Furthermore, the results of the Ti K-edge EXAFS analysis in this study also demonstrated that the distortion of the TiO_6 octahedral structure in LTO-R was intenser than that in the other two (as calculated by using Debye–Waller factors) (Fig. 22d) [155].

4.2.3 X-Ray Photoelectron Spectroscopy (XPS)

XPS, also known as electron spectroscopy for chemical analysis (ESCA), is a quantitative technique to analyze the surface of a sample and provide information concerning elemental composition, chemical valence states, electronic states and so on. The basic principle of XPS is to simultaneously measure kinetic energy and the number of photoelectrons ejected from a surface through monoenergetic X-rays (for Al Kα X-rays, $h\nu = 1486.7$ eV) under high vacuum conditions in which the kinetic energy (E_K) of electrons depends on the irradiating photon energy ($h\nu$), the binding energy (E_B) between electrons and nuclei relative to the Fermi level and the work function (ϕ), which is an adjustable instrumental correction factor calculated by using Eq. 7 [156]:

$$h\nu \rightleftharpoons E_K + E_B + \phi \tag{7}$$

And based on the value of E_B and the chemical shift, elemental composition and chemical bonding states can be calculated quantitatively because binding energy is related to the structure of electron shells and the surrounding environment of atoms in question. For example, Kang et al. [157] studied TiO_2 nanotube arrays (NTAs) with OVs prepared through $NaBH_4$ treatment using XPS and reported similar shifts of O 1s and Ti 2p, indicating the migration of electrons from O and Ti ions to OVs that can be regarded as electron traps (Fig. 23a, b). These researchers also used valence band XPS (VBXPS) to investigate the density of states (DOS) and the occupation of electronic states in the valence band and reported that the introduction of OVs can lead to the narrowing of band gaps from 2.03 to 1.50 eV as well as the presence of a slight band tail at ~ 0.97 eV (Fig. 23c). Here, these researchers suggested that the band tail represented localized defect states in the band gap at 0.75–1.18 eV below the CBM (Fig. 23d). In addition to peak shifts and defect states, XPS can also be used to confirm the existence of defects through peaks in deconvolved spectra [158] in which new peaks were observed at 684.8 eV (F^-) [148], 485.8 eV (Sn^{2+}) and 486.4 eV (Sn^{4+}) [159] as compared with pristine TiO_2. And as for reference $Li_4Ti_5O_{12}$ (R-LTO), the deconvolved XPS spectrum could only be fitted with two single peaks, implying that all Ti ions were Ti^{4+} (Fig. 23e), whereas for LTO with OVs (Fig. 23f), each of the two peaks could be deconvolved into two component peaks, indicating the existence of Ti^{3+} that formed with OVs through Eq. 8:

$$Li_4Ti_5O_{12} \xrightarrow{H_2\ \text{atmosphere}} \frac{x}{2}O_2(\text{gas}) + xV_O^{\cdot\cdot} + Li_4\,Ti_{2x}^{3+}O_{12-x} \tag{8}$$

4.2.4 Raman Spectroscopy

Raman spectroscopy is a nondestructive technique based on the inelastic scattering of monochromatic light, usually from a high-intensity laser source in which laser light photons are initially absorbed by analyte and subsequently reemitted. This reemitted light of the same wavelength as the laser source is called the Rayleigh scattered light (elastic scattering) and does not contain structural information concerning samples but does constitute most of the scattered light. Here, only a small proportion of photons shift up or down frequencies due to interactions with chemical bonds in materials. These photons are called Raman scattered light (inelastic scattering), and changes in frequency can provide information concerning vibrational, rotational and other low-frequency transitions in samples [160]. In terms of TiO_2, the main Raman active mode centered around 142 cm^{-1} (E_g) possesses a blueshift and a larger FWHM for partially reduced TiO_2 that becomes more evident with increasing reaction temperatures (Fig. 24a) [161]. This phenomenon is generally attributed to the small size effect of crystalline grains (< 10 nm) or the decreased correlation lengths as induced by defects in which the former can be excluded because the size of nanoparticles is not less than 19 nm. And considering that the liquid reduction process does not introduce any impurities as shown in energy dispersive X-ray results (Fig. 27a), the only practical conclusion is that OVs

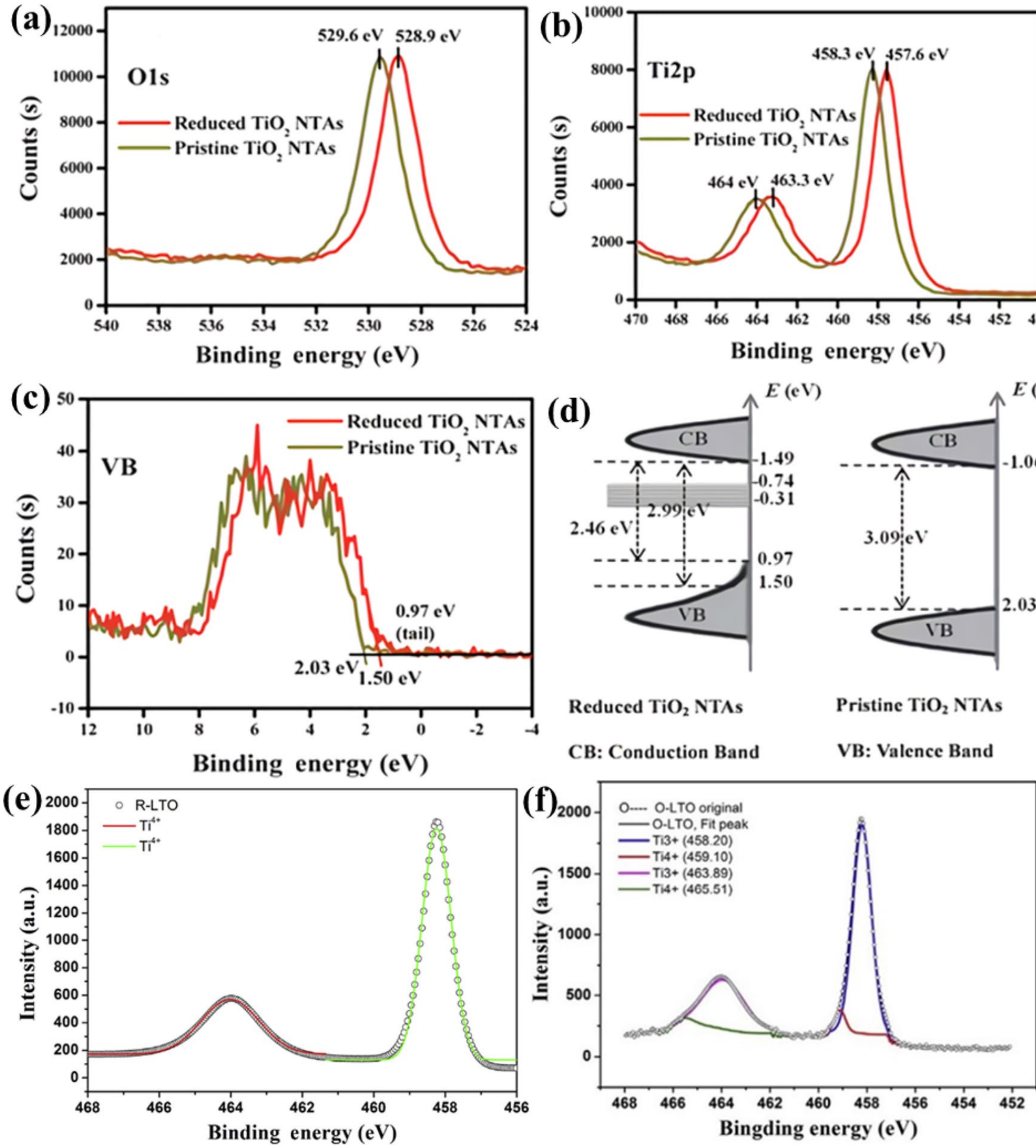

Fig. 23 **a** O 1s, **b** Ti 2p and **c** valence band XPS spectra of pristine and NaBH$_4$ reduced TiO$_2$ NTAs. **d** Schematic of the DOS of reduced and pristine TiO$_2$ NTAs. Reprinted with permission from Ref. [157], copyright 2013, Royal Society of Chemistry. **e** Deconvolved XPS spectra of reference Li$_4$Ti$_5$O$_{12}$ (R-LTO) and **f** Li$_4$Ti$_5$O$_{12}$ with OVs (O-LTO) synthesized under 5 vol% H$_2$/Ar atmosphere. Reprinted with permission from Ref. [158], copyright 2017, Elsevier

led to the blueshift and larger FWHM. Furthermore, a similar blueshift at 144 cm^{-1} can also be observed in F-doped TiO$_2$ [148], and as for Li$_4$Ti$_5$O$_{12}$ nanoparticles [162], the Raman peaks possess a blueshift from 674 to 680 cm^{-1}, which corresponds to the Ti–O vibration mode (Fig. 24b), meaning that more OVs are produced under an Ar/H$_2$ reducing atmosphere (8% mol). Moreover, the correlation between shifts/broadening of Raman peaks and the presence of OVs has also been observed in other studies [74, 163–165].

4.2.5 Fourier Transform Infrared (FTIR) Spectroscopy

FTIR spectroscopy can be used to obtain the spectra of infrared light absorption or emission in samples. Here, different vibration modes of various bonds can selectively absorb the radiation of specific wavelengths and these wavelengths can cause changes in dipole moments and elevate vibrational energy levels in which the frequency of absorption peaks is based on the vibrational energy gap between ground states and excited states. In addition, the number of vibrational

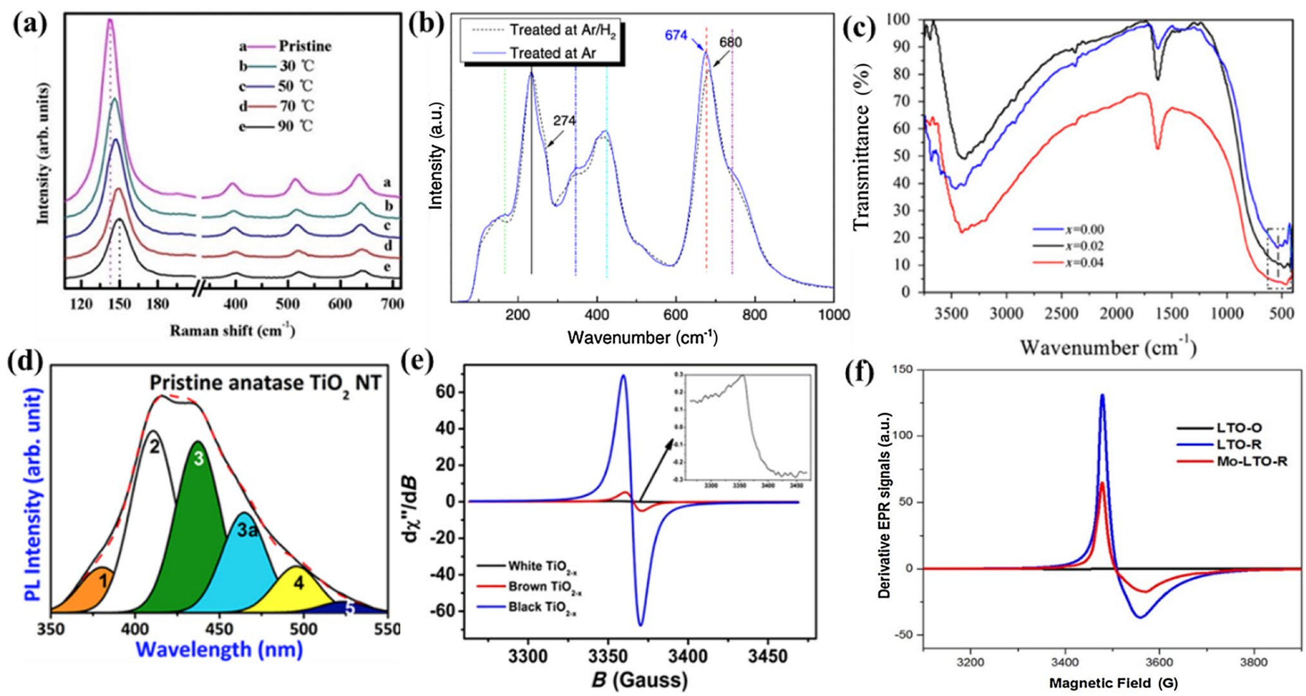

Fig. 24 **a** Raman spectra of the pristine anatase phase of TiO_2 nanotube arrays (TNAs) and partially reduced TNAs (PR-TNAs) in $NaBH_4$ solution at different temperatures. Reprinted with permission from Ref. [161], copyright 2015, IOP Publishing. **b** Raman spectra of $Li_4Ti_5O_{12}$ synthesized under different atmospheres. Reprinted with permission from Ref. [162], copyright 2011, Springer Nature. **c** FTIR spectra of undoped and Co^{2+} doped TiO_2 nanoparticles. Reprinted with permission from Ref. [145], copyright 2012, Elsevier. **d** Gaussian peak fitted PL spectra of TiO_2 nanotubes. Reprinted with permission from Ref. [166], copyright (2017) American Chemical Society. **e** EPR spectra of defective TiO_2 nanoparticles reduced by L-ascorbic acid (0, 0.3 and 0.7 g corresponding to white, brown and black TiO_{2-x}). Reprinted with permissions from Ref. [167] under Creative Commons. **f** Derivative EPR spectra of undoped LTO in oxidizing (LTO-O) and reducing atmospheres (LTO-R) as well as Mo-doped LTO in reducing atmosphere (Mo-LTO-R). Reprinted with permissions from Ref. [155] under Creative Commons

freedom degrees of chemical bonds can determine the number of absorption peaks. Therefore, by analyzing FTIR spectra, vibration modes in TiO_2 or $Li_4Ti_5O_{12}$ crystal lattices can be investigated, which are affected by synthesis conditions, doped ions, presence of OVs, etc. Furthermore, FTIR spectroscopy can be used to confirm the presence of OVs in doped Ti oxides. In general, absorption peaks around 400–800 cm^{-1} can be attributed to the bending and stretching vibration modes of Ti–O–Ti and Ti–O bonds [168, 169]. For example, Choudhury et al. [145] found a redshift for doped TiO_2 nanoparticles in the peak position of Ti–O from 454 cm^{-1} (undoped TiO_2) to 425 cm^{-1} and 423 cm^{-1} (0.02 and 0.04 Co^{2+}-doped TiO_2, respectively) (Fig. 24c). And because of charge neutrality, OVs were undoubtedly introduced into the Co^{2+}-doped samples, which can decrease the number of O ions available to form chemical bonds with metal ions, meaning bond strengths and force constant values (k) will decrease according to Eq. (9):

$$\nu = \frac{1}{2\pi c}\left(\frac{k}{\mu}\right)^{\frac{1}{2}} \tag{9}$$

in which ν is the wave number, k is the force constant of the chemical bond and μ is the reduced mass of the bond associated with the elements, meaning that lowered k or increased μ will lead to redshifting in corresponding FTIR peaks. Similar results for redshifting in FTIR spectra peaks were also reported for Zn- and Mn-co-doped TiO_2 [170].

4.2.6 Photoluminescence (PL) Spectroscopy

Photoluminescence (PL) is a process in which electrons are excited to higher electronic states after absorbing photons and subsequently return to lower energy states and radiate photons. PL spectroscopy can allow for the characterization of properties at the surface/interface of samples, especially those related to impurities and defects. For example, Sarkar et al. [166] conducted room-temperature PL emission spectra for TiO_2 nanotubes by exciting samples with 325 nm wavelength photons. Here, the obtained Gaussian curve fitted PL spectra (Fig. 24d) showed several peaks in which peak 1, positioned around 380 nm (3.26 eV), matched well with the band gap energy of anatase TiO_2 whereas peak 2 (411 nm, 3.01 eV) and peak

4 (496 nm, 2.5 eV) can be assigned to free exciton recombination and band tails, respectively, and peak 3 (437 nm, 2.84 eV) and peak 5 (523 nm, 2.37 eV) are related to surface defects or surface OVs, which can further become F and F^+ centers. In addition, these researchers suggested that peak 3a centered around 465 nm (2.66 eV) originated from shallow and deep surface traps, which are associated with Ti^{3+} states that are a result of the combination of electrons in F centers and adjacent Ti^{4+} ions based on Eqs. (10–13) [171]:

$$V_O + 2e^- \rightleftharpoons F \tag{10}$$

$$F + Ti^{4+} \rightleftharpoons F^+ + Ti^{3+} \tag{11}$$

$$V_O + e^- \rightleftharpoons F^+ \tag{12}$$

$$Ti^{4+} + e^- \rightleftharpoons Ti^{3+} \tag{13}$$

And as a result of these findings, it can be confirmed that visible light PL emission peaks in TiO_2 are closely related to OV defects. Moreover, researchers have also reported that for Co-doped TiO_2, an obvious decrease in intensity ratios of UV to visible emission peaks with dopant concentration can be observed [145].

4.2.7 Electron Paramagnetic Resonance (EPR)

Electron paramagnetic resonance (EPR), also known as electron spin resonance (ESR), is another powerful and nondestructive method to study materials with unpaired electrons based on the fact that every electron possesses a magnetic moment and a spin quantum number ($m_s = \pm 1/2$). Here, in the presence of an external magnetic field (B_0), separation between lower and upper states of unpaired electrons occurs with energy differences being calculated based on $\Delta E = g\ \mu_B B_0$ in which g is the Landé g-factor, μ_B is the Bohr magneton ($\mu_B = e\hbar/2m_e = 5.7884 \times 10^{-5}$eV T^{-1}), and B_0 is the strength of the applied magnetic field. And based on this equation, the splitting of energy levels is directly proportional to the strength of the applied magnetic field. In addition, unpaired electrons can move between two energy levels by absorbing or emitting photons with a frequency of v with the condition $\Delta E = hv$ (h is Planck's constant). Based on this, the fundamental equation of EPR spectroscopy is: $hv = g\ \mu_B B_0$. Moreover, aside from original absorption spectra, the first derivative of EPR signals is the most common method to report results. Overall, multiple studies have confirmed that EPR is an extraordinarily powerful technique to identify OVs and OV-related defect states [155, 158, 167, 172–177] in which for reduced TiO_2 nanoparticles, F^+ centers (OVs containing a single electron) and Ti^{3+} ([Ar]$3d^1$) can be directly detected. And based on Eq. (11) in which Ti^{3+} ions are formed after Ti^{4+} ions gain an electron from adjacent OVs (F centers), the presence of Ti^{3+} ions can be regarded as a sign of the presence of OVs. For example, defective TiO_{2-x} and Mo-doped $Li_4Ti_5O_{12}$ samples show strong EPR signals around $g = 2$, which can be ascribed to single electron-trapped OVs (F^+ centers) (Fig. 24e, f), and in general, g values around 1.96–1.99 correspond to Ti^{3+} ions on surfaces. Furthermore, large increases in EPR signal intensities for brown and black TiO_{2-x} can also indicate the increased production of OVs with increasing reduction from L-ascorbic acid (Fig. 24e). Similar increases can also be observed for LTO-O (in oxidizing atmosphere) and LTO-R (in reducing atmosphere) (Fig. 24f). Alternatively, the EPR signal intensity for Mo-doped LTO is markedly lower than that for LTO-R however, indicating a decrease in OVs. This can be explained by the fact that because the Mo dopant is in its Mo^{6+} state (confirmed by XPS), the partial reduction of Ti^{4+} ions is caused by charge compensation (the high valence dopant) similar to n-type doping rather than the introduction of OVs in reducing atmospheres.

4.3 Incident electron-based techniques

4.3.1 Positron Annihilation Spectroscopy (PAS)

Positron annihilation spectroscopy (PAS) is a nondestructive technique with high sensitivity to voids and defects in solids, especially to those that cannot be detected with other characterization methods. PAS operates on the principle that as a positron interacts with its antiparticle electron, they annihilate and release gamma rays that can be detected. Here, the lifetime of a positron can be calculated by recording the time difference between the emission of positrons from the radioactive source (e.g., ^{22}Na) and the detection of the produced gamma rays. And because positrons prefer to be trapped by atomic defects, leading to different lifetimes and diffusion lengths, these results can provide information concerning the electronic environment of annihilation sites, which correspond to various vacancies with different sizes, concentrations and so on. Overall, the three widely performed PAS techniques include positron annihilation lifetime spectroscopy (PALS), Doppler broadening spectroscopy (DBS) and angular correlation of annihilation radiation (ACAR). As an example, Jiang et al. [111] investigated the OVs of pristine and hydrogenated TiO_2 using PALS and found that in the obtained spectra, the first component (τ_1) represented the free annihilation of positrons in a defect-free crystal (Fig. 25) in which for pristine TiO_2, monovacancies naturally existed in the crystal lattice and τ_1 was 140.5 ps, whereas τ_1 for hydrogenated TiO_2 was significantly longer at 188.1 ps, with an increase of over 33%. And because OVs or shallow positron traps can

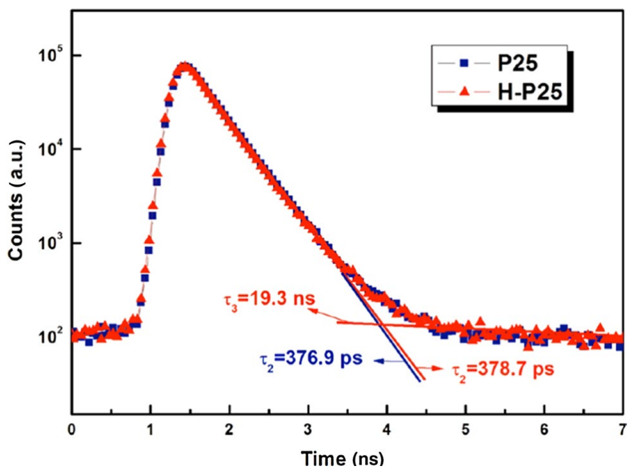

Fig. 25 Positron lifetime spectra with fitting lines for pristine (P25, blue) and hydrogenated (H-P25, red) TiO_2 nanoparticles. Reprinted with permission from Ref. [111], copyright (2012) American Chemical Society

reduce surrounding electron density, positron lifetimes and diffusion lengths are increased, meaning that the prolonged τ_1 of hydrogenated TiO_2 can demonstrate the existence of large numbers of Ti^{3+}-OVs in TiO_2 lattices as induced by hydrogenation. These researchers also reported that the corresponding relative intensity (I_1) also increased from 11.22% to 14.30% after reduction and that the longer lifetime component (τ_2) belonged to positrons captured by larger-sized defects (boundary-like defects) in which the average electron density is much lower than that in smaller-sized defects, leading to decreases in annihilation rates and remarkable increases in positron lifetime. And because of a larger percentage of boundary-like defects as compared with monovacancies, the relative intensity possesses the relation $I_2 > I_1$. As for the longest lifetime component (τ_3), these researchers reported that this was only detected in the hydrogenated sample at extremely low relative intensity, which they attributed to the annihilation of orthopositronium atoms in which the intensity was so low that the few voids of OV associates were created in the grains of hydrogenated TiO_2. As a result, OVs led to comparatively low nearby electron densities and therefore increased the value of τ_1. In addition, OV associates can form larger size clusters, which explains the longer lifetime components (τ_2 and τ_3) (Table 4).

4.3.2 Transmission Electron Microscopy (TEM)

Transmission electron microscopy can directly visualize atoms by using transmitting electrons through a specimen at high resolutions due to the small de Broglie wavelength of electrons. Here, spherical aberration corrected high-resolution transmission electron microscopy (C_s-corrected HRTEM) and spherical aberration corrected scanning transmission electron microscopy (STEM) are among the most widely used techniques in which the latter can be used with different detectors to obtain high-angle annular dark-field (HAADF), annular bright-field (ABF) and annular dark-field

Table 4 Positron lifetimes and relative intensities of pristine and hydrogenated TiO_2 nanoparticles. Reprinted with permission from Ref. [111], copyright (2012) American Chemical Society

Sample	τ_1 (ps)	τ_2 (ps)	τ_3 (ns)	I_1 (%)	I_2 (%)	I_3 (%)
Pristine TiO_2	140.5	376.9	NA	11.22	88.78	NA
Hydrogenated TiO_2	188.1	378.7	19.3	14.30	85.45	0.25

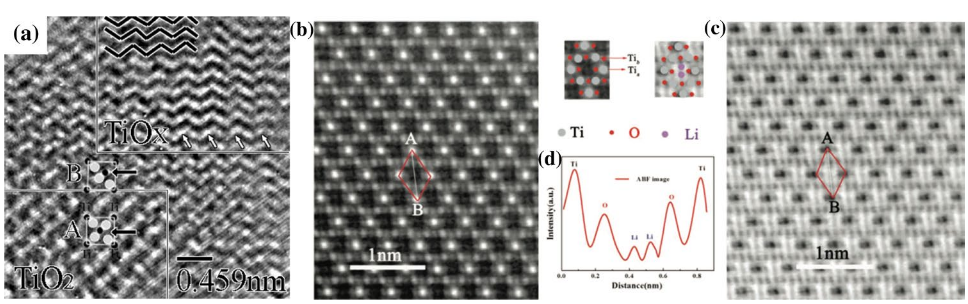

Fig. 26 **a** C_s-corrected HRTEM image of TiO_2 and reduced TiO_x [178]. **b** Enlarged HAADF-STEM image of $Li_4Ti_5O_{12}$. **c** ABF-STEM image and **d** the corresponding line profile of $Li_4Ti_5O_{12}$ along the [110] zone axis. The image contrast of the dark dots is inverted and represented as peaks. Reprinted with permission from Ref. [179], copyright (2012) John Wiley and Sons

(ADF) STEM images, all of which are effective and possess better image resolution, sensitivity and improved signal to noise ratios as compared with conventional TEM. For example, Yoshida et al. [178] obtained HRTEM images of TiO_2 and reduced TiO_x (Fig. 26a) in which small black and large white dots represented Ti and O atoms, respectively, and reported that as compared with pristine TiO_2 (marked "A"), one O atom was missing in the reduced TiO_x (marked "B"), thus providing direct evidence of OVs in TiO_2. Similar conclusions were also obtained in other studies (Fig. 26b, c) [179], and corresponding line profiles (Fig. 26d) can also reveal atom distributions on the surface with two pronounced Li^+ ion peaks.

4.3.3 Energy-Dispersive X-Ray Spectroscopy (EDS)

Energy-dispersive X-ray spectroscopy (EDS, EDX, EDXS or XEDS), sometimes referred to as energy dispersive X-ray analysis (EDXA) or energy dispersive X-ray microanalysis (EDXMA), is a surface analytical technique that uses an electron beam to eject electrons into inner shells to create electron holes. Electrons from the outer shell will subsequently fill these holes and release the energy difference in the form of X-rays. Here, the energy signature of this emission is unique for each element and can be detected by an energy-dispersive spectrometer. In principle, all elements from the atomic number 5 (Boron) to 92 (Uranium) can be detected with poorer accuracy for "lighter" elements (atomic number less than 10). And in general, EDS is coupled with SEM, TEM or STEM. For example, Zhang et al. [161] in their study on the reduction of TiO_2 nanotube arrays used EDS to demonstrate that the $NaBH_4$-based reducing process is pollution free with no impurities introduced (Fig. 27a, b) in which EDS revealed that a decrease in the atomic ratio of O : Ti with higher reduction temperatures originated from increasing OVs and that the non-integral stoichiometric ratio of O : Ti (1.97 : 1) was mainly due to the annealing process (low temperature and short annealing time in air). EDS can also be regarded as a tool to indirectly assist in the determination of oxygen defects provided that other possibilities are excluded. In addition, EDS can provide information concerning atomic composition (%) and can easily detect doped cations and anions such as Co^{2+} [145], Mo^{6+} [180], F^- [181] and N^{3-} [182].

4.3.4 Electron Energy Loss Spectroscopy (EELS)

When a beam of electrons with specific kinetic energy passes through a thin sample, the majority of electrons can interact elastically with the sample and a fraction will lose

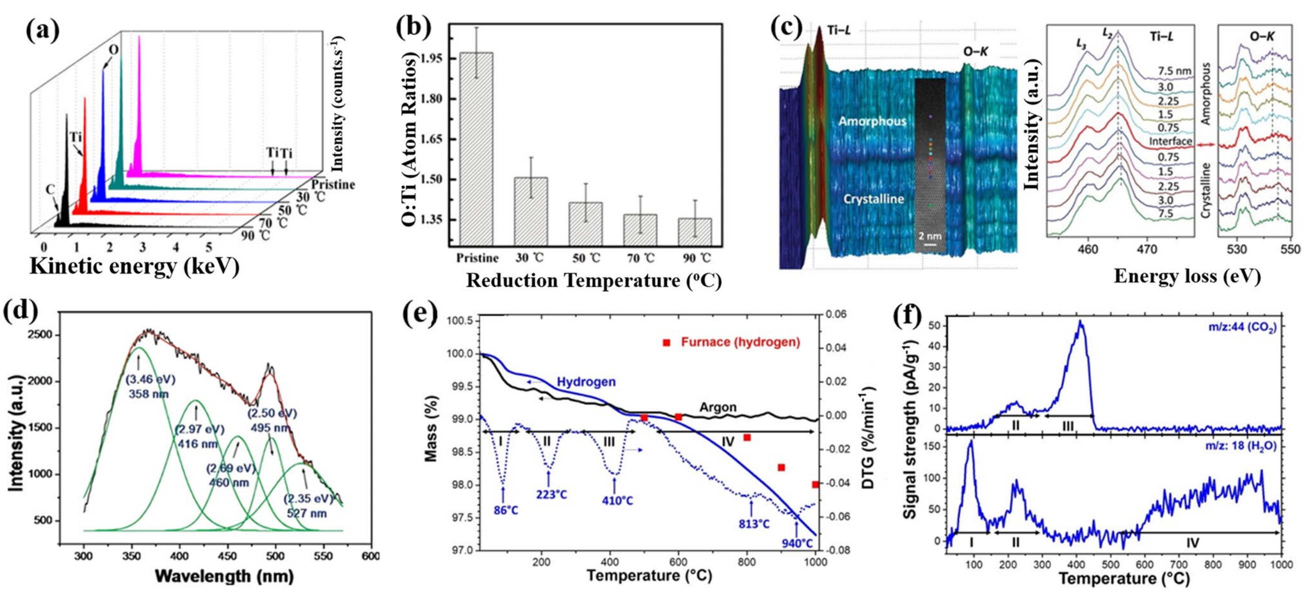

Fig. 27 **a** EDS spectra and **b** corresponding variations of O : Ti atom ratios for pristine and $NaBH_4$-reduced TiO_2 nanotube arrays at different temperatures. Reprinted with permission from Ref. [161], copyright 2015, IOP Publishing. **c** 3D EELS spectra with the STEM image marked with positions in which EELS spectra were recorded in the left panel, and corresponding EELS spectra for Ti-$L_{2,3}$ and O-K edges were recorded at various positions in the right panel. Reprinted with permission from Ref. [183], copyright (2016) American Chemical Society. **d** Cathodoluminescence spectra and Gaussian fitting results for sputter-deposited TiO_2 nanowires. Reprinted with permission from Ref. [159], copyright (2010) American Chemical Society. **e** Thermal gravimetric analysis (TGA) and derivative thermogravimetry (DTG) of LTO nanoparticles under Ar or H_2 atmosphere and **f** mass spectra signals of CO_2 and H_2O during annealing under H_2 atmosphere. Reprinted with permissions from Ref. [186], copyright John Wiley and Sons

energy and see their paths slightly deflected. This deflection is related to the structure and chemical state of the sample atoms as well as their neighboring environment. As a result, these properties can be measured by an electron spectrometer and can be typically incorporated into TEM or STEM. Overall, electron energy loss spectroscopy (EELS) is a powerful technique to analyze changes in kinetic energy distribution with much higher sensitivity as compared with EDS, especially for elements with smaller atomic numbers. For example, Lü et al. [183] fabricated TiO_2 bilayer thin films with a crystalline core and an oxygen-deficient amorphous shell through pulsed laser deposition (PLD) and were able to simultaneously record Ti-$L_{2,3}$ and O-K spectra using STEM–EELS (Fig. 27c). And based on previous studies [184, 185], Ti-L and O-K edges are sensitive to the existence of Ti^{3+} and OVs, respectively, in which the obtained STEM-EELS in this study showed that the Ti-L_2 peak shifts by ~ 0.5 eV from the core up to the surface, revealing the presence of Ti^{3+} ions from the amorphous surface to the crystalline lattice within 3 nm including the interface. A similar shift was also observed in the amorphous layer and the interface in the O-K spectra. And because the spectra in the crystalline side do not change with depth, this confirms that areas with high crystallinity contain fewer OVs. Furthermore, similar results were also observed in hydrogenated black TiO_2 [174].

4.3.5 Cathodoluminescence (CL) Spectroscopy

Cathodoluminescence (CL) is the emission of photons of a characteristic wavelength from a material in response to electron radiation. In essence, this phenomenon is the radiative recombination of electron–hole pairs as induced by incident electrons. Compared with optical characterization techniques, CL spectroscopy possesses several advantages in terms of spatial resolution and the association of morphology and structure, such as size, shape, composition, crystallography, electronic properties and much more. These advantages make CL spectroscopy a powerful characterization technique to study OVs. For example, Wu et al. [159] obtained the CL spectra and Gaussian fitting curves of sputter-deposited anatase TiO_2 nanowires (Fig. 27d) and found that the dominant peak centered at 358 nm originated from band-to-band emission, indicating a direct band gap of 3.46 eV. Here, these researchers attributed this blueshift as compared with the generally reported band gap of ~ 3.20 eV (387 nm) to the quantum confinement effect. These researchers also attributed the peak positioned at 416 nm (2.97 eV) to self-trapped excitons localized on the TiO_6 octahedra and the peaks centered at 460 nm (2.69 eV) and 527 nm (2.35 eV) to self-trapped excitons in F (an oxygen-ion vacancy occupied by two electrons) and F^+ (an oxygen-ion vacancy occupied by one electron) centers, respectively. Furthermore, the peak at 495 nm (2.50 eV) was attributed to surface defect states as induced by OVs.

4.4 Thermal Analysis and Other Techniques

Thermal analysis includes a series of techniques in which the property of a sample (such as heat flow, weight loss and mechanical properties) is continuously measured as a function of temperature. And among these methods, thermal gravimetric analysis (TA) and differential scanning calorimetry (DSC) are the most widely used techniques. In addition, because the OV formation process can lead to changes in mass that can be quantitatively measured, thermal analysis can also be used to monitor the presence of OVs under certain circumstances. For example, Widmaier et al. [186] used thermal analysis to study mass change in LTO during annealing under H_2 atmosphere (Fig. 27e) in which they attributed the observed peaks centered at 86 °C and 223 °C to water desorption [187, 188] and the third peak positioned at 410 °C to the decomposition of carboxylic groups on the LTO surface and/or the decomposition of impurities. These researchers also reported that at temperatures over 450 °C, no obvious changes were observed for the mass curve of LTO under Ar atmosphere but that continuous decreases for LTO under H_2 atmosphere at 450–1000 °C as well as simultaneous water desorption occurred (Fig. 27f). This phenomenon can only be explained by the reaction of H_2 with lattice oxygen producing OVs and H_2O, which can be expressed with the Kröger–Vink notation:

$$H_2(g) + O_O^{\times} \rightleftharpoons H_2O(g) + V_O^{\cdot\cdot} \quad (14)$$

And by analyzing the derivative thermogravimetry (DTG) curve (Fig. 27e), these researchers reported that oxygen atoms located in low-energy lattice sites were gradually removed at temperatures over 450 °C until temperatures reached 813 °C and that the removal of oxygen atoms located at high-energy lattice sites can be activated at temperatures over 813 °C before achieving a new balance at 940 °C.

As with thermal analysis, many other methods exist to detect the formation of oxygen defects and estimate the amount of oxygen deficiencies under specific conditions. These techniques including temperature-programmed desorption (TPD), temperature-programmed reduction (TPR) and oxidation (TPO) [189, 190]. Overall however, these methods do not directly detect OVs or their characteristic properties, which limits application.

5 Theoretical Aspects of Defects in TiO_2 and LTO

Slight defects have little effect on crystal lattices but can greatly affect the electronic structure and electrochemical properties of materials (e.g., conductivity and ion transport). And although electronic structures can roughly be studied through experimental techniques, theoretical investigations by using computational techniques are necessary, especially for the understanding of mechanisms behind many phenomena and processes. In addition, electronic and ionic conductivities are two important performance parameters for electrode materials, and in this section, the theoretical analysis of defects in TiO_2 and LTO will be discussed with respect to these two parameters. Furthermore, electrical conductivity can be directly inferred from electronic structure in theoretical analysis, and therefore, the DOS and band structures for both pristine and defective TiO_2 and LTO will also be discussed in which by comparing the electronic structures of pristine and defective phases, the effects of defects on the electrical conductivity of TiO_2 and LTO can be understood. Moreover, because ionic conductivity is determined by intercalation energy and the activation energy barrier of diffusion pathways, intercalation and diffusion processes and the effects of defects on these processes will also be discussed in which detailed theoretical analyses concerning these processes usually involve different intercalation sites and diffusion pathways.

5.1 DOS and Band Gap

TiO_2 has been widely applied as an anode material for LIBs and other electrochemical devices due to its excellent ability for Li, Na and Mg ion storage. As a result, TiO_2 has been extensively investigated both experimentally and theoretically in which among four naturally existing TiO_2 polymorphs (anatase, rutile, TiO_2(B) and brookite [191]), anatase, rutile and TiO_2-B (bronze) have been reported to be promising candidates as electrode materials in Li-based rechargeable batteries [192–195]. In terms of electronic structure, researchers usually focus on the DOS and band structure, especially for theoretical analysis. While the DOS and the band gap of pristine TiO_2 have been calculated many times by using DFT, the results vary depending on the choice of exchange–correlation functionals. And although DFT is a powerful method to deal with quantum multi-body issues and allows for realistic ab initio calculations, improper descriptions of exchange–correlation functionals usually result in well-known underestimations of the band gap. To correct the band gap prediction of standard DFT [including local density approximation (LDA) and generalized gradient approximation (GGA) calculations], two post-DFT methods can be used, including DFT + U, which includes the Hubbard U parameter (adding an on-site Hubbard U electron repulsion on selected localized orbitals), and hybrid density functionals, which contain a fraction of Hartree–Fock-type exchange functionals.

As an example, Dawson et al. [196] used GGA and screened exchange (sX) functionals to calculate the projected density of states (PDOS) of three pristine titania polymorphs (Fig. 28a, b) and found that the valence bands (VBs) of these polymorphs were all mainly composed of O-2p orbitals and that the CBs were mostly made up of Ti-3d orbitals in which the PDOS showed only one spin side because of its symmetric structure. These researchers also reported that for pristine TiO_2, the electrons were all found to be in pairs and consequently lacked spin polarization. These researchers also reported that the main difference between the PDOS calculated by GGA and that calculated by sX functionals is merely the distance between the VB and the CB, which is the band gap. Exact values of band gaps and lattice parameters are listed in Table 5 in which the values of GGA and sX correspond to those obtained from calculations (Fig. 28b) along with LDA, GGA + U and experimental (Exp.) values from other cited literature sources. Based on this, it is clear that LDA and GGA can severely underestimate the value of band gaps in comparison with experimental results, whereas GGA + U and sX functional results are much better.

Lithium titanate ($Li_4Ti_5O_{12}$, LTO) is another promising anode material for LIBs due to its well-known “zero strain” characteristic during charge/discharge [33, 198]. However, fewer theoretical studies of LTO exist as compared with TiO_2 due to the relatively complex structure of LTO which possesses a defective spinel structure with Li and Ti atoms randomly distributed among octahedral 16d sites. And based on the unit cell of LTO that can be denoted as $\left(Li_8\right)^{8a}\left(Li_{8/3}Ti_{40/3}\right)^{16d}\left(O_{32}\right)^{32e}$ (Fig. 28c), it can be seen that octahedral 32e sites and tetrahedral 8a sites are completely occupied by O and Li atoms, respectively, and that the ratio of Li/Ti in the 16d sites is 1/5 [197]. Here, to achieve correct stoichiometry, at least three unit cells are required to construct the atomic model for calculations, which results in a large supercell $Li_{32}Ti_{40}O_{96}$ containing 168 atoms. Furthermore, considering the numerous possible atomic arrangements of Ti and Li atoms in 16d sites because of their random distribution, it is necessary to find effective methods to determine the most likely specific structure with an exact Li/Ti distribution at the 16d sites, which is challenging, especially in such large supercells. To address this, Tsai et al. [197] systematically investigated the arrangements of Li and Ti atoms in 16d sites and proposed a proper method to effectively determine the atomic structure of LTO with the stablest Li/Ti distribution over the 16d sites by considering an appropriate distance between Li_{16d}–Li_{16d} pairs. And in the resulting calculated PDOS of the stablest structure

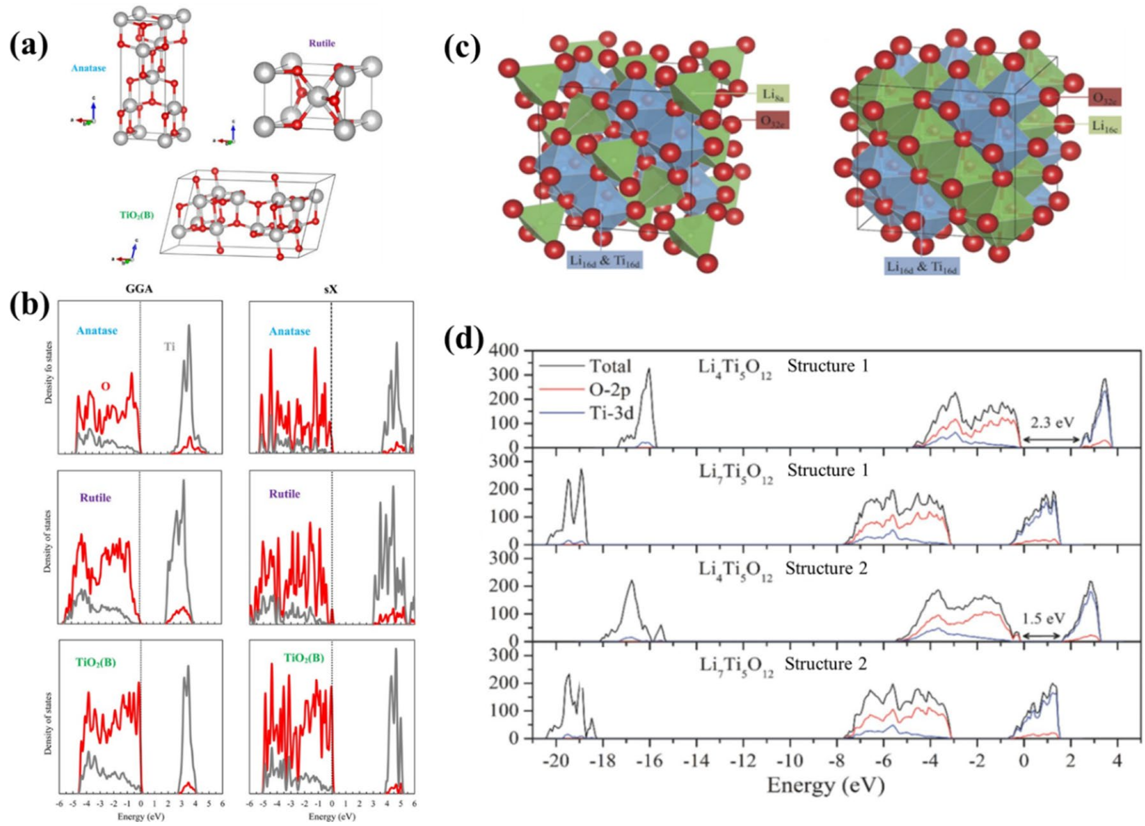

Fig. 28 **a** Crystal structure of TiO_2. Red and silver spheres represent O and Ti atoms, respectively. **b** PDOS of pristine anatase, rutile and TiO_2(B) calculated by using GGA and screened exchange (sX) functionals (the vertical dotted line represents the top of the valence band and is set to zero). Reprinted with permission from Ref. [196], copyright (2016) American Chemical Society. **c** Lattice structures of $Li_4Ti_5O_{12}$ and Li_7 Ti_5 O_{12} with unit cells. **d** PDOS of Li_4 Ti_5 O_{12} and Li_7 Ti_5 O_{12} with two different structures from PBE results in which the Fermi level is aligned to 0 eV. Reprinted with permissions from Ref. [197] under Creative Commons

(Fig. 28d), these researchers reported that similar to TiO_2, the VB and the CB of LTO are mainly composed of O-2p and Ti-3d states in which the band gap obtained from the PBE calculation was 2.3 eV, which was smaller than the experimentally reported result (3.8 eV [199–201]) and was not surprising for a result generated from PBE functionals (the GGA type) without Hubbard *U* correction. In general, however, not only do differences exist between theoretical and experimental results for estimations of LTO band gaps, large differences also exist between different theoretical results and even different experimental results (Table 5). One possible reason for this may be the different arrangements of Li/Ti in 16d sites, which is true for different calculated values ($Li_4Ti_5O_{12}$ structure 1 vs. $Li_4Ti_5O_{12}$ structure 2, Fig. 28d).

5.2 Theoretical Calculation of Defective Electronic Structures

Although TiO_2 and LTO have been experimentally confirmed to be promising anode materials with excellent Li storage properties [195, 214, 215], they still possess drawbacks such as poor electrical conductivity and deficient diffusivity of Li-ions in lattices [155, 216–220]. Here, several strategies have been adopted to improve the electrochemical performance of TiO_2 and LTO in which the introduction of defects including intrinsic defects such as OVs [113, 155, 221–224] and non-intrinsic defects such as doping [155, 220, 225–227] has shown experimental promise. As a result, theoretical analysis calculating defective electronic structures is important to understand such results.

5.2.1 Oxygen Vacancies

The introduction of OVs into TiO_2 can enhance the electrical conductivity of corresponding electrodes and improve the rate performance, cycling stability and energy capacity of batteries [113, 219, 221, 223]. To further understand the mechanisms behind this effect, significant theoretical studies have been conducted [203, 228–230]. Here, to calculate the properties of TiO_2 with OVs, the exact location of nonequivalent OV sites inside lattices needs to be first identified.

Table 5 Calculated lattice parameters and band gaps for three TiO_2 polymorphs, $Li_4Ti_5O_{12}$ and $Li_7Ti_5O_{12}$, together with experimental results for comparison

Structure	Method	Band gap	Lattice parameters			References
		E_g (eV)	a (Å)	b (Å)	c (Å)	
Anatase	LDA	2.00	3.69	–	9.47	[202]
	GGA	2.04	3.80	–	9.68	[196]
	GGA + U^a	3.18	3.79	–	9.77	[203]
	sX	3.51	3.75	–	9.59	[196]
	Exp.	3.20	–	–	–	[204]
	Exp.	–	3.79	–	9.51	[205]
Rutile	LDA	2.02	4.53	–	2.91	[206]
	GGA	1.77	4.63	–	2.96	[196]
	GGA + U^a	2.52	4.64	–	2.97	[203]
	sX	2.94	4.56	–	2.96	[196]
	Exp.	3.03	–	–	–	[204]
	Exp.	–	4.59	–	2.96	[205]
TiO_2(B)	LDA	–	12.14	3.73	6.49	[207]
	GGA	2.57	12.26	3.75	6.6	[196]
	GGA + U^a	3.28	12.28	3.76	6.62	[203]
	sX	3.71	12.15	3.72	6.48	[196]
	Exp.	3.22	–	–	–	[208]
	Exp.	–	12.18	3.74	6.53	[209]
$Li_4Ti_5O_{12}$	GGA(PBE)	2.3	8.4257	–	–	[131, 197]
	GGA(PW91)	2	8.619	–	–	[210]
	Exp.	3.8 3.1 1.8	–	–	–	[199–201] [211] [212]
	Exp.	–	8.3595	–	–	[213]
$Li_7Ti_5O_{12}$	GGA(PBE)	0^b	8.3609	–	–	[197]
	Exp.	–	8.3538	–	–	[213]

[a] The value of U used in this GGA + U calculation is 9.0 eV [203]

[b] $Li_7Ti_5O_{12}$ is a conductor with no band gaps [197, 210]

For anatase and rutile phases, there is only one type of OV sites [203] due to their relatively simple crystal structures in which the crystal structures of anatase (the space group $I4_1/amd$) and rutile (the space group $P4_2/mnm$) are both tetragonal (Fig. 28a). As for the TiO_2(B) (the space group $C2/m$) polymorph however, a monoclinic crystal structure exists (Fig. 29a) that is more complex in which Dalton et al. [231] showed that depending on different coordination numbers, two types of Ti atoms and three types of O atoms exist in TiO_2(B) and Arrouvel et al. [232] denoted these atoms as Ti_1, Ti_2 and O_{br} (bridging oxygen), O_{3f} (threefold coordinated oxygen) and O_{4f} (fourfold coordinated oxygen) (Fig. 29a). Alternatively, Feist et al. [209] reported that based on the experimentally observed bulk crystal structure, four different O sites exist inside one unit of the TiO_2(B) lattice, including O atoms with nearly linear twofold coordination inside the ab-plane (001), O atoms with tetrahedral fourfold coordination, O atoms with planar threefold coordination parallel to the ac-plane (010) and O atoms with planar threefold coordination parallel to the ab-plane (001). Based on this, Kong et al. [229] suggested that the label O_{3f} actually included two types of O atoms, which they labeled as $O_{3f(1)}$ and $O_{3f(2)}$ (Fig. 29b, c).

Finazzi et al. [228] also investigated OVs in bulk anatase using DFT calculations with GGA, GGA + U and hybrid functional methods performed on the CRYSTAL06 code in which the system with OVs used was a so-called triplet state, which possessed two extra electrons with each OV. Here, by using the equation $E_f = E(TiO_{2-x}) - E(TiO_2) + E\left(\frac{x}{2}O_2\right)$, these researchers calculated defect formation energies (E_f) for one OV in a supercell of 96 atoms ($Ti_{32}O_{64}$) with a OV concentration of 1.56% and obtained results that were in the range of 4.2–4.8 eV, varying based on the exchange–correlation functional used. In another study, Kong et al. [229] also calculated the OV formation energy of four types of O atoms in TiO_2(B) using VASP at the level of GGA + U (U = 4.0 eV) and obtained results that were in the range of 5.67–6.2 eV with an OV concentration of 1.56%. These researchers also reported that the OV formation energy values follow the

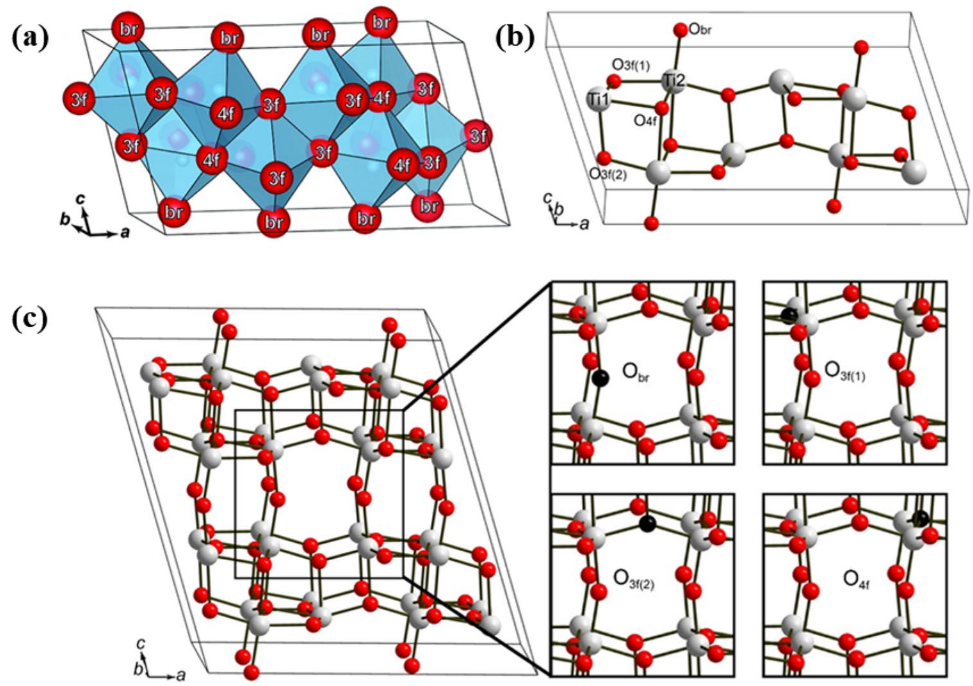

Fig. 29 **a** Oxygen sites inside one unit of bulk crystal TiO_2(B) structure with the version of **a** br, 3f and 4f. Reprinted with permission from Ref. [231], copyright (2012) American Chemical Society. And **b** & **c** br, 3f(1), 3f(2) and 4f. Reprinted with permission from Ref. [229], copyright (2016) Elsevier

order: $O_{3f(1)} < O_{4f} < O_{3f(2)} < O_{br}$, suggesting that $O_{3f(1)}$ site O atoms were the easiest to remove from lattices. Furthermore, Zhang et al. [230] calculated the properties of OVs in TiO_2(B) using the CASTEP code based on GGA and obtained OV formation energy values in the order of $O_{3f} < O_{br} < O_{4f}$ (only three types of oxygen sites were considered in this study in which the O_{3f} site actually included $O_{3f(1)}$ and $O_{3f(2)}$ sites). And although the order of O_{br} and O_{4f} was different in each study, the conclusion that OVs at the O_{3f} site are the most energetically favorable is consistent. More recently, Yeh et al. [203] also calculated OV formation energy for anatase, rutile and TiO_2(B) and took into account all four non-equivalent O sites for TiO_2(B) using the CASTEP code with GGA + U (U = 9.0 eV). Here, the obtained results in this study for TiO_2 polymorphs were in the order of anatase (4.46 eV, 0.69% OV) < rutile (4.60 eV, 0.69% OV) < TiO_2(B) (in the range of 5.34–5.98 eV, 0.78% OV) and the results for the four non-equivalent O sites of TiO_2(B) were in the order: $O_{br} < O_{3f(1)} < O_{4f} < O_{3f(2)}$. However, although the order of $O_{3f(1)} < O_{4f} < O_{3f(2)}$ in this study was consistent with those reported by Kong et al. [229], these researchers concluded that O_{br} sites possessed the lowest OV formation energy, which conflicted with the two previously described studies [229, 230] that suggested O_{br}, O_{3f} or $O_{3f(1)}$ sites possessed the lowest OV formation energy. Overall among the three polymorphs, OV formation energy data suggest that anatase can more easily form OVs than rutile or TiO_2(B).

Defect states introduced by OVs have profound influences on electronic structure, which can be clearly observed from the calculated PDOS of anatase (Fig. 30) by Finazzi et al. [228]. And in contrast to pristine states (Fig. 28b), the existence of one OV can result in unpaired electrons and lead to asymmetry in the PDOS (Fig. 30), which possesses two sides, including a spin-up side and a spin-down side. These researchers also reported that the theoretical description of the electronic structure of one OV in bulk anatase TiO_2 is highly dependent on the computational method in which conventional DFT functionals such as PBE (the GGA type) present a completely delocalized electron (Fig. 30b) and no states in the gap (Fig. 30a, defect states are adjacent to the CB). In addition, the results of GGA + U calculations are strongly dependent on the value of U in which if U increases from 2 to 4 eV, electrons become more localized (Fig. 30d, f, h) and defect states move deeper inside the gap (Fig. 30c, e, g). And although hybrid functionals can fix the delocalization problem (Fig. 30j, l), the rationality of results depends on the proper percentage of Hartree–Fock exchange in which the H&HLYP (hybrid DFT with 50% HF exchange, H&H = half&half) yields a gap that is too large [6.82 eV [228] vs. 3.20 eV (an experimental value, Table 5)], leading to results without physical meaning. Furthermore, B3LYP (hybrid DFT with 20% HF exchange) can also overestimate the band gap (3.92 eV [228] vs. 3.20 eV) and a 13% [233] admixture of HF exchange is suggested to obtain a correct gap for TiO_2.

The PDOS of OV-defective TiO_2 for all three polymorphs with different OV sites suggests that the existence of OVs can not only introduce defect states in band gaps, but also reduce gaps in which the position of gap states and the

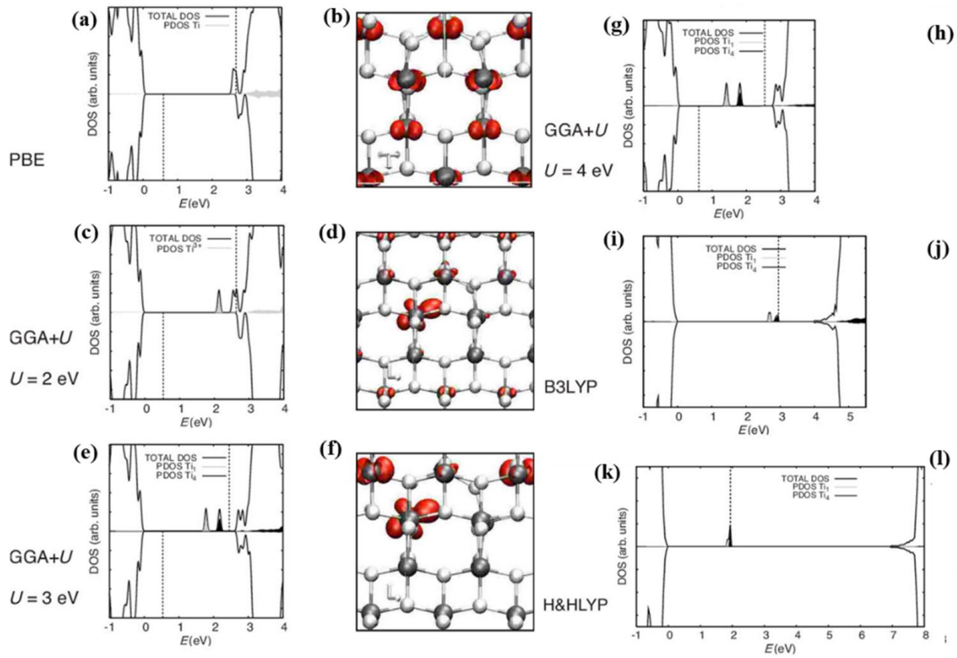

Fig. 30 Calculated PDOS for anatase with OVs (the left column, **a**–**e**) and corresponding spin distribution (**b**–**f**, Ti atoms: black spheres, O atoms: white spheres). **a, b** PBE (the GGA type), **c, d** GGA + U (U = 2 eV), **e**, **f** GGA + U (U = 3 eV), **g**, **h** GGA + U (U = 4 eV), **i**, **j** B3LYP (hybrid DFT with 20% HF exchange) and **k**, **l** H&HLYP (hybrid DFT with 50% HF exchange, H&H = half&half). Reprinted with permission from Ref. [228], copyright (2008) AIP Publishing

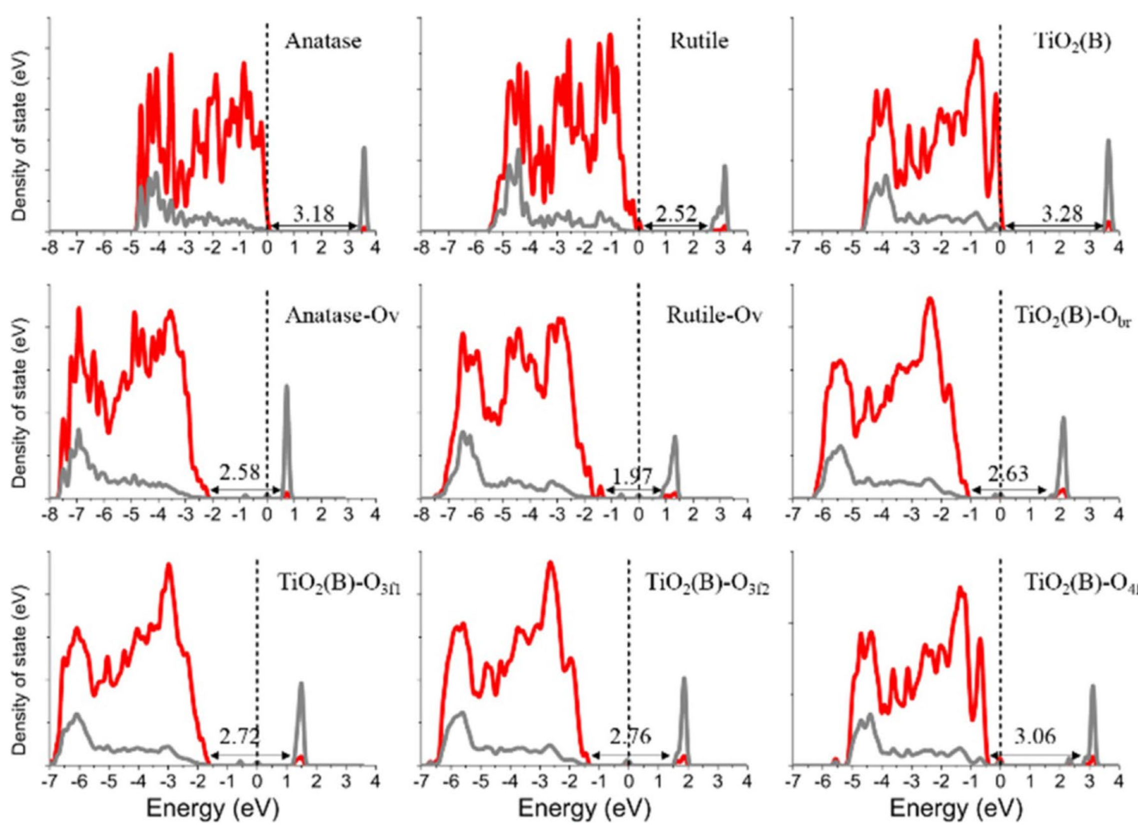

Fig. 31 PDOS of anatase, rutile, TiO_2 (B) and their OV-defective models. Red curves represent O-2p states, and gray curves represent Ti-3d states. Reprinted with permission from Ref. [203], copyright (2018) American Chemical Society

reduction of gaps vary from different OV sites (Fig. 31). Here, several theoretical calculations [203, 224, 229, 230] have demonstrated that the reason for enhanced electrochemical performance through the introduction of OVs in TiO_2 is the improvement of electrical conductivity by decreased band gaps and increased charge carrier concentrations. For example, Yeh et al. [203] in their calculations reported that after the introduction of OVs, band gaps were reduced by 0.66, 0.55 and 0.22–0.65 eV [depending on the different OV sites in TiO_2(B)] for oxygen-defective anatase, rutile and TiO_2(B), respectively, and that for each polymorph, the Fermi level shifted toward the CB. Similarly, Finazzi et al. [228] reported that for anatase, the localized electrons calculated by GGA + U (U = 3 eV) and B3LYP gave rise to states within the gap at the position near ~ 1 eV below the CB (Fig. 30e, i), resulting in a decrease in the band gap. Furthermore, Zheng et al. [224] reported that as compared with the DOS of anatase with 1.56% oxygen deficiency, more DOS can be found below the Fermi level in 3.13% oxygen defective anatase, suggesting a higher charge carrier concentration with increased OVs.

As for LTO, researchers have experimentally [131, 155, 234] and theoretically [131, 235] reported that the existence of OVs can improve electrical conductivity. And to calculate OV-defective LTO, different oxygen sites do not need to be considered because there is only one type of oxygen atoms that resides in the octahedral 32e sites of the spinel structure. For example, Nasara et al. [131] performed ab initio calculations on OV-defective LTO through VASP using a GGA functional parameterized by PBE in which the atomic models used were the cubic supercell $Li_{32}Ti_{40}O_{96}$ ($Li_4Ti_5O_{12}$) for the pristine phase and $Li_{32}Ti_{40}O_{95}$ ($Li_4Ti_5O_{11.875}$) for the OV-defective one, with an OV concentration of 1.04% (1/96 atoms) (Fig. 32a). In this study, the model used for the pristine LTO was the same as the stablest one reported by Tsai et al. [197]; therefore, the calculated PDOS and band gaps were also similar (Fig. 32b, 28d, 2.3 eV) under the same PBE functional. Nasara et al. also reported that the LTO lattice parameter can expand by 0.1519% (from 8.426 Å for the pristine material to 8.439 Å for the OV-defective one) in the presence of OVs and that the different charge distributions (Fig. 32c) revealed that the negative charge compensation as induced by OVs is localized around nearby Ti ions. Furthermore, these researchers also obtained the PDOS of OV-defective LTO (Fig. 32d) and reported that the Fermi level can shift to the CB due to the filling of charge compensated electrons in the CB in which the number of these electrons is two, corresponding to the model of one OV in a supercell. And based on this, OVs can increase charge carrier density and even allow LTO to behave like a metal, thus enhancing the electrical conductivity of OV-defective LTO. Samin et al. [235] also

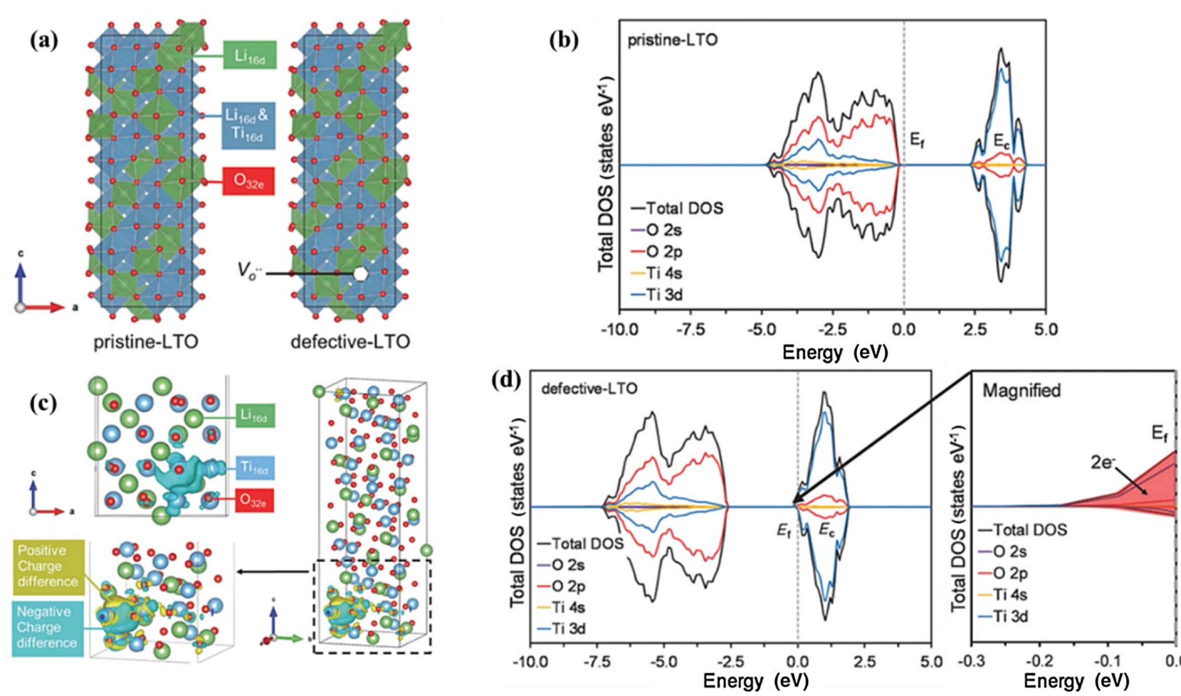

Fig. 32 **a** Supercell models for pristine and OV-defective LTO. **b** PDOS of pristine LTO. **c** Charge density difference schematic for OV-defective LTO. **d** PDOS of OV-defective LTO (the inset magnifies the partially occupied CBM). Reprinted with permission from Ref. [131], copyright (2017) John Wiley and Sons

reported similar results for the insulator-to-metal transition of OV-defective LTO based on DFT calculations with the same atomic model and the same PBE functional in which their calculated formation energy for 1.04% OV was 7.45 eV.

Overall, OVs are essential defects in metal oxides due to their comprehensive influence. And according to theoretical analysis, OVs can act as shallow donors and increase the DOS to below the Fermi level and thus increase charge carrier concentration. In addition, OVs can introduce defective states into band gaps and reduce band gaps. Furthermore, the effects of OVs are not only limited to electrical conductivity and they can also have a significant impact on the intercalation and diffusion of Li-ions, which will be discussed in the following sections.

5.2.2 Li Doping

As electrode materials for rechargeable LIBs, the properties of Li-intercalated TiO_2 (Li-doped TiO_2) also need to be studied because the intercalation of Li atoms can also affect the electronic structure of host materials. For example, Dawson et al. [196] calculated the PDOS of Li-doped TiO_2 by using the hybrid sX functional and found that gap states formed in the PDOS for all three polymorphs and that their positions were all at ~ 1 eV below the CB (Fig. 33a). Furthermore, these researchers also reported that these defect states all occupied the Ti-3d state, suggesting that excess charge from doped Li is localized at nearby Ti atoms, producing Ti^{3+} ions. Other calculations by using GGA + U [207, 236] and HSE [237] have also reported similar results, all of which are in agreement with experimental findings for anatase [238–241] and rutile [242]. Moreover, defect states generally do not appear within the band gap of Li-doped TiO_2 in GGA calculations [207, 236, 243] because excess charge is delocalized in GGA calculations, and GGA + U or hybrid functionals are necessary to correct the delocalization problem. However, Legrain et al. [244] reported that their calculations using GGA produced localized results with defect states appearing within the band gap and below the CB at ~ 1 eV for anatase and rutile and at 1.5 eV for TiO_2(B). These researchers also conducted a spin density difference analysis which showed that the occupied Ti-3d state was localized on single Ti atoms for all polymorphs, indicating the presence of Ti-3d species (Fig. 33b). Here, these researchers attributed this to the use of tuned, localized basis sets and norm-conserving pseudopotentials. Nevertheless, their findings will require further investigations to verify.

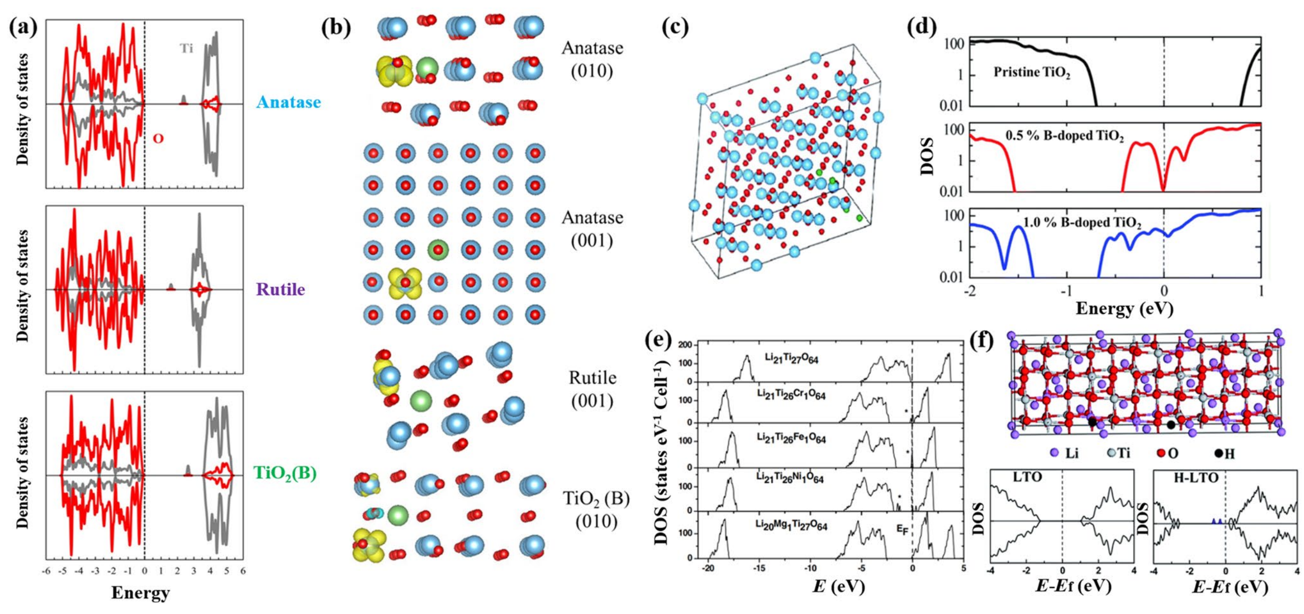

Fig. 33 **a** PDOS of Li-intercalated anatase, rutile and TiO_2(B) calculated by using sX functionals. The vertical dotted line represents the top of the valence band which is set to zero. Reprinted with permission from Ref. [196], copyright (2016) American Chemical Society. **b** Spin density differences $\rho_{\mathrm{plotted}} = \rho_{\mathrm{up}} - \rho_{\mathrm{down}}$ in three Li-doped TiO_2 polymorphs (Ti atoms: blue spheres, O atoms: red spheres, Li atoms: green spheres). The projection plane is (001) and (010) for anatase, (001) for rutile and (010) for TiO_2(B). Reprinted with permission from Ref. [244], copyright (2015) Elsevier. **c** Supercell model of boron-doped rutile TiO_2. **d** Calculated DOS of pristine and boron-doped rutile TiO_2 with dopant concentrations of 0.5% and 1.0%. Reprinted with permission from Ref. [226], copyright (2014) Royal Society of Chemistry. **e** DOS of LTO and M-doped LTO (M = Cr, Fe, Ni and Mg) calculated with a 2 × 1 × 1 supercell and GGA functional. Reprinted with permission from Ref. [245], copyright (2006) John Wiley and Sons. **f** 3 × 1 × 1 supercell model for H-doped LTO and the calculated DOS for pristine and H-doped models from HSE06. Reprinted with permission from Ref. [110], copyright (2014) Royal Society of Chemistry

Similarities also exist between the electronic structures of Li-doped TiO_2 and OV-defective TiO_2 in which both contain defect states forming in the gap ~ 1 eV below the CB by affecting the Ti-3d states. For example, the PDOS of Li-doped anatase (Fig. 33a, top panel) is similar to the PDOS of OV-defective anatase (Fig. 30e) and the only difference is the shape of the defect states in which the former consists of one peak and the latter consists of two peaks. Here, the reasons for the similarities and differences in the electronic structures between these two defective systems are easy to understand and are based on the fact that one intercalating Li atom can bring one extra electron, whereas one OV can result in two extra electrons. And considering the similarity of electronic structures, the effects of these two types of defects are similar as well in which similar to OV-formation, Li doping can also reduce band gaps and increase charge carrier concentrations to improve electrical conductivity [236]. Furthermore, previously intercalated Li in TiO_2 can also affect the successive intercalation and transport of other Li-ions (discussed in Sect. 5.3).

The situation for Li-doped LTO is different from TiO_2, however, because the intercalation of Li does not alter the phase structure of the TiO host, but will lead to phase transformations in LTO [33, 197, 210, 213, 246]. Overall, it is generally accepted that $Li_7Ti_5O_{12}$, a defective rock-salt structure (Fig. 28c), is the stablest phase for Li-doped LTO in which the unit cell of $Li_7Ti_5O_{12}$ can be denoted as $\left(Li_{16}\right)^{16c}\left(Li_{8/3}Ti_{40/3}\right)^{16d}\left(O_{32}\right)^{32e}$ with octahedral 16c sites, 32e sites and 16*d* sites occupied by Li atoms, O atoms and a random distribution of 1/3 Li and 5/3 Ti, respectively. Similarly, a supercell $Li_{56}Ti_{40}O_{96}$ containing 192 atoms is composed of three unit cells to achieve correct stoichiometry. Here, Tsai et al. [197] calculated the PDOS of $Li_7Ti_5O_{12}$ with an optimized specific atomic structure (Fig. 28d) and reported that as compared with pristine LTO, the Fermi level shifted up into the conduction bands due to extra electrons from the ionization of intercalated Li atoms, making $Li_7Ti_5O_{12}$ a conductor. The metallic properties of $Li_7Ti_5O_{12}$ have also been reported in experimental studies [213].

5.2.3 Doping with Other Cations or Anions

To improve the electrochemical performance of TiO_2 as an anode in LIBs, the strategy of introducing non-intrinsic defects such as doping with cations or anions has also been adopted in which the effects of several different dopants for TiO_2 LIB anodes have been extensively investigated. These dopants include Fe^{3+} [247, 248], Mn [103, 104], Co [101], Ni [249], Cu [99], Zn [100], Nb [250], Mo^{6+} [251], Sn [252, 253], F^- [254], B [226], C [255], N [225, 256–259], P [227] and co-doping systems such as C–N [260, 261] and Cr–N [262]. Despite the extensiveness of these dopants, aliovalent ion-doped TiO_2 electrodes have rarely been examined from a theoretical first-principle calculation perspective. However, computational studies of doped TiO_2 for photocatalysis or other applications are available and the doping effects of the same aliovalent elements in TiO_2 are constant regardless of application. Furthermore, although significant theoretical studies [226, 263–272] have demonstrated that doping with different elements can enhance electrical conductivity, the electronic structure of doped TiO_2 with different dopants differs significantly. And for the sake of conciseness, boron-doped TiO_2 will be used as an example in this review to discuss the electronic structure of doped systems and doping effects.

For example, Tian et al. [226] investigated rutile with B atoms substituting O atoms using GGA DFT calculations without the Hubbard *U* parameter and their calculated DOS for pristine and doped rutile with 0.5% and 1% dopants showed that B-doping can lead to Fermi levels moving toward the CB, indicating that the main carriers in this doped system are electrons (Fig. 33d). In addition, these researchers found that the defect states caused by B-doping started to appear in the gap but were adjacent to the CB. And to study the influence of B-doping on electrical conductivity (σ), these researchers also calculated the band structure and obtained the effective mass m^* of the CB minimum through $m^* = \hbar^2/\left(\partial^2 E(k)/\partial k^2\right)$ in which $\hbar$ is the reduced Planck constant. Here, based on the basic physical equation $\sigma = ne\mu$ (n, e, μ denotes carrier concentration, elementary charge and carrier mobility, respectively), the relationship between electrical conductivity, carrier concentration, defect concentration N and effective mass can be expressed as $\sigma \propto n/Nm^*$, in which μ is inversely proportional to N and m^* ($\mu \propto 1/Nm^*$) and the carrier concentration n can be calculated by integrating the DOS. Furthermore, because the defect concentration N is known, the value of electrical conductivity can also be obtained. And as a result, the calculated results obtained in this study revealed that B-doping at lower concentrations ($< 1\%$) can enhance carrier mobility μ and electrical conductivity σ by increasing carrier concentration n and decreasing effective mass m^* of the CB minimum. Similar results were also reported by Yang et al. [272] for Nb-doping and according to results from other studies [264–271], improved electrical conductivity caused by doping with various elements is a result of the reduction of band gaps. Overall, enhanced electrical conductivity is a positive effect of doping and is one of the reasons for improved electrochemical performance as seen in various experimental studies employing doping [99–101, 103, 104, 225–227, 247–259].

Similarly, significant experimental efforts have been undertaken to evaluate doping effects for LTO with various aliovalent ions such as V [273], Cr [220, 274], Mn [274], Co [274], Ni [274], Zr [275, 276], Nb [277], Mo [155, 278], Ru [279], Gd [280], Na [281, 282], Mg [283], Ca [284], Sr [285], Br [286], H [110] and co-doping systems such as Mi–Mn [287], W–Br [288], Al–F [289] and Na–K [290], all of which have reported enhanced performances for LIBs. Despite this, there are few theoretical studies on aliovalent ion-doping for LTO in which theoretical studies on LTO doping with other cations or anions are limited to doping with Cr, Fe, Ni or Mg [245], Zr [276], H [110], Na [281], Zn [291], Br, Cl, F, N, P or S [292], W and Br [288], Gd [280] and Mg [293]. In this review, typical cases will be presented to illustrate defective electronic structures and doping effects associated with LTO. For example, Liu et al. [245] investigated the electronic properties of M-doped LTO (M = Cr, Fe, Ni and Mg) using DFT GGA calculations in which they considered a model with one Ti substituted by Cr, Fe or Ni and another model with one Li substituted by Mg in a $2 \times 1 \times 1$ supercell. Here, the calculated DOS showed that the new states consisting of 3d orbitals of dopants appeared in the gap for Cr-, Fe- and Ni-doped LTO (Fig. 33e) in which the Fe 3d states and Ni 3d states were localized and were far from the CB, making it difficult for electrons to hop to the CB. However, the Cr 3d states were also near the Ti 3d states (the main component of the CB), allowing the hopping of electrons between these 3d states to be feasible. As for Mg doping, these researchers reported that the Fermi level shifted toward the CBM due to the extra valence electron (Mg substituting Li), making the system an n-type semiconductor. As a result, these researchers reported that Cr- and Mg-doping can enhance the electrical conductivity of LTO by increasing the density of carriers, whereas Fe- and Ni-doping did not. The improved electrical conductivity of Mg-doping has also been reported by Cho et al. [293], who investigated Mg doping sites in LTO using first-principle calculations. Qiu et al. [110] also studied the electronic properties of H-doped LTO using DFT calculations based on HSE06, a hybrid functional. Here, the computational model (a $3 \times 1 \times 1$ supercell with two H atoms randomly distributed among interstitial sites) and the corresponding calculated DOS clearly revealed that H-doping can introduce mid-gap states that were below the Fermi level and thus were occupied with electrons that were easier to transport to the CB (Fig. 33f), meaning that the reduction of the band gap was the reason for enhancements in the electrical conductivity of H-doped LTO. Obvious changes in electronic structure and improved electrical conductivity for LTO have also been reported in doping with other elements such as Gd [280], Zn [291] and W–Br co-doping [288]. However, Kim et al. [276] also reported that in the case of Zr-doped LTO, little effects on electronic structure and electrical conductivity were found after Zr substituted Ti according to calculated results.

5.3 Li-Intercalation and Diffusion Processes and the Effects of Defects

In the study of TiO_2 anodes for LIBs, the processes of intercalation and diffusion of Li-ions are critically important, especially the theoretical aspects. In general, there are several different possible sites for intercalation and pathways for diffusion within the same structure, and in order to find the most probable ones, the usual technique is to calculate and analyze the intercalation energy for each site and the diffusion activation energy barrier for each pathway. Similarly, investigations into the influence of defects on these processes can also be achieved by calculating and comparing these two terms for pristine and defective structures.

5.3.1 Li-Intercalation and Diffusion Processes in Pristine Structures

5.3.1.1 Li-Intercalation The primary problem faced by the construction of a theoretical model for calculations is the defining of the precise location of Li-ions. In anatase and rutile structures, both the empty octahedral and tetrahedral sites are potential sites for Li-ions to intercalate [196, 243, 294], whereas for the TiO_2(B) structure, three possible intercalation sites exist [229, 232, 295] and can be referred to as C, A1 and A2 (Fig. 34a). Here, the C site is located in the middle of a distorted octahedron as the cavity of the *b*-axis channel and is also at the center of the square plane created by the arrangement of O_{br} atoms. Alternatively, the A1 site is fivefold coordinated to $O_{3f(2)}$ atoms in the (001) plane and the A2 site is also fivefold coordinated to O_{br} atoms within the (001) plane. Here, various experimental [296, 297] and theoretical [196, 232, 236, 243] studies have reported that intercalated Li atoms do not sit perfectly at the center of C sites in TiO_2(B) [196, 232, 296] or at the center of the O_6 octahedron in anatase [196, 236, 297] and rutile [196, 243] and according to the theoretical calculations by Dawson et al. [196], the off-center displacement of an intercalated Li atom is ~ 0.3 Å along the *b*-axis in TiO_2(B) and ~ 0.3 Å and 0.5 Å along the *c*-axis in anatase and rutile, respectively.

The stability of Li-intercalated systems can also be analyzed by evaluating the defect formation energy of Li-doped TiO_2 or the intercalation energy of Li in TiO_2, in which $E_{intercalation} = E_{lithiated} - E_{TiO_2} - E_{Li}$. Here, octahedral sites appear to be stabler for anatase and rutile [196, 244] because Li atoms positioned at the tetrahedral sites either provide higher energy or drift to octahedral sites [244]. For example, calculations conducted by Dawson et al. [196] showed that octahedral sites were more energetically favorable than tetrahedral sites by − 0.39 and − 0.61 eV in anatase [Li_xTiO_2, x(Li) = 0.028] and rutile [Li_xTiO_2, x(Li) = 0.031], respectively. Koudriachova et al. [294] reported similar results of − 0.45 and − 0.7 eV for anatase [x(Li/Ti) = 0.5] and rutile

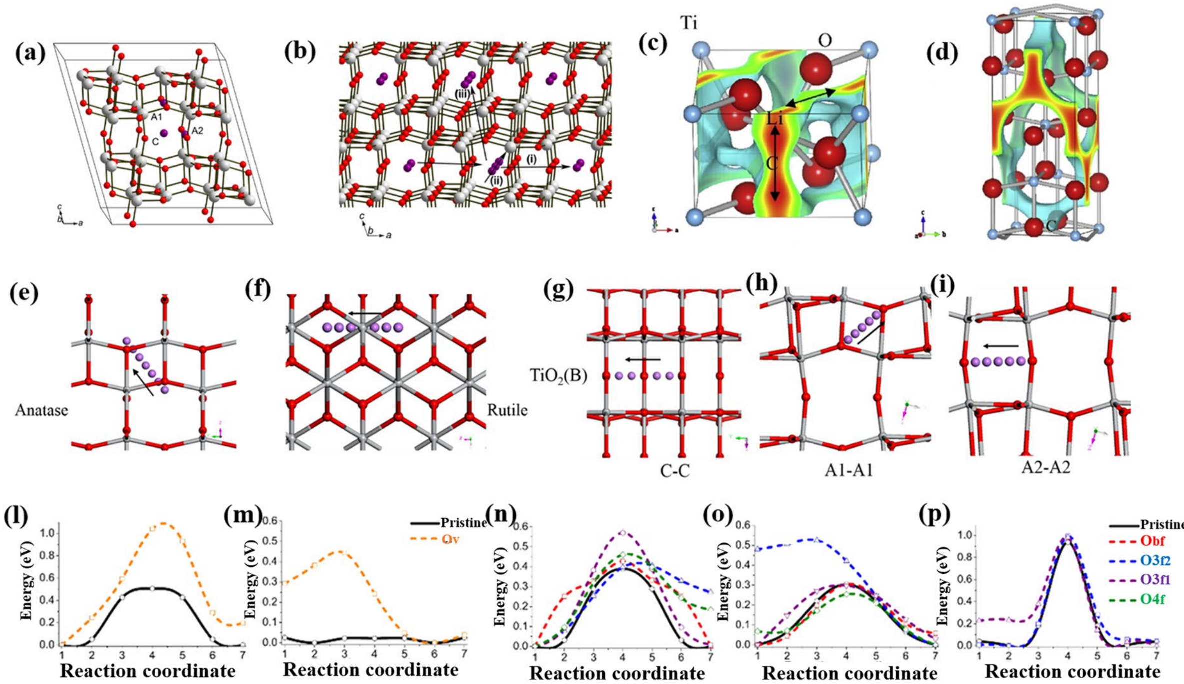

Fig. 34 **a** Three insertion sites in the structure of TiO_2(B). **b** Three possible diffusion pathways for Li-ions involving conventional hopping between two neighboring C sites in TiO_2(B). In **a** and **b**, white, red and purple spheres represent Ti, O and Li atoms, respectively. Reprinted with permission from Ref. [229], copyright (2016) Elsevier. **c** Diffusion pathway between two octahedral sites in rutile. **d** Diffusion pathway between two octahedral sites in anatase. In **c** and **d**, light blue and red spheres represent Ti and O atoms, respectively. Reprinted with permission from Ref. [298], copyright (2015) Elsevier. Li diffusion pathways for **e** anatase and **f** rutile involving Li-ions hopping between two neighboring octahedral sites in each structure. Li diffusion pathways for TiO_2(B) with Li atoms hopping between **g** two adjacent C sites, **h** two neighboring A1 sites and **i** two neighboring A2 sites. **l**–**p** Calculated energy profiles for Li-ion diffusion pathways in pristine and OV-defective models of **l** anatase, **m** rutile and for TiO_2(B), **n** C–C, **o** A1–A1 and **p** A2–A2. Reprinted with permission from Ref. [203], copyright (2018) American Chemical Society

[x(Li/Ti) = 0.5], respectively. As for TiO_2(B), disagreement exists concerning which of the potential three intercalation sites is the stablest in which many computational studies [196, 203, 229, 232] indicate that C sites are the lowest energy sites for Li-intercalation as confirmed with powder neutron diffraction experiments [296], whereas other calculations predict that A2 [207, 299] or A1 sites [231] are more energetically preferable.

And in the comparison of Li-intercalation energies among the three TiO_2 polymorphs, Yeh et al. [203] found the order of stability to be TiO_2(B) [C site, − 1.4079 eV, x(Li/Ti) = 0.016] > anatase [octahedral site, − 1.3616 eV, x(Li/Ti) = 0.014] > rutile [octahedral site, − 0.1531 eV, x(Li/Ti) = 0.014]. Similar results were also reported by Legrain et al. [244]. Here, the negative values of the defect formation energy for Li-doped TiO_2 suggest that all three polymorphs can be good candidates for Li-intercalation. Despite this, Li-intercalation energy for rutile is much smaller than that for anatase and TiO_2(B), corresponding to lower theoretical capacity of rutile (168 mAh g^{-1} [300]) as compared with that of TiO_2(B) and anatase (both with capacities of 335 mAh g^{-1} [301]).

Li-ion intercalation in LTO is accompanied by phase transformation as induced by the location change of Li-ions in which in the spinel cubic unit cell $\left(Li_8\right)^{8a}\left(Li_{8/3}Ti_{40/3}\right)^{16d}\left(O_{32}\right)^{32e}$ of LTO, octahedral 16c sites are empty. Here, researchers have confirmed [197, 210, 246] that during the intercalation process, newly inserted Li-ions occupy empty octahedral 16c sites and Li-ions that originally resided in tetrahedral 8a sites transfer to octahedral 16c sites to form $\left(Li_{16}\right)^{16c}\left(Li_{8/3}Ti_{40/3}\right)^{16d}\left(O_{32}\right)^{32e}$ ($Li_7Ti_5O_{12}$) and that this newly formed rock-salt phase of $Li_7Ti_5O_{12}$ can maintain the $\left(Li_{8/3}Ti_{40/3}\right)^{16d}\left(O_{32}\right)^{32e}$ framework, possibly being the reason for the "zero strain" characteristic. Researchers have also calculated the slight shrinkage in the lattice volume to be 0.2% [210] or 0.77% [197] for $Li_{4+x}Ti_5O_{12}$ if x changes from 0 to 3 and the average Li-intercalation voltage (from $x = 0$ to $x = 3$ for $Li_{4+x}Ti_5O_{12}$) was calculated to be 1.45 V [210] or 1.41 V [197], which is close to the experimental result of 1.55 V [198]. Overall, the reversible charge/discharge process of LTO is thought to occur between $Li_4Ti_5O_{12}$ and $Li_7Ti_5O_{12}$ phases [197, 210], corresponding to a reversible theoretical capacity of 175 mAh g^{-1} [33]. However, Zhong et al. [246] reported that

LTO can continue to be intercalated by Li-ions until reaching a $Li_{8.5}Ti_5O_{12}$ state during which the $\left(Li_{8/3}Ti_{40/3}\right)^{16d}\left(O_{32}\right)^{32e}$ framework can remain stable and that further intercalation of Li-ions can bring about clear structural distortion. Here, these researchers also reported based on calculations that the average intercalation voltage for $Li_{4+x}Ti_5O_{12}$ was 1.48 V (from $x=0$ to $x=3$) and 0.05 V (from $x=3$ to $x=4.5$) and that the total theoretical capacity was 260 mAh g^{-1} (with x from 0 to 4.5).

5.3.1.2 Li-Diffusion Process Based on the possible Li-ion diffusion pathways for the three polymorphs of TiO_2 (Fig. 34b–i) along with their corresponding energy profiles (Fig. 34l–p), the most probable Li-ion diffusion pathway is along the <201> direction for anatase (Fig. 34d) and along the *c*-axis direction for rutile (Fig. 34c) with the lowest activation energy being 0.42 eV and 0.04 eV for anatase and rutile, respectively [298], in which both pathways involve Li-ion hopping between two neighboring octahedral sites. As for Li hopping among tetrahedral sites, this leads to much higher energy barriers. For example, the activation energy of a zigzag path in the (001) plane with Li passing through tetrahedral sites in rutile is 0.8 eV [x(Li/Ti) = 0.5] [243], which is much higher than the activation energy of the *c*-axis directional path [0.04 eV from the same calculation [243] with the same x(Li/Ti) = 0.5]. Therefore, the diffusion of Li-ions in rutile is one dimensional (along the *c*-axis direction) and strongly anisotropic. The same diffusion direction and similar energy barriers as these two polymorphs of TiO_2 were also reported from other calculations such as the energy barrier for anatase (Li_xTiO_2) of 0.6 eV [x(Li/Ti) = 0.03] [302], 0.511 eV [x(Li/Ti) = 0.028] [236] and 0.5056 eV [x(Li/Ti) = 0.014] and for rutile (Li_xTiO_2) of 0.04 eV [x(Li/Ti) = 0.5] [243, 294] and 0.0254 [x(Li/Ti) = 0.014] [203]. As for TiO_2(B), three possible Li-ion diffusion pathways involving conventional hopping between two neighboring C sites (Fig. 34 b) exist, including migration along the *a*-axis direction with Li-ions following a zigzag path in the (001) plane through A2 sites (path i), migration along the *b*-axis channel (the *b*-axis direction) between two adjacent C sites (path ii) and migration along the *c*-axis direction between two *b*-axis channels through A1 sites (path iii) [229, 232]. Here, Arrouvel et al. [232] calculated the activation energy barriers of these three pathways and found that they were in the order of path (ii) (~ 0.3 eV) < path (iii) (~ 0.5 eV) < path (i) (~ 1 eV) [x(Li) = 0.125] and Kong et al. [229] reported similar results with an order of path (ii) (0.51 eV) < path (iii) (0.71 eV) < path (i) (1.16 eV) [x(Li/Ti) = 0.031]. And although the values from these different calculations were not exactly the same, the same order of pathways—path (ii) < path (iii) < path (i) in both studies suggested that the *b*-axis direction along the b-axis channel is the most energetically favorable pathway for Li-ion migration in TiO_2(B). Despite this, these results only considered Li-ions hopping from one C site to another C site (the C–C path, Fig. 34g), and more recently, Yeh et al. [203] conducted a systematic investigation of the minimum energy pathways in TiO_2(B) for Li-ion hopping between two A1 sites (the A1–A1 path, Fig. 34h) and between two A2 sites (the A2–A2 path, Fig. 34i) and found that the energy barrier was the lowest for the A1–A1 pathway [0.3037 eV, Fig. 34o, x(Li) = 0.016] rather than for the C–C pathway [0.3894 eV, Fig. 34 n, x(Li) = 0.016] in which their C–C pathway was equivalent to path (ii) and that the energy barrier for the A2–A2 pathway [0.9381 eV, Fig. 34p, x(Li) = 0.016] was the highest.

Overall, activation energy barrier data suggest that Li-ion diffusion in rutile possesses the lowest energy barrier [e.g., 0.0254 eV [203], Fig. 34m, x(Li) = 0.014] and that diffusion in rutile is easier than in TiO_2(B) [the energy barrier = 0.3 eV [203], Fig. 34o, x(Li) = 0.016], with diffusion being least favorable in anatase [the energy barrier = 0.5 eV [203], Fig. 34l, x(Li) = 0.014]. However, the intercalation of Li in rutile is nonetheless significantly more difficult than that in the other two polymorphs, and considering both intercalation energy and activation energy, TiO_2(B) is the most promising of the three polymorphs as an anode material for LIBs.

Li-ion diffusion in LTO is usually considered in both the delithiated spinel phase $Li_4Ti_5O_{12}$ and the lithiated rock-salt phase $Li_7Ti_5O_{12}$, and Ziebarth et al. [303] systematically investigated this diffusion process with first principle calculations using a simplified model that considered the hopping of only one Li vacancy in a supercell lattice in which in the spinel phase $Li_4Ti_5O_{12}$, tetrahedral 8a sites are filled with Li-ions, whereas octahedral 16c sites are empty, meaning that the diffusion pathways mainly involved vacancy hopping between two 8a sites. Here, these researchers reported that based on their results, a traditional symmetric pathway (8a → 16c → 8a′) possessing activation energy of 0.48 eV existed for single vacancies and that the 16c site between two 8a sites that acted as the transition state was not observed and was the metastable state. However, these researchers also reported that considering the different local chemical environments caused by the random distribution of Li/Ti in 16d sites, other pathways still existed in which the other pathways (8a → 16c → 8a′) with lower energy barriers (0.30–0.36 eV) were all asymmetric and all showed a flat plateau near the middle passed 16c sites, indicating a metastable transition state. As for the rock-salt phase $Li_7Ti_5O_{12}$, these researchers reported that the 16c sites were occupied and 8a sites were empty, meaning that the main pathway was the one with vacancy hopping between two 16c sites in which the energy barrier of these diffusion pathways (16c → 8a → 16c′) was in the range of 0.2–0.51 eV and that the middle passed 8a sites for all of these pathways were not observed and were metastable transition states. Moreover, the shapes of most of these pathways were asymmetric. In this study, these researchers also investigated the mobility of Li-ions at the stable 16d sites and reported that the diffusion of one single Li vacancy from the 16d site to the 8a site was difficult (with a high energy barrier of 0.92 eV) in the spinel phase, whereas the reverse direction was much easier (with much lower activation energy of 0.42 eV), indicating that vacancies can easily be trapped in stable 16d sites, which can slow down diffusion processes in lattices. Nevertheless, the situation in the rock-salt phase was different, suggesting that vacancies were not stable in 16d sites, and therefore, the diffusion of Li-ions in rock-salt phases is easier than in the spinel phase, which is in agreement with previous reported computational results from Chen et al. [304]. However, because Li-ion diffusion for composition between spinel and rock-salt phases is complex, it is rarely reported in theoretical studies.

5.3.2 The Effects of Defects on Li-Intercalation and Diffusion Processes

5.3.2.1 Effects of OVs on Li-Intercalation OVs can have great influences on the intercalation and diffusion of Li atoms, and the effects of OVs on Li-intercalation can be evaluated by comparing the intercalation energy of Li inserting into pristine and OV-defective TiO_2 ($E^{OV}_{f,Li}$). Here, Li-intercalation in OV-defective TiO_2 can form systems with complex defects in which both OV sites and intercalation sites for Li atoms need to be considered. In addition, a combination of these two types of defect sites has many permutations, especially for TiO_2(B), because of the existence of four different OV sites (O_{br}, O_{3f1}, O_{3f2} and O_{4f}, Fig. 29b, c) and three different Li-intercalation sites (C, A1 and A2, Fig. 34a). Based on this, Yeh et al. [203] took into account all permutations and combinations of these two different sites and reported that Li-intercalation at the A2 site in TiO_2(B) with an O_{4f} OV site was unstable because it can either immigrate to a C site or possess higher energy. Furthermore, these researchers compared $E^{OV}_{f,Li}$ with $E^{P}_{f,Li}$ and found that OVs (0.69%) were detrimental for Li-intercalation in anatase and rutile but that the opposite was true for TiO_2(B) with the C-O_{4f} site combination (with OV concentration at 0.78%). Similar results for TiO_2(B) were also reported by Kong et al. [229] who reported that the voltage for Li insertion at C sites in OV-defective TiO_2(B) (OV concentration of 1.56%) was higher than that in pristine TiO_2(B), suggesting that the existence of OVs is beneficial for Li-intercalation in TiO_2(B).

As for LTO, Samin et al. [235] reported that the calculated average intercalation potential between $Li_4Ti_5O_{12}$ and $Li_7Ti_5O_{12}$ reduced from 1.26 V in pristine LTO to 1.09 V in the OV-defective structure, which represented decreased battery discharge capacities due to introduced OVs. Alternatively, Nasara et al. [131] concluded that the theoretical capacity of LTO between $Li_4Ti_5O_{12}$ and $Li_7Ti_5O_{12}$ can increase from 175 (pristine) to 180 mAh g^{-1} (6.5% OV defective) and also reported that the capacities observed from experimental results were 171.2 and 169.9 mAh g^{-1} for OV-defective and pristine LTO, respectively.

5.3.2.2 Effects of OVs on Li-Diffusion Activation energy is a good reference to evaluate the effects of OVs on Li-ion diffusion. For example, based on the energy profiles for Li-ion diffusion in OV-defective TiO_2 along with data for the pristine structure (Fig. 34l–p), Yeh et al. [203] demonstrated that compared with pristine structures, the diffusion energy barriers in OV-defective anatase and rutile [0.69% OV, x(Li/Ti) = 0.014] can increase by 0.5 and 0.4 eV, respectively (Fig. 34l, m), suggesting that OVs may hinder Li-ion diffusion in these polymorphs. Alternatively, these researchers also found that the energy barrier for the A1–A1 pathway decreased by 0.006 and 0.049 eV after the introduction of OVs (0.78%) at O_{3f1} and O_{4f} sites, respectively, for TiO_2(B) [x(Li/Ti) = 0.016] (Fig. 34o) but increased for the A1–A1 pathway with other OV sites (Fig. 34o) as well as other pathways with all types of OV sites (Fig. 34n, p). These researchers also reported that the A2–A2 pathway diffusion may not exist in TiO_2(B) with O_{br} and O_{4f} OVs (Fig. 34p) because Li-ions initially on the A2–A2 pathway will move to adjacent C sites after full relaxation of the lattice. Overall, the decreased energy barriers for the A1–A1 pathway in TiO_2(B)-O_{3f1} and TiO_2(B)-O_{4f} suggest that the diffusion of Li-ions in TiO_2(B) can become more efficient in the presence of these two types of OVs. In a further study, Kong et al. [229] suggested that the effects of OVs on Li-ion diffusion may depend on OV concentration in which the diffusion energy barrier for the C–C pathway (path (ii) in Fig. 34b) in a 1.56% OV TiO_2(B)-O_{3f1} or TiO_2(B)-O_{4f} structure is slightly higher than that in the pristine TiO_2(B) structure, which is consistent with the 0.78% OV results from Yeh et al. [203]. Nevertheless, the energy barrier for the same pathway in the same structure is lower than that with 1.56% OV and even lower than that in pristine materials at 3.12% OV. As for the effects of OVs on Li-diffusion in LTO, Nasara et al. [131] reported that the calculated diffusion coefficient for OV-defective LTO was 1.53×10^{-12} cm^2 s^{-1}, which was almost 1.9 times that for pristine LTO (8.06×10^{-13} cm^2 s^{-1}). Here, these researchers claimed that the enhanced diffusivity of Li-ions in OV-defective LTO can be attributed to wider channels created by OV-induced lattice expansion in which the expansion rate of the lattice parameter was calculated to be 0.1519%.

5.3.2.3 Effects of Li Concentration Li-intercalation and diffusion processes can also be affected by previously intercalated Li. For example, Ti–Li repulsion and the mutual repulsion of Li-ions in TiO_2(B) are two factors that can affect the stability of insertion sites [229, 232] in which the experimental and computational studies by Armstrong et al. [296] showed that C sites were the most energetically favorable for Li-ion intercalation but only with low concentrations of Li-ions [x(Li/Ti)⩽0.25]. Here, these researchers reported that at x(Li/Ti) = 0.25, all C sites were occupied and at a higher concentration range of 0.25 < x(Li/Ti)⩽0.5, A1 sites become more favorable than C sites and all A1 sites become fully occupied at x(Li/Ti) = 0.5. In addition, if x(Li/Ti) > 0.5, A2 sites become more favorable than C or A1 sites and all C, A1 and A2 sites become fully occupied at x(Li/Ti) = 1, leading to maximum Li storage capacity. Researchers have also suggested that the reason why C sites are the stablest at low Li-ion concentrations is that Li–Ti distances are maximized at C sites, thus minimizing Li–Ti repulsion [229]. And with the increasing Li content, mutual repulsion of Li-ions becomes stronger in C sites than that in A1 sites as C sites become fully occupied with Li-ions, leading to changes in the most favorable site. Similar reasons underlie the transition from A1 to A2 sites. In another study, Arrouvel et al. [232] reported that the intercalation voltage for pristine TiO_2(B) decreased from 1.64 to 1.29 V as Li content x(Li/Ti) increased from 0.031 to 0.125, indicating that Li-intercalation becomes more difficult as Li concentrations increase. Kong et al. [229] also reported similar results, showing that as x(Li/Ti) increases from 0.031 to 1, insertion voltages for pristine and OV-defective TiO_2(B) decrease from 1.29 to 0.72 V and from 1.35 to 0.69 V, respectively. Furthermore, these researchers found that the intercalation voltage of OV-defective TiO_2(B) was higher than that of pristine TiO_2(B) at lower Li concentrations [x(Li/Ti)⩽0.25] but that the voltage was lower at high Li concentrations [0.25 < x(Li/Ti)⩽1], suggesting that OVs are beneficial for both charge and discharge processes in TiO_2(B) anodes. These researchers attributed this effect to that fact that higher insertion voltages in the low Li content allow for easier lithiation in anodes during charging, whereas lower insertion voltages allow for easier delithiation in anodes during discharging.

As for Li diffusion, Olson et al. [302] showed that for anatase, activation energy decreased from 0.65 to 0.45 eV as Li content x(Li/Ti) increased from 0.03 to 0.1, suggesting that Li diffusion becomes easier with higher Li concentrations. Here, these researchers suggested that increased Li-intercalation will lead to greater amounts of charge compensated electrons, which can provide stronger coupling screening effects [302] for Li-ions, and as a result, a higher Li content is beneficial for Li-ion diffusion. Similar results for anatase have also been reported by Yildirim et al. [305], who found that energy barriers will increase with increasing the Li content only above a theoretical Li concentration limit in anatase whereas for rutile, the results were on the contrary in which the energy barrier increased by 0.2 eV as x(Li/Ti) increased from 0.1 to 0.5. Here, these researchers suggested that the channels for Li diffusion can easily be blocked (energy preferable sites becoming unavailable) in rutile due to the one dimensional diffusion mechanism whereas the diffusion mechanism for anatase involves 3D hopping between octahedral sites, which can tolerate stronger Li–Li repulsive interactions. And because the different diffusion mechanisms are determined by different structures, concentration dependence of diffusivity is structure dependent.

5.3.2.4 Effects of Other Dopants Aliovalent elemental doping of TiO_2 LIB anodes has seldom being examined by theoretical studies. As a result, limited theoretical investigations of the effects of doping with other elements on Li-intercalation in TiO_2 exist. However, Kumar et al. [263] investigated the Li-intercalation energy of C- and N-doped anatase TiO_2 by DFT using a PBE functional (a GGA type) together with the Hubbard U parameter and considered a system of anatase with one O atom substituted by one C or N atom with one or two OVs created to maintain charge neutrality in which their doped system was denoted as $TiO_{2-2x}C_x$ or $TiO_{2-3x}N_{2x}$ for C- and N-doping. Here, these researchers reported that the Li-intercalation energy for C-doped anatase was lower than that of pristine anatase with a low Li content, indicating that C-doping is beneficial for Li-intercalation in anatase. These researchers also reported that opposite results were found for N-doped anatase in which N-doping led to higher Li-intercalation energy under low Li-loading. In addition, these researchers calculated the theoretical charge capacities of LIBs with doped TiO_2 anodes using Bader charge analysis [306–308] and obtained 310, 438 and 421 mA g^{-1} for pristine, C-doped and N-doped anatase TiO_2, respectively. And to the best of our knowledge, other theoretical studies into the effects of other dopants on Li diffusion in TiO_2 have yet to be reported. As for LTO, Song et al. [281] reported that Na-doping is beneficial for Li diffusion in which based on their calculated results, the activation energy barrier for Li diffusion in Na-doped LTO (spinel $NaLi_{30}Ti_{40}O_{96}$) was ~ 0.25 eV, which was much lower than that in the undoped phase (spinel $Li_{31}Ti_{40}O_{96}$) at 0.38 eV and they attributed this effect to a lattice expansion from 8.427 to 8.443 Å.

6 Applications of TiO_2 and LTO

Ti-based oxides are frequently studied in electrochemical energy storage devices because of their promising potential for high energy density, working voltage and cycle lifes [12, 309, 310]. However, the further development of Ti-based oxides for energy storage is limited by slow kinetic behaviors during charge/discharge in which kinetics is slowed by limited active sites in TiO_2/LTO and large ionic radii (Li^+,

Na^{+}, Mg^{2+} and Al^{3+}), which slow ion insertion/extraction in metal-ion batteries [311–313]. Here, sluggish ion diffusion can be addressed by introducing defects such as vacancies, lattice distortions, unpaired electrons and Ti^{3+} [314, 315]. In addition, defects can also cause corresponding charge redistribution to balance the insertion/extraction of Li^{+} by enhancing electron diffusion. For example, extrinsic defects (ion doping) in TiO_2/LTO can generally reduce ion diffusion depth and improve intra-particle conductivity and these effects are particularly advantageous for LIBs in which ion diffusion is a rate-limiting factor. Moreover, extrinsically defective TiO_2/LTO can also be used for a range of different electrochemical energy storage devices, including SIBs, multivalent-ion batteries and supercapacitors. As for non-stoichiometric defects (vacancies), these are accompanied by disordered surface layers, accelerated ion desolvation in electrolytes and improved electron conductivity through corresponding charge compensation, all of which are advantageous for charge-transfer reactions in electrochemical energy storage devices. In summary, defective Ti-based oxides can be applied in LIBs, SIBs, multivalent-ion batteries and supercapacitors to achieve better electrochemical performance [316, 317] and in this section, defective TiO_2/LTO with vacancy-induced lattice relaxations and atom-doped lattice distortions is discussed for energy storage applications.

6.1 Lithium-Ion Batteries (LIBs)

TiO_2/LTO has widely been used as anode materials in LIBs because of rapid Li-ion insertion/extraction behaviors. However, poor electronic and ionic conductivities of TiO_2/LTO greatly limit application in electrochemical energy storage devices [110, 143, 318]. To overcome these limitations, defect structures in Ti-based oxides can promote the migration of electrons and ions in bulk phases and improve dynamic performance [315, 316]. Recently, Ti-based oxides with Ti^{3+} or OVs have also shown promise for LIBs. For example, Chen et al. [77] prepared dark rutile TiO_2 nanorods through a simple solvent-thermal method (Fig. 35a) and reported that the dark TiO_2 exhibited a higher specific capacity (92.1 mAh g^{-1}, 50 C, 1 C = 168 mA g^{-1}) and impressive capacity retention of 98.4% after 1000 cycles. Here, these researchers attributed the remarkable rate capability and extraordinary cycling stability to the optimized electronic structure resulting from Ti^{3+} and OVs. In another example, Shin et al. [219] used a hydrogen-thermal treatment method to prepare oxygen-deficient $TiO_{2-\delta}$ nanoparticles in which 1-h thermal treated TiO_2 under 5% H_2/95% Ar atmosphere (H_2-1 h-$TiO_{2-\delta}$), 1-h thermal treated TiO_2 under Ar atmosphere (Ar-1 h-$TiO_{2-\delta}$) and pristine TiO_2 were all prepared and utilized as anodes in LIBs. And as a result, these researchers reported that the conductivity of H_2-1 h-$TiO_{2-\delta}$ reached 1.5×10^{-3} S cm^{-1} and was much higher than Ar-1 h-$TiO_{2-\delta}$ and pristine TiO_2. In addition, these researchers reported that the Li^{+} storage for H_2-1 h-$TiO_{2-\delta}$ and Ar-1 h-$TiO_{2-\delta}$ showed great enhancements as compared with pristine TiO_2 and that the discharge capacities of H_2-1 h-$TiO_{2-\delta}$ and Ar-1 h-$TiO_{2-\delta}$ were 180 and 148 mAh g^{-1} at 0.2 C (1 C = 336 mA g^{-1}), respectively, whereas the pristine TiO_2 only produced 64 mAh g^{-1} (Fig. 35b).

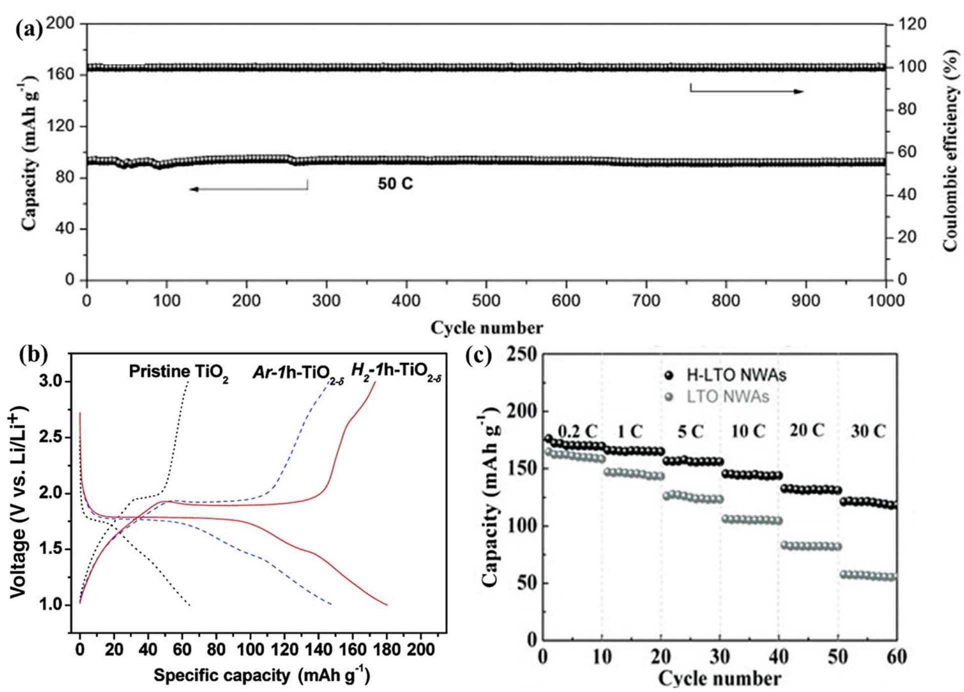

Fig. 35 **a** Cycling performance of dark TiO_2 at a rate of 50 C expressed as extraction capacity and Coulombic efficiency versus the cycle number. Reprinted with permission from Ref. [77], copyright (2018) American Chemical Society. **b** Charge/discharge profiles (at the 20th cycle) for pristine TiO_2 (the dotted line), Ar-1 h-$TiO_{2-\delta}$ (the dashed line) and H_2-1 h-$TiO_{2-\delta}$ (the solid line) cycled at 0.2 C. Reprinted with permission from Ref. [219], copyright (2012) American Chemical Society. **c** Specific discharge capacities at various C rates for LTO and H-LTO NWAs. Reprinted with permission from Ref. [318], copyright (2012) John Wiley and Sons

Furthermore, Deng et al. [319] fabricated an oxygen deficient H-TiO_2@C electrode through a hydrothermal process followed by a hydrogenation process and reported that the rich OVs induced by hydrogenation resulted in excellent pseudo-capacitive storage in which the resulting H-TiO_2@C electrode delivered a remarkable capacity of 310 mAh g^{-1} at 0.1 A g^{-1} and a higher rate performance of 126 mAh g^{-1} at 1 A g^{-1}. Qiu et al. [113] also successfully prepared blue rutile TiO_2 nanoparticles through an enhanced high-pressure hydrogenation process and reported that the blue TiO_2 possessed remarkable discharge capacities and rate performances as compared with pristine rutile TiO_2 in which outstanding discharge specific capacities of 179.8 mAh g^{-1} and 129.2 mAh g^{-1} were achieved at rates of 0.1 C and 5 C (1 C = 336 mA g^{-1}), respectively. Moreover, Qiu et al. [110] also prepared hydrogenated Li titanate (H-LTO) through a similar process and reported much higher reversible capacities and better cycling stability (134.9 mAh g^{-1} at 5 C after 100 cycles, 1 C = 175 mA g^{-1}). In another example, Shen et al. [318] used a hydrogenation process to successfully introduce Ti^{3+} in LTO nanowires (H-LTO NWAs) and reported that as compared with pristine LTO nanowires (NWAs), the H-LTO NWAs delivered much higher Li^+ storage capacities (173 mAh g^{-1} at 0.2 C) and much better rate performances (121 mAh g^{-1} at 30 C) (Fig. 35c). In addition, Chen et al. [85] used a solvothermal method with a subsequent annealing treatment to obtain defective mesoporous $Li_4Ti_5O_{12-y}$ and reported that the resulting excellent rate performances (139 mAh g^{-1} at 20 C) can be attributed to the unique defective mesoporous structure and the presence of OVs and Ti^{3+}–O^{2-}–Ti^{4+} pairs. Nasara et al. [131] also synthesized a highly oxygen-deficient LTO (the OVs content up to ~ 6.5%) from a one-pot thermal reduction process and reported that the high concentration of OVs greatly improved electronic and ionic conductivities of the LTO material as evidenced by the decreased impedance of the defective LTO electrode (Fig. 36a) as well as lowered polarization voltage and a much stronger peak current and peak symmetry (Fig. 36b), all of which can provide increased electrochemical activity and enhanced reaction kinetics as compared with pristine LTO.

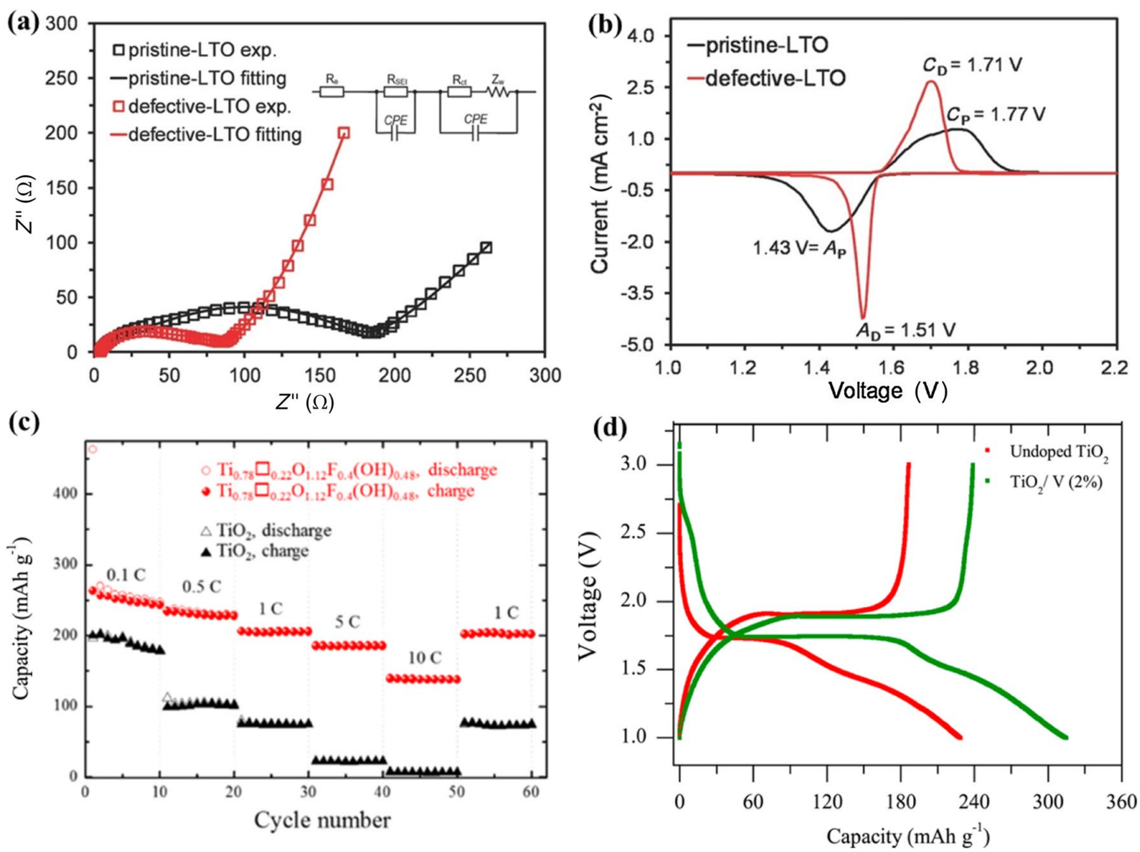

Fig. 36 **a** Electrochemical impedance spectroscopy for pristine and defective LTO. **b** Cyclic voltammetry for pristine and defective LTO. Reprinted with permission from Ref. [131], copyright (2017) John Wiley and Sons. **c** Rate capabilities of pure TiO_2 anatase and $Ti_{0.78}\square_{0.22}O_{1.12}F_{0.4}(OH)_{0.48}$ electrodes. Reprinted with permission from Ref. [320], copyright (2015) American Chemical Society. **d** Initial charge/discharge profiles of undoped and V^{5+}-doped TiO_2 electrodes. Reprinted with permission from Ref. [322], copyright (2013) Elsevier

OVs in TiO_2/LTO lattices can also enhance electron and ion transport and thus promote better rate performances and cycling stability in LIBs. In addition, atom doping-induced lattice distortions in TiO_2/LTO structures are also considered to be an effective strategy to this end. For example, Li et al. [320] prepared monovalent F^-/OH^--anion-doped TiO_2 ($Ti_{0.78}\square_{0.22}O_{1.12}F_{0.4}(OH)_{0.48}$) through a mild solvothermal process and reported outstanding electrochemical performances as compared with pure TiO_2 in which the doping of monovalent F^-/OH^- anions can cause the replacement of O^{2-} divalent ions and the disruption of the crystalline atomic structure of TiO_2. As a result, the as-synthesized $Ti_{0.78}\square_{0.22}O_{1.12}F_{0.4}(OH)_{0.48}$ possessed a uniform distribution of cationic vacancies with a concentration up to 22% and was able to deliver reversible specific capacities of 204 mAh g^{-1} and 134 mAh g^{-1} at current densities of 1 C and 10 C, respectively (Fig. 36c). In addition, even at an extremely high current density of 50 C, the sample still delivered a specific capacity of 75 mAh g^{-1} after 300 cycles. Here, these researchers attributed the improved electrochemical Li storage properties to defect chemistry and cationic vacancies, which play an important role in providing additional Li^+ diffusion pathways and enhancing the transport of Li^+. In another study, Ma et al. [321] synthesized F-doped carbon-encapsulated $Li_4Ti_5O_{12}$ composites (C-FLTOs) through a hydrothermal process and a controlled solid state lithiation reaction at high temperatures and reported that charge compensation in the lattice resulting from F-doping is beneficial to structural stability and electronic conductivity of C-FLTOs in which the optimized sample (C-FLTO with a carbon content of 2.03 wt%) delivered an outstanding charge capacity of ~ 158 mAh g^{-1} at 1 C and high rate performances up to 140 C.

In addition to anion doping, various types of cation doping have also been reported to improve the electrochemical performance of Ti-based materials. For example, Anh et al. [322] found that Vanadium (V^{5+})-doped TiO_2 synthesized through a solvothermal method following a calcination treatment gave rise to Ti^{4+} vacancies and increased ion and electronic conductivity, which enhanced the Li^+ storage performance of the V^{5+}-doped TiO_2 electrode. As a result, the optimized V^{5+}-doped TiO_2 (TiO_2/V 2%) exhibited decreased polarization voltages in initial charge/discharge profiles relative to undoped TiO_2 (Fig. 36d) in which as compared with undoped TiO_2, the TiO_2/V 2% electrode delivered a higher reversible capacity of 232.6 mAh g^{-1} at 0.1 mA cm^{-2}. In another study, Thi et al. [251] investigated the effects of Mo^{6+} doping on the electrochemical properties of TiO_2. Here, these researchers synthesized anatase-type Ti with different Mo^{6+} doping levels (1, 3, and 5 wt%) through a simple solvothermal method followed by an annealing process and reported that Mo^{6+}-doped TiO_2 with increasing numbers of Ti^{4+} vacancies showed higher conductivities and therefore led to enhanced electrochemical performances in which TiO_2 nanoparticles doped at 1, 3 and 5 wt% delivered capacities of 165.3, 169.5 and 152.7 mAh g^{-1}, respectively, after 30 cycles at 0.8 mA cm^{-2}, whereas undoped TiO_2 only delivered a capacity of 127.7 mAh g^{-1} under the same conditions. Fehse et al. [323] also prepared Nb-doped TiO_2 nanofibers through a facile, single-step electrospinning method and reported that Nb doping had significant effects on electronic structure, increased the lattice disorder in doped samples and also reduced diffusion pathway lengths and improved intra-particle conductivity. And as a result, the Nb-doped TiO_2 nanofibers possessed higher rate capabilities than non-doped materials during the electrochemical cycling process. In addition, Bai et al. [324] fabricated Y-modified $Li_4Ti_5O_{12}$ with different Y-doping contents (Y_xLTO, $x=0$–1.1) through a coprecipitation method and reported that Y-doping led to an increased lattice constant and enhanced electronic and ionic conductivities, which resulted in outstanding rate capabilities and long cycle life spans, leading to the Y_xLTO ($x=0.06$) electrode maintaining a capacity of 156.8 mAh g^{-1} at 10 C after 1000 cycles. Furthermore, Song et al. [220] fabricated $Li_{4-x/3}Ti_{5-2x/3}Cr_xO_{12}$ with an unexpected structure through ball milling following by heat treatment. Here, although doping with heterogeneous elements normally increases structural disorder, in this study, the doping of Cr^{3+} in LTO resulted in an anomalous decrease in structural disorder due to the straightening of Ti–O–Ti bonds. This decreased disorder and enhanced electronic conductivity with the introduction of Cr^{3+} subsequently contributed to exceptional electrochemical performances in which at a rate of 10 C, the $Li_{4-x/3}Ti_{5-2x/3}Cr_xO_{12}$ displayed a high discharge capacity of 125 mAh g^{-1}. In summary, the excellent electrochemical performances of defective Ti-based oxides in LIBs can be ascribed to modified electronic structures (OVs, Ti^{3+} and ion doping), shortened Li^+ diffusion pathways and enhanced diffusion of Li^+ [315, 316, 321].

6.2 Sodium-Ion Batteries (SIBs)

Similar to LIBs, the optimized electronic structure and improved electronic and ionic transport imparted by introducing defects in Ti-based oxides have also been applied to SIBs. For example, Chen et al. [325] prepared nanostructured black anatase TiO_2 with OVs through a $NaBH_4$ high temperature reduction process and used it as a SIB anode, resulting in the black TiO_2 (B-TO) delivering a high capacity of 207.6 mAh g^{-1} at a current density of 0.2 C and 91.2 mAh g^{-1} at a high current density of 20 C (Fig. 37a), which were superior to white TiO_2 (W-TO) anodes. Here, these researchers attributed such remarkably high rate capabilities and long cycling life spans to the presence of OVs, which can improve both intrinsic electrical conductivity and kinetics of the Na ion uptake-release process. In another

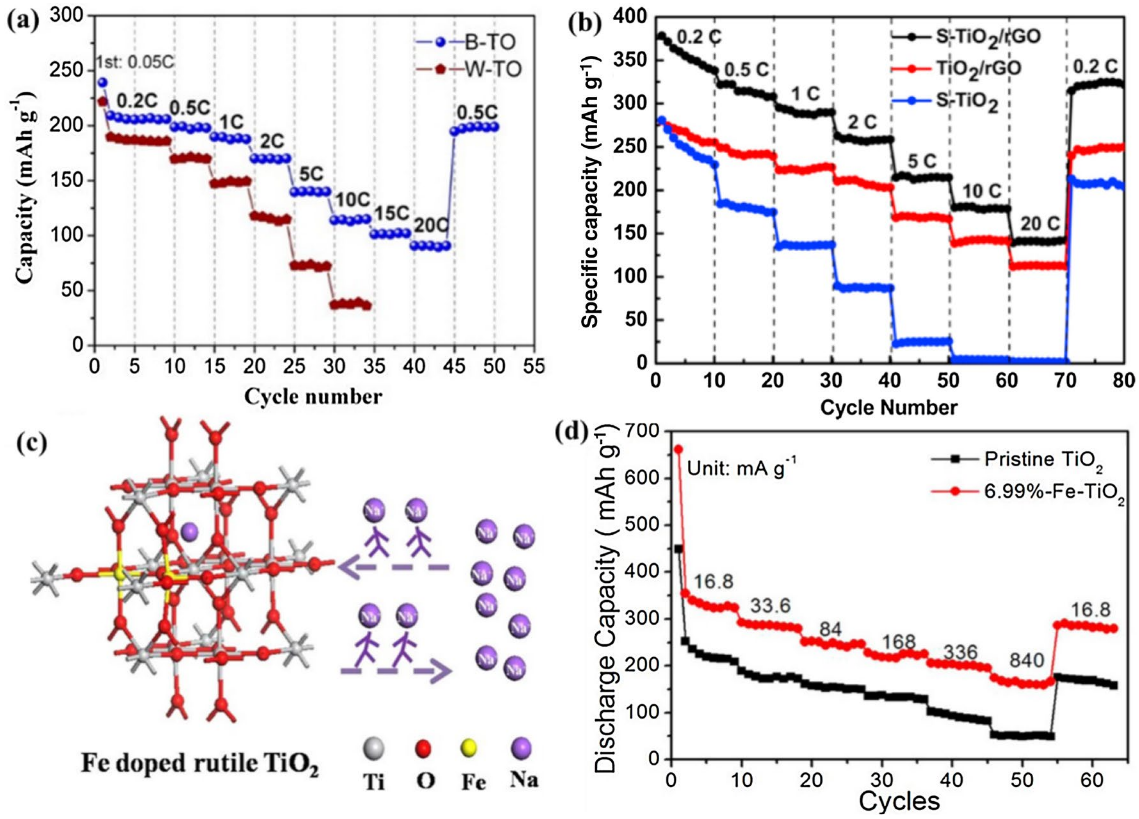

Fig. 37 **a** Rate performances of B-TO and W-TO at elevated rates expressed as Na^+ extraction capacity versus the cycle number. Reprinted with permission from Ref. [325], copyright (2016) American Chemical Society. **b** Rate capabilities of S-TiO_2/rGO, TiO_2/rGO and S-TiO_2 electrodes at different current densities. Reprinted with permission from Ref. [328], copyright (2018) Elsevier. **c** Structural models of Fe-doped-TiO_2. **d** Rate capabilities of pristine and Fe-doped TiO_2 at different currents. Reprinted (adapted) with permission from Ref. [329]. Copyright (2017) American Chemical Society

study, Zhang et al. [230] designed a blue-colored TiO_2(B) as a SIB anode and reported that the introduction of OVs in the blue TiO_2(B) allowed for higher capacities as compared with pristine white TiO_2(B) electrodes in which the blue TiO_2(B) electrode delivered a capacity of 210.5 mAh g^{-1} and 89.8 mAh g^{-1} at 0.5 C and 15 C, respectively. And by using a controlled hydrothermal process followed by heat treatment, Zhao et al. [326] successfully synthesized carbon-bonded oxygen-deficient TiO_2 nanotubes (TiO_{2-x}/C) through a carbon reduction process and reported that as an anode for SIBs, the TiO_{2-x}/C displayed superior rate capabilities of 191 mAh g^{-1} at 0.2 C and 141 mAh g^{-1} at 10 C. Here, these researchers attributed this pseudocapacitance-dominant reversible charge/discharge process to the synergy between the ultrathin nanotube structure, the existence of OVs, Ti–C bonding at the TiO_2/C interface and coherent amorphous/TiO_2(B) heterojunctions. Xiong et al. [327] also found that cation-deficient 2D nanosheet $Ti_{0.87}O_2$ as a SIB electrode can exhibit outstanding reversible capacities (490 mAh g^{-1}, 0.1 A g^{-1}), ultra-long cycle life spans and superior low-temperature capabilities for Na storage due to its unique structure which is composed of intimately hybridized $Ti_{0.87}O_2$ and N-doped graphene in which these Ti vacancies can not only promote ion transport, but also provide fully accessible sites for ion insertion.

In addition to the introduction of OVs, the production of defects through the introduction of different anions and cations is another effective strategy to improve the Na^+ storage properties of Ti-based oxides. For example, He et al. [330] synthesized a surface-defect-rich and deep-cation-site-rich S-doped rutile TiO_2 (R-TiO_{2-x}-S) through a plasma-assisted method as a SIB anode and reported that the R-TiO_{2-x}-S delivered excellent capacities of 264.8 mAh g^{-1} and 128.5 mAh g^{-1} at current densities of 50 mA g^{-1} and 10000 mA g^{-1}, respectively. Zhang et al. [328] also synthesized S-doped TiO_2 nanosheets encapsulated in graphene nanosheets (S-TiO_2/rGO) for SIBs in which calcination in a mixed gas of sulfur vapor and hydrogen at 600 °C endowed the S-TiO_2/rGO composite with rich Ti^{3+}/OV defects. And as a result, the S-TiO_2/rGO electrode exhibited outstanding rate performances (153 mAh g^{-1} at 20 C) as compared with the two control electrodes of TiO_2/rGO and S-TiO_2 (Fig. 37b).

These researchers also reported that the pseudocapacitance imparted by the 2D morphology and vacancy-rich TiO_2 nanosheets was able to deliver ultra-stable cycle performances with limited losses even after 8000 cycles. In addition, Wu et al. [331] prepared N-doped white mesoporous TiO_2 (N-MTO) nanofibers through an electrospinning method followed by annealing in which the as-spun nanofibers were first annealed in air to remove organic components and subsequently calcined under 5% NH_3/Ar atmosphere at 550 °C to introduce OVs and partial reduce Ti^{4+} to Ti^{3+}. And as a result, the N-MTO delivered a much better Na^+ storage capability of 110 mAh g^{-1} at 10 C as compared with white mesoporous TiO_2 (MTO) nanofibers and no noticeable capacity loss even after 500 cycles. Here, these researchers attributed these improved electrochemical properties to the existence of Ti^{3+} and OVs as caused by the introduction of N. Furthermore, Usui et al. [332] successfully prepared Nb-doped rutile TiO_2 ($Ti_{1-x}Nb_xO_2$, $x=0$–0.18) through a sol–gel method followed by gas deposition and the resulting $Ti_{0.94}Nb_{0.06}O_2$ electrode exhibited a high Na^+ extraction capacity of 160 mAh g^{-1} at 50 mA g^{-1} after 50 cycles. Moreover, He et al. [329] synthesized Fe-doped 3D cauliflower-like rutile TiO_2 as a SIB anode in the calcination process, and Fe ions replaced Ti^{4+} at some sites and created corresponding OVs in the TiO_2 crystal structure (Fig. 37c) with the prepared TiO_2 with 6.99% Fe doping possessing higher concentrations of OVs on the surface. And as a result, the Fe-doped TiO_2 delivered a discharge capacity of 327.1 mAh g^{-1} at 16.8 mA g^{-1} and a high rate performance of 160.5 mAh g^{-1} at 840 mA g^{-1} (Fig. 37d). Here, these improved performances were attributed to the OVs produced from Fe doping in the TiO_2 structure. In summary, the improved capacity and cycle stability of defective TiO_2/LTO for SIBs can be attributed to the introduction of OVs and non-intrinsic defects such as doping, thus enabling enhanced intrinsic electronic conductivity and fast Na-ion diffusion kinetics [79, 333–335].

6.3 Other Metal-Ion Batteries

Multivalent ion batteries such as reversible Mg- and Al-ion batteries are particularly attractive for large-scale energy storage applications due to superior theoretical volumetric energy densities. However, the development of multivalent

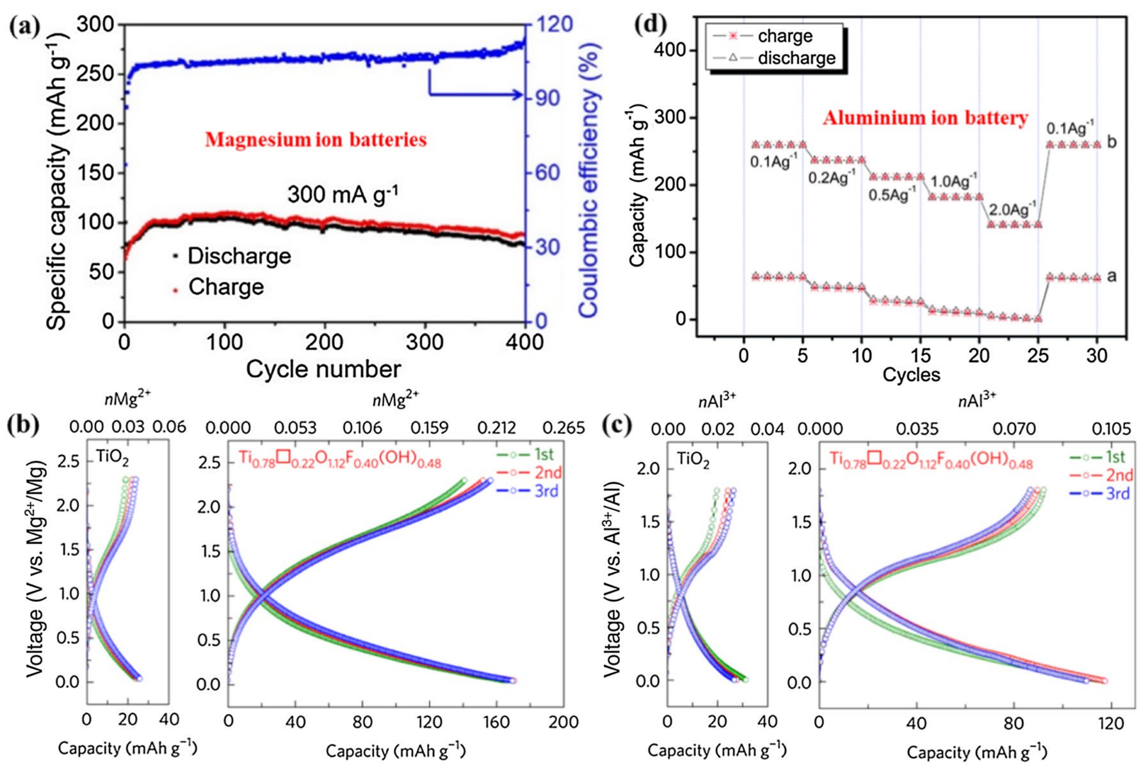

Fig. 38 **a** Electrochemical performance of porous B-TiO_{2-x} at 300 mA g^{-1} (Mg^{2+} extraction capacity vs. the cycle number). Reprinted with permission from Ref. [339], copyright (2018) American Chemical Society. **b** Galvanostatic discharge–charge curves for TiO_2 and $Ti_{0.78}\square_{0.22}O_{1.12}F_{0.40}(OH)_{0.48}$ versus Mg. Cells were cycled at 20 mA g^{-1} in the potential range 0.05–2.3 V versus Mg^{2+}/Mg. **c** Galvanostatic discharge–charge curves for TiO_2 and $Ti_{0.78}\square_{0.22}O_{1.12}F_{0.40}(OH)_{0.48}$ versus Al. Cells were cycled at 20 mA g^{-1} in the potential range 0.01–1.8 V versus Al^{3+}/Al. Reprinted with permission from Ref. [340], copyright (2017) Springer Nature. **d** Rate performances of commercial white anatase TiO_2 and black anatase TiO_2 nanoleave electrodes at different current rates. Reprinted with permission from Ref. [341], copyright (2014) Royal Society of Chemistry

batteries still faces challenges related to inherent limited ion mobility, strong kinetic barriers and lack of suitable electrode materials [336–338]. Here, the presence of OVs can play a vital role in improving the development of rechargeable Mg and Al batteries because they can enhance Mg^{2+} and Al^{3+} ion diffusion kinetics. For example, Wang et al. [339] synthesized vacancy-rich, 2D black TiO_{2-x} (B-TiO_{2-x}) nanoflakes through an efficient atomic substitution strategy and reported that the unique structure of the ultrathin porous nanoflakes can play a crucial role in the reversible Mg^{2+} storage process with discharge capacities of 150, 126, 114 and 106 mAh g^{-1} at current densities of 50, 100, 200 and 300 mA g^{-1}, respectively. These researchers also reported that even after 400 cycles at 300 mA g^{-1}, the B-TiO_{2-x} was still able to deliver a capacity of 77 mAh g^{-1} (76% retention) and demonstrated good cycling stability (Fig. 38a). In addition, both experimental results and DFT calculations have demonstrated that OVs can enhance electrical conductivity and ion diffusion kinetics and provide more active sites for multivalent ion insertion. Koketsu et al. [340] also found that prepared $Ti_{0.78}\square_{0.22}O_{1.12}F_{0.40}(OH)_{0.48}$ can present good reversible electrochemical performances for both Mg and Al ion storage in which the Mg^{2+} extraction capacity of $Ti_{0.78}\square_{0.22}O_{1.12}F_{0.40}(OH)_{0.48}$ (165 mAh g^{-1} at 20 mA g^{-1}) was much higher than that of TiO_2 (only 25 mAh g^{-1} at 20 mA g^{-1}) (Fig. 38b). Furthermore the detailed analysis of Al storage properties (Fig. 38c) showed that $Ti_{0.78}\square_{0.22}O_{1.12}F_{0.40}(OH)_{0.48}$ can deliver a discharge capacity up to 120 mAh g^{-1} at the initial cycle and further stabilized at 90 mAh g^{-1} at 20 mA g^{-1}, whereas pure TiO_2 exhibited poor intercalation properties for Al^{3+}. In another study, He et al. [341] synthesized black, well-defined nanostructured anatase TiO_2 for Al^{3+} ion storage and reported that the black anatase TiO_2 containing electro-conducting Ti^{3+} can exhibit a sustained rate capability of 141.3 mAh g^{-1} at a current density of 2.0 A g^{-1} that was much better than that of white anatase TiO_2 (Fig. 38d).

6.4 Supercapacitors

Because of its remarkably high stability, low toxicity and low costs, TiO_2 has also been considered as a potential material in electrochemical capacitors. For example, Li et al. [342] reported a facile electrochemical method to prepare Ti^{3+} self-doped anatase TiO_2 with OVs in an ethylene glycol electrolyte in which in a three-electrode system, the capacitance of the self-doped, black TiO_2 produced a significant 42-fold improvement over pristine TiO_2. In addition, the self-doping in black TiO_2 possessed significantly narrower band gaps and lower resistivities, which can greatly contribute to supercapacitor properties. In another example, Lu et al. [343] synthesized hydrogenated TiO_2 (H-TiO_2) through the calcination of anodized TiO_2 nanotube arrays (NTAs) in hydrogen atmosphere and reported that the H-TiO_2 NTAs prepared at 400 °C achieved a 40 times higher specific capacitance (3.24 mF cm^{-2},100 mV s^{-1}) as compared with air-annealed TiO_2 synthesized under the same conditions. In addition, Zhou et al. [344] prepared self-doped TiO_2 nanotube arrays through a simple cathodic polarization treatment of pristine TiO_2 nanotube arrays and reported that as an electrode material for supercapacitors, the self-doped TiO_2 nanotube arrays exhibited 39 times higher capacitance than pristine TiO_2. Kim et al. [345] also used an electrochemical self-doping method to fabricate blue and black colored TiO_2 nanotube arrays and reported that the black-colored TiO_2 nanotube arrays exhibited better capacitance than the blue TiO_2. Furthermore, Salari et al. [346] used a facile method to fabricate highly ordered OV-defective Ti nanotubes that delivered a high and stable capacitance with approximately 98% capacitance retention after 500 cycles and Wu et al. [122] prepared 1D anodic Ti oxide (ATO) nanotube arrays through a plasma-assisted hydrogenation method and investigated its electrochemical performance in supercapacitors. Here, the hydrogenated ATO delivered a higher capacity of 7.4 times (7.22 mF cm^{-2}) at a current density of 0.05 mA cm^{-2} as compared with pristine ATO and these researchers attributed the excellent rate capability and cycling stability of the prepared ATO nanotubes to the outstanding conductivity and larger specific surface areas. Overall, the introduction of OVs can enhance the capacitance in supercapacitors because they can serve as active sites to enhance adsorption properties, promote electron and ion migration and increase the density of charge carriers [317, 347, 348].

7 Summary and Outlook

Overall, this review has summarized the mechanisms of defect formation, the types of structural defects, defect-induced modifications of structural and chemical properties in TiO_2/LTO and the application of defective Ti oxides in electrochemical energy storage devices. Over the years, an array of physical, chemical and doping methods has been developed to partially reduce Ti^{4+} to Ti^{3+} or introduce OVs in lattices to improve electronic and ionic conductivities of Ti-based oxides, resulting in corresponding charge compensation and optimizations to charge carrier transportation kinetics, allowing for enhanced electronic, optical and chemical properties for defective TiO_2/LTO as compared with pristine TiO_2/LTO lattices. For example, extra mid-gap states or narrowed band gaps introduced by defects can increase the absorption of visible light, and OVs and Ti^{3+} centers can serve as shallow donors to accelerate electron mobility, and highly active surface amorphous layers can facilitate the adsorption and dissociation of reactants. And based on these improvements, defective TiO_2/LTO nanomaterials can be used in a wide range of promising energy storage applications. Furthermore, the future development of TiO_2/LTO nanomaterials for practical application in electrochemical storage applications should focus on several key areas. First, the existing technologies and methods to tune defects are relatively complex or resource intensive and it is necessary to develop effective, facile and large-scale synthetic methods to prepare and control defect structures. Second, generated OVs and Ti^{3+} are unstable in TiO_2/LTO lattices in which Ti^{3+} is prone to oxidization to Ti^{4+} by air and OVs are easily filled by dissociated oxygen in air or water, meaning further research should focus on the preservation of oxygen defects and Ti^{3+} in TiO_2/LTO lattices. Third, because defect concentrations are usually not controllable during defect formation, the quantitative control of defects can allow for more precise understanding of the effects of defects on the electronic structure and physical and on chemical properties of materials.

Overall, the creation of defects is a promising route to resolve poor electronic and ionic conductivities caused by empty Ti^{4+} 3d orbitals in Ti-based oxides and TiO_2/LTO defect structures possess many promising applications in the field of electrochemical energy generation and storage. However, further research efforts are still required, from theoretical calculations to synthetic methods, in order to improve our understanding of defective TiO_2/LTO materials and their practical application in clean energy devices.

Acknowledgements We are grateful for the financial support from the Australia Research Council Discovery Projects DP170103721 and DP180102003, the National Key R&D Program of China (2016YFB0700600), the Soft Science Research Project of Guangdong Province (No. 2017B030301013) and the Shenzhen Science and Technology Research Grant (ZDSYS201707281026184). We would also like to thank Dr. Sean E. Lowe (Griffith University) for his contributions in polishing our manuscript.

References

1. Forster, B.A.: Optimal energy use in a polluted environment. J. Environ. Econ. Manag. **7**, 321–333 (1980). https://doi.org/10.1016/0095-0696(80)90025-x
2. Chen, X., He, W., Ding, L.X., et al.: Enhancing interfacial contact in all solid state batteries with a cathode-supported solid electrolyte membrane framework. Energy Environ. Sci. **12**, 938–944 (2019). https://doi.org/10.1039/c8ee02617c
3. Chen, H., Cong, T.N., Yang, W., et al.: Progress in electrical energy storage system: a critical review. Prog. Nat. Sci. **19**, 291–312 (2009). https://doi.org/10.1016/j.pnsc.2008.07.014
4. Wang, P.J., Huang, S.M., Wu, W.C.: Electrical energy storage device. United States Patent US6373152B1, Apr. 16, 2002
5. Goodenough, J.B., Park, K.S.: The Li-ion rechargeable battery: a perspective. J. Am. Chem. Soc. **135**, 1167–1176 (2013). https://doi.org/10.1021/ja3091438
6. Xiang, H., Chen, J., Li, Z., et al.: An inorganic membrane as a separator for lithium-ion battery. J. Power Sources **196**, 8651–8655 (2011). https://doi.org/10.1016/j.jpowsour.2011.06.055
7. Jiang, Z., Xie, H., Wang, S., et al.: Perovskite membranes with vertically aligned microchannels for all-solid-state lithium batteries. Adv. Energy Mater. **8**, 1801433 (2018). https://doi.org/10.1002/aenm.201801433
8. Van Schalkwijk, W., Scrosati, B.: Advances in lithium ion batteries introduction. In: Van Schalkwijk, W.A., Scrosati, B. (eds.) Advances in Lithium-Ion Batteries, pp. 1–5. Springer, US, Boston, MA (2002)
9. Yabuuchi, N., Kubota, K., Dahbi, M., et al.: Research development on sodium-ion batteries. Chem. Rev. **114**, 11636–11682 (2014). https://doi.org/10.1021/cr500192f
10. Wang, G., Zhang, L., Zhang, J.: A review of electrode materials for electrochemical supercapacitors. Chem. Soc. Rev. **41**, 797–828 (2012). https://doi.org/10.1039/C1CS15060J
11. González, A., Goikolea, E., Barrena, J.A., et al.: Review on supercapacitors: technologies and materials. Renew. Sustain. Energy Rev. **58**, 1189–1206 (2016). https://doi.org/10.1016/j.rser.2015.12.249
12. Zhu, G.N., Wang, Y.G., Xia, Y.Y.: Ti-based compounds as anode materials for Li-ion batteries. Energy Environ. Sci. **5**, 6652–6667 (2012). https://doi.org/10.1039/C2EE03410G
13. Lan, T.B., Tu, J.X., Zou, Q.M., et al.: Synthesis of anatase TiO_2 mesocrystals with highly exposed low-index facets for enhanced electrochemical performance. Electrochim. Acta **319**, 101–109 (2019). https://doi.org/10.1016/j.electacta.2019.06.152
14. Zaleska, A.: Doped-TiO_2: a review. Recent Patents Eng. **2**, 157–164 (2008). https://doi.org/10.2174/187221208786306289
15. Mor, G.K., Varghese, O.K., Paulose, M., et al.: A review on highly ordered, vertically oriented TiO_2 nanotube arrays: fabrication, material properties, and solar energy applications. Sol. Energy Mater. Sol. Cells **90**, 2011–2075 (2006). https://doi.org/10.1016/j.solmat.2006.04.007
16. Paramasivam, I., Jha, H., Liu, N., et al.: A review of photocatalysis using self-organized TiO_2 nanotubes and other ordered oxide nanostructures. Small **8**, 3073–3103 (2012). https://doi.org/10.1002/smll.201200564
17. Xiong, H., Slater, M.D., Balasubramanian, M., et al.: Amorphous TiO_2 nanotube anode for rechargeable sodium ion batteries. J. Phys. Chem. Lett. **2**, 2560–2565 (2011). https://doi.org/10.1021/jz2012066
18. Fujishima, A., Honda, K.: Electrochemical photolysis of water at a semiconductor electrode. Nature **238**, 37–38 (1972). https://doi.org/10.1038/238037a0
19. Zhang, W., Zhang, Y., Yu, L., et al.: TiO_2-B nanowires via topological conversion with enhanced lithium-ion intercalation properties. J. Mater. Chem. A **7**, 3842–3847 (2019). https://doi.org/10.1039/C8TA10709B
20. Liu, Y., Chen, W., Yang, C., et al.: Hierarchical TiO_2-B composed of nanosheets with exposed 010 facets as a high-performance anode for lithium ion batteries. J. Power Sources **392**, 226–231 (2018). https://doi.org/10.1016/j.jpowsour.2018.04.110
21. Ding, T., Wu, J., Chen, Z., et al.: Synthesis of hierarchically mesoporous TiO_2 spheres via a emulsion polymerization route for superior lithium-ion batteries. J. Electroanal. Chem. **818**, 1–9 (2018). https://doi.org/10.1016/j.jelechem.2018.04.023
22. Liu, Y., Guo, M., Liu, Z., et al.: Rapid and facile synthesis of hierarchically mesoporous TiO_2-B with enhanced reversible capacity and rate capability. J. Mater. Chem. A **6**, 1196–1200 (2018). https://doi.org/10.1039/C7TA09264D
23. Zhang, W., Xu, T., Liu, Z., et al.: Hierarchical TiO_{2-x} imbedded with graphene quantum dots for high-performance lithium storage. Chem. Commun. **54**, 1413–1416 (2018). https://doi.org/10.1039/C7CC09406J

24. Zhang, W., Lan, T., Ding, T., et al.: Carbon coated anatase TiO_2 mesocrystals enabling ultrastable and robust sodium storage. J. Power Sources **359**, 64–70 (2017). https://doi.org/10.1016/j.jpowsour.2017.05.040
25. Liu, S., Yu, J., Jaroniec, M.: Anatase TiO_2 with dominant high-energy 001 facets: synthesis, properties, and applications. Chem. Mater. **23**, 4085–4093 (2011). https://doi.org/10.1021/cm200597m
26. Dylla, A.G., Henkelman, G., Stevenson, K.J.: Lithium insertion in nanostructured TiO_2 (B) architectures. Acc. Chem. Res. **46**, 1104–1112 (2013). https://doi.org/10.1021/ar300176y
27. Li, J., Wan, W., Zhou, H., et al.: Hydrothermal synthesis of TiO_2(B) nanowires with ultrahigh surface area and their fast charging and discharging properties in Li-ion batteries. Chem. Commun. **47**, 3439–3441 (2011). https://doi.org/10.1039/c0cc04634e
28. Rai, A.K., Anh, L.T., Gim, J., et al.: Simple synthesis and particle size effects of TiO_2 nanoparticle anodes for rechargeable lithium ion batteries. Electrochim. Acta **90**, 112–118 (2013). https://doi.org/10.1016/j.electacta.2012.11.104
29. Tian, J., Zhao, Z., Kumar, A., et al.: Recent progress in design, synthesis, and applications of one-dimensional TiO_2 nanostructured surface heterostructures: a review. Chem. Soc. Rev. **43**, 6920–6937 (2014). https://doi.org/10.1039/C4CS00180J
30. Chen, X., Selloni, A.: Introduction: titanium dioxide (TiO_2) nanomaterials. Chem. Rev. **114**, 9281–9282 (2014). https://doi.org/10.1021/cr500422r
31. Ge, M.Z., Cai, J.S., Iocozzia, J., et al.: A review of TiO_2 nanostructured catalysts for sustainable H_2 generation. Int. J. Hydrogen Energy **42**, 8418–8449 (2017). https://doi.org/10.1016/j.ijhydene.2016.12.052
32. Reddy, K.M., Manorama, S.V., Reddy, A.R.: Bandgap studies on anatase titanium dioxide nanoparticles. Mater. Chem. Phys. **78**, 239–245 (2003). https://doi.org/10.1016/S0254-0584(02)00343-7
33. Zhao, B., Ran, R., Liu, M.L., et al.: A comprehensive review of $Li_4Ti_5O_{12}$-based electrodes for lithium-ion batteries: the latest advancements and future perspectives. Mater. Sci. Eng. R Rep. **98**, 1–71 (2015). https://doi.org/10.1016/j.mser.2015.10.001
34. Zhang, Y.L., Hu, X.B., Xu, Y.L., et al.: Recent progress of $Li_4Ti_5O_{12}$ with different morphologies as anode material. Acta Chim. Sin. **71**, 1341–1353 (2013). https://doi.org/10.6023/A13040423
35. Lin, X., Pan, F., Wang, H.: Progress of $Li_4Ti_5O_{12}$ anode material for lithium ion batteries. Mater. Technol. **29**, A82–A87 (2014). https://doi.org/10.1179/1753555714Y.0000000170
36. Yu, L., Wu, H.B., Lou, X.W.: Mesoporous $Li_4Ti_5O_{12}$ hollow spheres with enhanced lithium storage capability. Adv. Mater. **25**, 2296–2300 (2013). https://doi.org/10.1002/adma.201204912
37. Zhao, L., Hu, Y.S., Li, H., et al.: Porous $Li_4Ti_5O_{12}$ coated with N-doped carbon from ionic liquids for Li-ion batteries. Adv. Mater. **23**, 1385–1388 (2011). https://doi.org/10.1002/adma.201003294
38. Shi, Y., Gao, J., Abruna, H.D., et al.: Rapid synthesis of $Li_4Ti_5O_{12}$/graphene composite with superior rate capability by a microwave-assisted hydrothermal method. Nano Energy **8**, 297–304 (2014). https://doi.org/10.1016/j.nanoen.2014.06.009
39. He, Y., Muhetaer, A., Li, J., et al.: Ultrathin $Li_4Ti_5O_{12}$ nanosheet based hierarchical microspheres for high-rate and long-cycle life Li-ion batteries. Adv. Energy Mater. **7**, 1700950 (2017). https://doi.org/10.1002/aenm.201700950
40. Shen, L., Zhang, X., Uchaker, E., et al.: $Li_4Ti_5O_{12}$ nanoparticles embedded in a mesoporous carbon matrix as a superior anode material for high rate lithium ion batteries. Adv. Energy Mater. **2**, 691–698 (2012). https://doi.org/10.1002/aenm.201100720
41. Wang, Y.-Q., Gu, L., Guo, Y.-G., et al.: Rutile-TiO_2 nanocoating for a high-rate $Li_4Ti_5O_{12}$ anode of a lithium-ion battery. J. Am. Chem. Soc. **134**, 7874–7879 (2012). https://doi.org/10.1021/ja301266w
42. Naldoni, A., Allieta, M., Santangelo, S., et al.: Effect of nature and location of defects on bandgap narrowing in black TiO_2 nanoparticles. J. Am. Chem. Soc. **134**, 7600–7603 (2012). https://doi.org/10.1021/ja3012676
43. Cho, E., Han, S., Ahn, H.S., et al.: First-principles study of point defects in rutile TiO_{2-x}. Phys. Rev. B **73**, 193202 (2006). https://doi.org/10.1103/PhysRevB.73.193202
44. Yu, X., Kim, B., Kim, Y.K.: Highly enhanced photoactivity of anatase TiO_2 nanocrystals by controlled hydrogenation-induced surface defects. ACS Catal. **3**, 2479–2486 (2013). https://doi.org/10.1021/cs4005776
45. Xu, H., Chen, J., Li, Y., et al.: Fabrication of $Li_4Ti_5O_{12}$-TiO_2 nanosheets with structural defects as high-rate and long-life anodes for lithium-ion batteries. Sci. Rep. **7**, 2960 (2017). https://doi.org/10.1038/s41598-017-03149-2
46. Fischer, S., Munz, A.W., Schierbaum, K.-D., et al.: The geometric structure of intrinsic defects at TiO_2 (110) surfaces: an STM study. Surf. Sci. **337**, 17–30 (1995). https://doi.org/10.1016/0039-6028(95)00572-2
47. Göpel, W., Anderson, J.A., Frankel, D., et al.: Surface defects of TiO_2(110): a combined XPS, XAES and ELS study. Surf. Sci. **139**, 333–346 (1984). https://doi.org/10.1016/0039-6028(84)90054-2
48. Morgan, B.J., Watson, G.W.: Intrinsic n-type defect formation in TiO_2: a comparison of rutile and anatase from GGA + U calculations. J. Phys. Chem. C **114**, 2321–2328 (2010). https://doi.org/10.1021/jp9088047
49. Czoska, A., Livraghi, S., Chiesa, M., et al.: The nature of defects in fluorine-doped TiO_2. J. Phys. Chem. C **112**, 8951–8956 (2008). https://doi.org/10.1021/jp8004184
50. Di Valentin, C., Pacchioni, G., Selloni, A.: Reduced and n-type doped TiO_2: nature of Ti^{3+} species. J. Phys. Chem. C **113**, 20543–20552 (2009). https://doi.org/10.1021/jp9061797
51. Tachikawa, T., Ishigaki, T., Li, J.G., et al.: Defect-mediated photoluminescence dynamics of Eu^{3+}-doped TiO_2 nanocrystals revealed at the single-particle or single-aggregate level. Angew. Chem. Int. Ed. **47**, 5348–5352 (2008). https://doi.org/10.1002/anie.200800528
52. Kong, L., Wang, C., Zheng, H., et al.: Defect-induced yellow color in Nb-doped TiO_2 and its impact on visible-light photocatalysis. J. Phys. Chem. C **119**, 16623–16632 (2015). https://doi.org/10.1021/acs.jpcc.5b03448
53. Kofstad, P.: Thermogravimetric studies of the defect structure of rutile (TiO_2). J. Phys. Chem. Solids **23**, 1579–1586 (1962). https://doi.org/10.1016/0022-3697(62)90240-8
54. Marucco, J.-F., Gautron, J., Lemasson, P.: Thermogravimetric and electrical study of non-stoichiometric titanium dioxide TiO_{2-x}, between 800 and 1100°C. J. Phys. Chem. Solids **42**, 363–367 (1981). https://doi.org/10.1016/0022-3697(81)90043-3
55. Millot, F., Picard, C.: Oxygen self-diffusion in non-stoichiometric rutile TiO_{2-x} at high temperature. Solid State Ionics **28**, 1344–1348 (1988). https://doi.org/10.1016/0167-2738(88)90384-0
56. Catlow, C.R.A., James, R.: Disorder in TiO_{2-x}. Proc. R. Soc. Lond. Ser. A Math. Phys. Eng. Sci. **384**, 157–173 (1982). https://doi.org/10.1098/rspa.1982.0152
57. Menetrey, M., Markovits, A., Minot, C., et al.: Formation of Schottky defects at the surface of MgO, TiO_2, and SnO_2: a comparative density functional theoretical study. J. Phys. Chem. B **108**, 12858–12864 (2004). https://doi.org/10.1021/jp048497c
58. Weibel, A., Bouchet, R., Knauth, P.: Electrical properties and defect chemistry of anatase (TiO_2). Solid State Ionics **177**, 229–236 (2006). https://doi.org/10.1016/j.ssi.2005.11.002

59. Bak, T., Nowotny, J., Sucher, N.J., et al.: Effect of crystal imperfections on reactivity and photoreactivity of TiO_2 (rutile) with oxygen, water, and bacteria. J. Phys. Chem. C **115**, 15711–15738 (2011). https://doi.org/10.1021/jp2027862
60. Batzill, M., Katsiev, K., Gaspar, D.J., et al.: Variations of the local electronic surface properties of TiO_2 (110) induced by intrinsic and extrinsic defects. Phys. Rev. B **66**, 235401 (2002). https://doi.org/10.1103/PhysRevB.66.235401
61. Nowotny, J., Bak, T., Nowotny, M.K., et al.: Defect chemistry and electrical properties of titanium dioxide. 1. Defect diagrams. J. Phys. Chem. C **112**, 590–601 (2008). https://doi.org/10.1021/jp074565u
62. Hoshino, K., Peterson, N.L., et al.: Diffusion and point-defects in TiO_{2-x}. J. Phys. Chem. Solids **46**, 1397–1411 (1985). https://doi.org/10.1016/0022-3697(85)90079-4
63. Carneiro, J., Azevedo, S., Fernandes, F., et al.: Synthesis of iron-doped TiO_2 nanoparticles by ball-milling process: the influence of process parameters on the structural, optical, magnetic, and photocatalytic properties. J. Mater. Sci. **49**, 7476–7488 (2014). https://doi.org/10.1007/s10853-014-8453-3
64. Serpone, N.: Is the band gap of pristine TiO_2 narrowed by anion- and cation-doping of titanium dioxide in second-generation photocatalysts? J. Phys. Chem. B **110**, 24287–24293 (2006). https://doi.org/10.1021/jp065659r
65. Wang, J., Tafen, D.N., Lewis, J.P., et al.: Origin of photocatalytic activity of nitrogen-doped TiO_2 nanobelts. J. Am. Chem. Soc. **131**, 12290–12297 (2009). https://doi.org/10.1021/ja903781h
66. Huang, H., Li, X., Wang, J., et al.: Anionic group self-doping as a promising strategy: band-gap engineering and multi-functional applications of high-performance CO_3^{2-}-doped $Bi_2O_2CO_3$. ACS Catal. **5**, 4094–4103 (2015). https://doi.org/10.1021/acscatal.5b00444
67. Sathish, M., Viswanathan, B., Viswanath, R., et al.: Synthesis, characterization, electronic structure, and photocatalytic activity of nitrogen-doped TiO_2 nanocatalyst. Chem. Mater. **17**, 6349–6353 (2005). https://doi.org/10.1021/cm052047v
68. Chen, X., Burda, C.: The electronic origin of the visible-light absorption properties of C-, N-and S-doped TiO_2 nanomaterials. J. Am. Chem. Soc. **130**, 5018–5019 (2008). https://doi.org/10.1021/ja711023z
69. Luo, N.J., Jiang, Z., Shi, H.H., et al.: Photo-catalytic conversion of oxygenated hydrocarbons to hydrogen over heteroatom-doped TiO_2 catalysts. Int. J. Hydrogen Energy **34**, 125–129 (2009). https://doi.org/10.1016/j.ijhydene.2008.09.097
70. Sathish, M., Viswanath, R.P., Gopinath, C.S.: N,S-co-doped TiO_2 nanophotocatalyst: synthesis, electronic structure and photocatalysis. J. Nanosci. Nanotechnol. **9**, 423–432 (2009). https://doi.org/10.1166/jnn.2009.j095
71. Zhen, C., Wang, L., Liu, L., et al.: Nonstoichiometric rutile TiO_2 photoelectrodes for improved photoelectrochemical water splitting. Chem. Commun. **49**, 6191–6193 (2013). https://doi.org/10.1039/c3cc42458h
72. He, J., Behera, R., Finnis, M., et al.: Prediction of high-temperature point defect formation in TiO_2 from combined ab initio and thermodynamic calculations. Acta Mater. **55**, 4325–4337 (2007). https://doi.org/10.1016/j.actamat.2007.04.005
73. Amade, R., Heitjans, P., Indris, S., et al.: Defect formation during high-energy ball milling in TiO_2 and its relation to the photocatalytic activity. J. Photochem. Photobiol. A Chem. **207**, 231–235 (2009). https://doi.org/10.1016/j.jphotochem.2009.07.015
74. Wu, Q., Zheng, Q., van de Krol, R.: Creating oxygen vacancies as a novel strategy to form tetrahedrally coordinated Ti^{4+} in Fe/TiO_2 nanoparticles. J. Phys. Chem. C **116**, 7219–7226 (2012). https://doi.org/10.1021/jp212577g
75. Chen, X., Liu, L., Peter, Y.Y., et al.: Increasing solar absorption for photocatalysis with black hydrogenated titanium dioxide nanocrystals. Science **331**, 746–750 (2011). https://doi.org/10.1126/science.1200448
76. Xin, X., Xu, T., Yin, J., et al.: Management on the location and concentration of Ti^{3+} in anatase TiO_2 for defects-induced visible-light photocatalysis. Appl. Catal. B **176**, 354–362 (2015). https://doi.org/10.1016/j.apcatb.2015.04.016
77. Chen, J., Song, W., Hou, H., et al.: Ti^{3+} self-doped dark rutile TiO_2 ultrafine nanorods with durable high-rate capability for lithium-ion batteries. Adv. Funct. Mater. **25**, 6793–6801 (2015). https://doi.org/10.1002/adfm.201502978
78. Kirner, U., Schierbaum, K., Göpel, W., et al.: Low and high temperature TiO_2 oxygen sensors. Sensors Actuators B Chem. **1**, 103–107 (1990). https://doi.org/10.1016/0925-4005(90)80181-X
79. Ou, G., Xu, Y., Wen, B., et al.: Tuning defects in oxides at room temperature by lithium reduction. Nat. Commun. **9**, 1302 (2018). https://doi.org/10.1038/s41467-018-03765-0
80. Feng, H., Xu, Z., Ren, L., et al.: Activating titania for efficient electrocatalysis by vacancy engineering. ACS Catal. **8**, 4288–4293 (2018). https://doi.org/10.1021/acscatal.8b00719
81. Ghosh, S., Khan, G.G., Mandal, K., et al.: Evolution of vacancy-type defects, phase transition, and intrinsic ferromagnetism during annealing of nanocrystalline TiO_2 studied by positron annihilation spectroscopy. J. Phys. Chem. C **117**, 8458–8467 (2013). https://doi.org/10.1021/jp3115836
82. Xia, T., Zhang, Y., Murowchick, J., et al.: Vacuum-treated titanium dioxide nanocrystals: optical properties, surface disorder, oxygen vacancy, and photocatalytic activities. Catal. Today **225**, 2–9 (2014). https://doi.org/10.1016/j.cattod.2013.08.026
83. Xia, T., Zhang, W., Murowchick, J.B., et al.: A facile method to improve the photocatalytic and lithium-ion rechargeable battery performance of TiO_2 nanocrystals. Adv. Energy Mater. **3**, 1516–1523 (2013). https://doi.org/10.1002/aenm.201300294
84. Guillemot, F., Porte, M., Labrugère, C., et al.: Ti^{4+} to Ti^{3+} conversion of TiO_2 uppermost layer by low-temperature vacuum annealing: interest for titanium biomedical applications. J. Colloid Interface Sci. **255**, 75–78 (2002). https://doi.org/10.1006/jcis.2002.8623
85. Chen, X., Guan, X., Li, L., et al.: Defective mesoporous $Li_4Ti_5O_{12-y}$: an advanced anode material with anomalous capacity and cycling stability at a high rate of 20 C. J. Power Sources **210**, 297–302 (2012). https://doi.org/10.1016/j.jpowsour.2012.03.014
86. Pan, X., Ma, X.: Study on the milling-induced transformation in TiO_2 powder with different grain sizes. Mater. Lett. **58**, 513–515 (2004). https://doi.org/10.1016/S0167-577X(03)00536-6
87. Pan, X., Ma, X.: Phase transformations in nanocrystalline TiO_2 milled in different milling atmospheres. J. Solid State Chem. **177**, 4098–4103 (2004). https://doi.org/10.1016/j.jssc.2004.08.017
88. Sepelak, V., Begin-Colin, S., Le Caer, G.: Transformations in oxides induced by high-energy ball-milling. Dalton Trans. **41**, 11927–11948 (2012). https://doi.org/10.1039/c2dt30349c
89. Indris, S., Amade, R., Heitjans, P., et al.: Preparation by high-energy milling, characterization, and catalytic properties of nanocrystalline TiO_2. J. Phys. Chem. B **109**, 23274–23278 (2005). https://doi.org/10.1021/jp054586t
90. Ren, R.M., Yang, Z.G., Shaw, L.L.: Polymorphic transformation and powder characteristics of TiO_2 during high energy milling. J. Mater. Sci. **35**, 6015–6026 (2000). https://doi.org/10.1023/A:1026751017284
91. Marinel, S., Choi, D.H., Heuguet, R., et al.: Broadband dielectric characterization of TiO_2 ceramics sintered through microwave and conventional processes. Ceram. Int. **39**, 299–306 (2013). https://doi.org/10.1016/j.ceramint.2012.06.025

92. Chen, Y., Li, W., Wang, J., et al.: Microwave-assisted ionic liquid synthesis of Ti^{3+} self-doped TiO_2 hollow nanocrystals with enhanced visible-light photoactivity. Appl. Catal. B **191**, 94–105 (2016). https://doi.org/10.1016/j.apcatb.2016.03.021
93. Ishida, Y., Doshin, W., Tsukamoto, H., et al.: Black TiO_2 nanoparticles by a microwave-induced plasma over titanium complex aqueous solution. Chem. Lett. **44**, 1327–1329 (2015). https://doi.org/10.1246/cl.150531
94. Choi, J., Park, H., Hoffmann, M.R., et al.: Effects of single metal-ion doping on the visible-light photoreactivity of TiO_2. J. Phys. Chem. C **114**, 783–792 (2009). https://doi.org/10.1021/jp908088x
95. Di Valentin, C., Pacchioni, G.: Trends in non-metal doping of anatase TiO_2: B, C, N and F. Catal. Today **206**, 12–18 (2013). https://doi.org/10.1016/j.cattod.2011.11.030
96. Yang, X., Zhang, M.J., Min, Y., et al.: Controllable formation of (004)-orientated Nb: TiO_2 for High-Performance transparent conductive oxide thin films with tunable near-infrared transmittance. ACS Appl. Mater. Interfaces. **9**, 29021–29029 (2017). https://doi.org/10.1021/acsami.7b06792
97. Lan, T., Zhang, W., Wu, N.L., et al.: Nb-doped rutile TiO_2 mesocrystals with enhanced lithium storage properties for lithium ion battery. Chem. A Eur. J. **23**, 5059–5065 (2017). https://doi.org/10.1002/chem.201605115
98. Pathak, S.K., Abate, A., Ruckdeschel, P., et al.: Performance and stability enhancement of dye-sensitized and perovskite solar cells by Al doping of TiO_2. Adv. Funct. Mater. **24**, 6046–6055 (2014). https://doi.org/10.1002/adfm.201401658
99. Zhang, Y., Meng, Y., Zhu, K., et al.: Copper-doped titanium dioxide bronze nanowires with superior high rate capability for lithium ion batteries. ACS Appl. Mater. Interfaces. **8**, 7957–7965 (2016). https://doi.org/10.1021/acsami.5b10766
100. Ali, Z., Cha, S.N., Sohn, J.I., et al.: Design and evaluation of novel Zn doped mesoporous TiO_2 based anode material for advanced lithium ion batteries. J. Mater. Chem. **22**, 17625–17629 (2012). https://doi.org/10.1039/C2JM33315E
101. Kashale, A.A., Rasal, A.S., Kamble, G.P., et al.: Biosynthesized Co-doped TiO_2 nanoparticles based anode for lithium-ion battery application and investigating the influence of dopant concentrations on its performance. Compos. Part B Eng. **167**, 44–50 (2019). https://doi.org/10.1016/j.compositesb.2018.12.001
102. Hong, Z., Kang, M., Chen, X., et al.: Synthesis of mesoporous Co^{2+}-doped TiO_2 nanodisks derived from metal organic frameworks with improved sodium storage performance. ACS Appl. Mater. Interfaces **9**, 32071–32079 (2017). https://doi.org/10.1021/acsami.7b06290
103. Zhang, W., Zhou, W., Wright, J.H., et al.: Mn-doped TiO_2 nanosheet-based spheres as anode materials for lithium-ion batteries with high performance at elevated temperatures. ACS Appl. Mater. Interfaces. **6**, 7292–7300 (2014). https://doi.org/10.1021/am500604p
104. Wang, J., Yang, G., Wang, L., et al.: In-situ fabrication of transition-metal-doped TiO_2 nanofiber/nanosheet structure for high-performance Li storage. J. Alloys Compd. **787**, 1110–1119 (2019). https://doi.org/10.1016/j.jallcom.2019.02.152
105. Serpone, N., Lawless, D., Disdier, J., et al.: Spectroscopic, photoconductivity, and photocatalytic studies of TiO_2 colloids: naked and with the lattice doped with Cr^{3+}, Fe^{3+}, and V^{5+} cations. Langmuir **10**, 643–652 (1994). https://doi.org/10.1021/la00015a010
106. Yang, K., Dai, Y., Huang, B.: Understanding photocatalytic activity of S-and P-doped TiO_2 under visible light from first-principles. J. Phys. Chem. C **111**, 18985–18994 (2007). https://doi.org/10.1021/jp0756350
107. Feng, N., Liu, F., Huang, M., et al.: Unravelling the efficient photocatalytic activity of boron-induced Ti(3+) species in the surface layer of TiO_2. Sci. Rep. **6**, 34765 (2016). https://doi.org/10.1038/srep34765
108. Irie, H., Watanabe, Y., Hashimoto, K.: Nitrogen-concentration dependence on photocatalytic activity of $TiO_{2-x}N_x$ powders. J. Phys. Chem. B **107**, 5483–5486 (2003). https://doi.org/10.1021/jp030133h
109. Qi, Y., Huang, Y., Jia, D., et al.: Preparation and characterization of novel spinel $Li_4Ti_5O_{12-x}Br_x$ anode materials. Electrochim. Acta **54**(21), 4772–4776 (2009). https://doi.org/10.1016/j.electacta.2009.04.010
110. Qiu, J., Lai, C., Gray, E., et al.: Blue hydrogenated lithium titanate as a high-rate anode material for lithium-ion batteries. J. Mater. Chem. A **2**, 6353–6358 (2014). https://doi.org/10.1039/C4TA00556B
111. Jiang, X., Zhang, Y., Jiang, J., et al.: Characterization of oxygen vacancy associates within hydrogenated TiO_2: a positron annihilation study. J. Phys. Chem. C **116**, 22619–22624 (2012). https://doi.org/10.1021/jp307573c
112. Wang, G., Wang, H., Ling, Y., et al.: Hydrogen-treated TiO_2 nanowire arrays for photoelectrochemical water splitting. Nano Lett. **11**, 3026–3033 (2011). https://doi.org/10.1021/nl201766h
113. Qiu, J., Li, S., Gray, E., et al.: Hydrogenation synthesis of blue TiO_2 for high-performance lithium-ion batteries. J. Phys. Chem. C **118**, 8824–8830 (2014). https://doi.org/10.1021/jp501819p
114. Lu, H.Q., Zhao, B.B., Pan, R.L., et al.: Safe and facile hydrogenation of commercial Degussa P25 at room temperature with enhanced photocatalytic activity. RSC Adv. **4**, 1128–1132 (2014). https://doi.org/10.1039/c3ra44493g
115. Cai, J., Wang, Y., Zhu, Y., et al.: In situ formation of disorder-engineered TiO_2 (B)-anatase heterophase junction for enhanced photocatalytic hydrogen evolution. ACS Appl. Mater. Interfaces. **7**, 24987–24992 (2015). https://doi.org/10.1021/acsami.5b07318
116. Su, T., Yang, Y., Na, Y., et al.: An insight into the role of oxygen vacancy in hydrogenated TiO_2 nanocrystals in the performance of dye-sensitized solar cells. ACS Appl. Mater. Interfaces. **7**, 3754–3763 (2015). https://doi.org/10.1021/am5085447
117. Wu, M.C., Chang, I.C., Hsiao, K.C., et al.: Highly visible-light absorbing black TiO_2 nanocrystals synthesized by sol–gel method and subsequent heat treatment in low partial pressure H_2. J. Taiwan Inst. Chem. Eng. **63**, 430–435 (2016). https://doi.org/10.1016/j.jtice.2016.02.026
118. Liu, N., Schneider, C., Freitag, D., et al.: Black TiO_2 nanotubes: cocatalyst-free open-circuit hydrogen generation. Nano Lett. **14**, 3309–3313 (2014). https://doi.org/10.1021/nl500710j
119. Wang, W., Lu, C., Ni, Y., et al.: A new sight on hydrogenation of F and NF doped 0 0 1 facets dominated anatase TiO_2 for efficient visible light photocatalyst. Appl. Catal. B **127**, 28–35 (2012). https://doi.org/10.1016/j.apcatb.2012.08.002
120. Hoang, S., Berglund, S.P., Hahn, N.T., et al.: Enhancing visible light photo-oxidation of water with TiO_2 nanowire arrays via cotreatment with H_2 and NH_3: synergistic effects between Ti^{3+} and N. J. Am. Chem. Soc. **134**, 3659–3662 (2012). https://doi.org/10.1021/ja211369s
121. Yan, Y., Han, M., Konkin, A., et al.: Slightly hydrogenated TiO_2 with enhanced photocatalytic performance. J. Mater. Chem. A **2**, 12708–12716 (2014). https://doi.org/10.1039/c4ta02192d
122. Wu, H., Xu, C., Xu, J., et al.: Enhanced supercapacitance in anodic TiO_2 nanotube films by hydrogen plasma treatment. Nanotechnology **24**, 455401 (2013). https://doi.org/10.1088/0957-4484/24/45/455401
123. Yang, C., Wang, Z., Lin, T., et al.: Core-shell nanostructured "black" rutile titania as excellent catalyst for hydrogen production enhanced by sulfur doping. J. Am. Chem. Soc. **135**, 17831–17838 (2013). https://doi.org/10.1021/ja4076748
124. Lin, T., Yang, C., Wang, Z., et al.: Effective nonmetal incorporation in black titania with enhanced solar energy utilization.

Energy Environ. Sci. **7**, 967–972 (2014). https://doi.org/10.1039/C3EE42708K
125. Ye, M., Jia, J., Wu, Z., et al.: Synthesis of black TiO_x nanoparticles by Mg reduction of TiO_2 nanocrystals and their application for solar water evaporation. Adv. Energy Mater. **7**, 1601811 (2017). https://doi.org/10.1002/aenm.201601811
126. Zheng, Z., Huang, B., Meng, X., et al.: Metallic zinc-assisted synthesis of Ti^{3+} self-doped TiO_2 with tunable phase composition and visible-light photocatalytic activity. Chem. Commun. **49**, 868–870 (2013). https://doi.org/10.1039/c2cc37976g
127. Sinhamahapatra, A., Jeon, J.-P., Yu, J.-S.: A new approach to prepare highly active and stable black titania for visible light-assisted hydrogen production. Energy Environ. Sci. **8**, 3539–3544 (2015). https://doi.org/10.1039/C5EE02443A
128. Ariyanti, D., Mills, L., Dong, J., et al.: $NaBH_4$ modified TiO_2: defect site enhancement related to its photocatalytic activity. Mater. Chem. Phys. **199**, 571–576 (2017). https://doi.org/10.1016/j.matchemphys.2017.07.054
129. Xu, J., Qi, X., Luo, C., et al.: Synthesis and enhanced microwave absorption properties: a strongly hydrogenated TiO_2 nanomaterial. Nanotechnology **28**, 425701 (2017). https://doi.org/10.1088/1361-6528/aa81ba
130. Chen, S., Xiao, Y., Wang, Y., et al.: A facile approach to prepare black TiO_2 with oxygen vacancy for enhancing photocatalytic activity. Nanomaterials **8**, 245 (2018). https://doi.org/10.3390/nano8040245
131. Nasara, R.N., Tsai, P.C., Lin, S.K.: One-step synthesis of highly oxygen-deficient lithium titanate oxide with conformal amorphous carbon coating as anode material for lithium ion batteries. Adv. Mater. Interfaces **4**, 1700329 (2017). https://doi.org/10.1002/admi.201700329
132. Tominaka, S., Tsujimoto, Y., Matsushita, Y., et al.: Synthesis of nanostructured reduced titanium oxide: crystal structure transformation maintaining nanomorphology. Angew. Chem. Int. Ed. **50**, 7418–7421 (2011). https://doi.org/10.1002/anie.201101432
133. Mao, C., Zuo, F., Hou, Y., et al.: In situ preparation of a Ti^{3+} self-doped TiO_2 film with enhanced activity as photoanode by N_2H_4 reduction. Angew. Chem. Int. Ed. **53**, 10485–10489 (2014). https://doi.org/10.1002/anie.201406017
134. Ullattil, S.G., Periyat, P.: A 'one pot' gel combustion strategy towards Ti^{3+} self-doped 'black'anatase TiO_{2-x} solar photocatalyst. J. Mater. Chem. A **4**, 5854–5858 (2016). https://doi.org/10.1039/C6TA01993E
135. Zou, X., Liu, J., Su, J., et al.: Facile synthesis of thermal-and photostable titania with paramagnetic oxygen vacancies for visible-light photocatalysis. Chem. A Eur. J. **19**, 2866–2873 (2013). https://doi.org/10.1002/chem.201202833
136. Zhang, Z., Hedhili, M.N., Zhu, H., et al.: Electrochemical reduction induced self-doping of Ti^{3+} for efficient water splitting performance on TiO_2 based photoelectrodes. Phys. Chem. Chem. Phys. **15**, 15637–15644 (2013). https://doi.org/10.1039/c3cp52759j
137. Dong, J., Han, J., Liu, Y., et al.: Defective black TiO_2 synthesized via anodization for visible-light photocatalysis. ACS Appl. Mater. Interfaces. **6**, 1385–1388 (2014). https://doi.org/10.1021/am405549p
138. Grabstanowicz, L.R., Gao, S., Li, T., et al.: Facile oxidative conversion of TiH_2 to high-concentration Ti^{3+}-self-doped rutile TiO_2 with visible-light photoactivity. Inorg. Chem. **52**, 3884–3890 (2013). https://doi.org/10.1021/ic3026182
139. Liu, X., Xu, H., Grabstanowicz, L.R., et al.: Ti^{3+} self-doped TiO_{2-x} anatase nanoparticles via oxidation of TiH_2 in H_2O_2. Catal. Today **225**, 80–89 (2014). https://doi.org/10.1016/j.cattod.2013.08.025
140. Zhu, Q., Peng, Y., Lin, L., et al.: Stable blue TiO_{2-x} nanoparticles for efficient visible light photocatalysts. J. Mater. Chem. A **2**, 4429–4437 (2014). https://doi.org/10.1039/c3ta14484d
141. Zhao, Z., Tan, H., Zhao, H., et al.: Reduced TiO_2 rutile nanorods with well-defined facets and their visible-light photocatalytic activity. Chem. Commun. **50**, 2755–2757 (2014). https://doi.org/10.1039/c3cc49182j
142. Pei, Z., Ding, L., Lin, H., et al.: Facile synthesis of defect-mediated TiO_{2-x} with enhanced visible light photocatalytic activity. J. Mater. Chem. A **1**, 10099–10102 (2013). https://doi.org/10.1039/c3ta12062g
143. Dong, S., Wang, X., Shen, L., et al.: Trivalent Ti self-doped $Li_4Ti_5O_{12}$: a high performance anode material for lithium-ion capacitors. J. Electroanal. Chem. **757**, 1–7 (2015). https://doi.org/10.1016/j.jelechem.2015.09.002
144. Schaub, R., Wahlström, E., Rønnau, A., et al.: Oxygen-mediated diffusion of oxygen vacancies on the TiO_2 (110) surface. Science **299**, 377–379 (2003). https://doi.org/10.1126/science.1078962
145. Choudhury, B., Choudhury, A.: Luminescence characteristics of cobalt doped TiO_2 nanoparticles. J. Lumin. **132**, 178–184 (2012). https://doi.org/10.1016/j.jlumin.2011.08.020
146. Yun, H.J., Lee, D.M., Yu, S., et al.: Effect of valence band energy on the photocatalytic performance of N-doped TiO_2 for the production of O_2 via the oxidation of water by visible light. J. Mol. Catal. A: Chem. **378**, 221–226 (2013). https://doi.org/10.1016/j.molcata.2013.06.016
147. Sarkar, A., Khan, G.G., Chaudhuri, A., et al.: Multifunctional $BiFeO_3/TiO_2$ nano-heterostructure: photo-ferroelectricity, rectifying transport, and nonvolatile resistive switching property. Appl. Phys. Lett. **108**, 033112 (2016). https://doi.org/10.1063/1.4940118
148. Samsudin, E.M., Hamid, S.B.A., Juan, J.C., et al.: Effective role of trifluoroacetic acid (TFA) to enhance the photocatalytic activity of F-doped TiO_2 prepared by modified sol–gel method. Appl. Surf. Sci. **365**, 57–68 (2016). https://doi.org/10.1016/j.apsusc.2016.01.016
149. Shrivastava, B.D.: X-ray absorption fine structure (XAFS) spectroscopy using synchrotron radiation. J. Phys: Conf. Ser. **365**, 012002 (2012). https://doi.org/10.1088/1742-6596/365/1/012002
150. Yamashita, H., Ichihashi, Y., Anpo, M., et al.: Photocatalytic decomposition of NO at 275 K on titanium oxides included within y-zeolite cavities: the structure and role of the active sites. J. Phys. Chem. **100**, 16041–16044 (1996). https://doi.org/10.1021/jp9615969
151. Chen, L.X., Rajh, T., Jager, W., et al.: X-ray absorption reveals surface structure of titanium dioxide nanoparticles. J. Synchrotron Radiat. **6**, 445–447 (1999). https://doi.org/10.1107/S090904959801591X
152. Graetz, J., Reilly, J.J., Johnson, J., et al.: X-ray absorption study of Ti-activated sodium aluminum hydride. Appl. Phys. Lett. **85**, 500–502 (2004). https://doi.org/10.1063/1.1773614
153. Wagemaker, M., Lützenkirchen-Hecht, D., Keil, P., et al.: Quasi-in situ reflection mode XANES at the Ti K-edge of lithium intercalated TiO_2 rutile and anatase. Phys. B **336**, 118–123 (2003). https://doi.org/10.1016/S0921-4526(03)00279-5
154. Liu, Z.F., Davis, R.J.: Investigation of the structure of microporous Ti–Si mixed oxides by X-Ray, Uv reflectance, Ft-Raman, and Ft-Ir spectroscopies. J. Phys. Chem. **98**, 1253–1261 (1994). https://doi.org/10.1021/j100055a035
155. Song, H., Jeong, T.G., Moon, Y.H., et al.: Stabilization of oxygen-deficient structure for conducting $Li_4Ti_5O_{12}$-delta by molybdenum doping in a reducing atmosphere. Sci. Rep. **4**, 4350 (2014). https://doi.org/10.1038/srep04350
156. Konno, H.: Chapter 8—X-ray photoelectron spectroscopy. In: Inagaki, M., Kang, F. (eds.) Materials Science and Engineering of Carbon, pp. 153–171. Butterworth-Heinemann, Oxford (2016)

157. Kang, Q., Cao, J., Zhang, Y., et al.: Reduced TiO_2 nanotube arrays for photoelectrochemical water splitting. J. Mater. Chem. A **1**, 5766–5774 (2013). https://doi.org/10.1039/C3TA10689F
158. Guo, Q., Cheng, X., Shi, Y., et al.: Bluish $Li_4Ti_5O_{12}$ with enhanced rate performance. J. Alloys Compd. **710**, 383–392 (2017). https://doi.org/10.1016/j.jallcom.2017.03.296
159. Wu, W.Y., Chang, Y.M., Ting, J.M.: Room-temperature synthesis of single-crystalline anatase TiO_2 nanowires. Cryst. Growth Des. **10**, 1646–1651 (2010). https://doi.org/10.1021/cg901210c
160. Ferraro, J.R., Nakamoto, K., Brown, C.W.: Chapter 1—basic theory. In: Ferraro, J.R., Nakamoto, K., Brown, C.W. (eds.) Introductory Raman spectroscopy, 2nd edn, pp. 1–94. Academic Press, San Diego (2003)
161. Zhang, X.Q., Chen, J.B., Wang, C.W., et al.: Low-temperature liquid phase reduced TiO_2 nanotube arrays: synergy of morphology manipulation and oxygen vacancy doping for enhancement of field emission. Nanotechnology **26**, 175705 (2015). https://doi.org/10.1088/0957-4484/26/17/175705
162. Yi, T.F., Jiang, L.J., Liu, J., et al.: Structure and physical properties of $Li_4Ti_5O_{12}$ synthesized at deoxidization atmosphere. Ionics **17**, 799–803 (2011). https://doi.org/10.1007/s11581-011-0581-z
163. Parker, J.C., Siegel, R.W.: Calibration of the Raman spectrum to the oxygen stoichiometry of nanophase TiO_2. Appl. Phys. Lett. **57**, 943–945 (1990). https://doi.org/10.1063/1.104274
164. Zhang, W.F., He, Y.L., Zhang, M.S., et al.: Raman scattering study on anatase TiO_2 nanocrystals. J. Phys. D Appl. Phys. **33**, 912–916 (2000). https://doi.org/10.1088/0022-3727/33/8/305
165. Choudhury, B., Dey, M., Choudhury, A.: Defect generation, d-d transition, and band gap reduction in Cu-doped TiO_2 nanoparticles. Int. Nano Lett. **3**, 25 (2013). https://doi.org/10.1186/2228-5326-3-25
166. Sarkar, A., Karmakar, K., Khan, G.G.: Designing Co–Pi modified one-dimensional N–P TiO_2/$ZnCo_2O_4$ nanoheterostructure photoanode with reduced electron–hole pair recombination and excellent photoconversion efficiency ($>3\%$). J. Phys. Chem. C **121**, 25705–25717 (2017). https://doi.org/10.1021/acs.jpcc.7b08213
167. Wajid Shah, M., Zhu, Y., Fan, X., et al.: Facile synthesis of defective TiO_{2-x} nanocrystals with high surface area and tailoring bandgap for visible-light photocatalysis. Sci. Rep. **5**, 15804 (2015). https://doi.org/10.1038/srep15804
168. McDevitt, N.T., Baun, W.L.: Infrared absorption study of metal oxides in the low frequency region (700–240 cm^{-1}). Spectrochim. Acta **20**, 799–808 (1964). https://doi.org/10.1016/0371-1951(64)80079-5
169. Wang, P., Qi, C., Wen, P., et al.: Synthesis of Si, N co-doped nano-sized TiO_2 with high thermal stability and photocatalytic activity by mechanochemical method. Nanomaterials (2018). https://doi.org/10.3390/nano8050294
170. Benjwal, P., Kar, K.K.: Removal of methylene blue from wastewater under a low power irradiation source by Zn, Mn co-doped TiO_2 photocatalysts. RSC Adv. **5**, 98166–98176 (2015). https://doi.org/10.1039/C5RA19353B
171. Yu, D., Goh, K., Wang, H., et al.: Scalable synthesis of hierarchically structured carbon nanotube–graphene fibres for capacitive energy storage. Nat. Nanotechnol. **9**, 555 (2014). https://doi.org/10.1038/NNANO.2014.93
172. Li, J., Zhang, M., Guan, Z., et al.: Synergistic effect of surface and bulk single-electron-trapped oxygen vacancy of TiO_2 in the photocatalytic reduction of CO_2. Appl. Catal. B **206**, 300–307 (2017). https://doi.org/10.1016/j.apcatb.2017.01.025
173. Sun, Y., Egawa, T., Shao, C., et al.: Quantitative study of F center in high-surface-area anatase titania nanoparticles prepared by MOCVD. J. Phys. Chem. Solids **65**, 1793–1797 (2004). https://doi.org/10.1016/j.jpcs.2004.05.006
174. Guo, Y., Chen, S., Yu, Y., et al.: Hydrogen-location-sensitive modulation of the redox reactivity for oxygen-deficient TiO_2. J. Am. Chem. Soc. (2019). https://doi.org/10.1021/jacs.9b01836
175. Meng, W.-W., Yan, B.-L., Xu, Y.-J.: A facile electrochemical modification route in molten salt for Ti^{3+} self-doped spinel lithium titanate. Electrochim. Acta **279**, 128–135 (2018). https://doi.org/10.1016/j.electacta.2018.05.070
176. Liu, H., Ma, H.T., Li, X.Z., et al.: The enhancement of TiO_2 photocatalytic activity by hydrogen thermal treatment. Chemosphere **50**, 39–46 (2003). https://doi.org/10.1016/S0045-6535(02)00486-1
177. Kaftelen, H., Tuncer, M., Tu, S., et al.: Mn-substituted spinel $Li_4Ti_5O_{12}$ materials studied by multifrequency EPR spectroscopy. J. Mater. Chem. A **1**, 9973–9982 (2013). https://doi.org/10.1039/C3TA11590A
178. Yoshida, K., Kawai, T., Nambara, T., et al.: Direct observation of oxygen atoms in rutile titanium dioxide by spherical aberration corrected high-resolution transmission electron microscopy. Nanotechnology **17**, 3944–3950 (2006). https://doi.org/10.1088/0957-4484/17/15/056
179. Lu, X., Zhao, L., He, X., et al.: Lithium storage in $Li_4Ti_5O_{12}$ spinel: the full static picture from electron microscopy. Adv. Mater. **24**, 3233–3238 (2012). https://doi.org/10.1002/adma.201200450
180. Gomathi Devi, L., Narasimha Murthy, B.: Characterization of Mo Doped TiO_2 and its enhanced photo catalytic activity under visible light. Catal. Lett. **125**, 320–330 (2008). https://doi.org/10.1007/s10562-008-9568-4
181. Ho, W., Yu, J.C., Lee, S.: Synthesis of hierarchical nanoporous F-doped TiO_2 spheres with visible light photocatalytic activity. Chem. Commun. **10**, 1115–1117 (2006). https://doi.org/10.1039/B515513D
182. Samsudin, E.M., Abd Hamid, S.B., Juan, J.C., et al.: Controlled nitrogen insertion in titanium dioxide for optimal photocatalytic degradation of atrazine. RSC Adv. **5**, 44041–44052 (2015). https://doi.org/10.1039/C5RA00890E
183. Lü, X., Chen, A., Luo, Y., et al.: Conducting Interface in oxide homojunction: understanding of superior properties in black TiO_2. Nano Lett. **16**, 5751–5755 (2016). https://doi.org/10.1021/acs.nanolett.6b02454
184. Muller, D.A., Nakagawa, N., Ohtomo, A., et al.: Atomic-scale imaging of nanoengineered oxygen vacancy profiles in $SrTiO_3$. Nature **430**, 657–661 (2004). https://doi.org/10.1038/nature02756
185. Nakagawa, N., Hwang, H.Y., Muller, D.A.: Why some interfaces cannot be sharp. Nat. Mater. **5**, 204–209 (2006). https://doi.org/10.1038/nmat1569
186. Widmaier, M., Pfeifer, K., Bommer, L., et al.: Valence-tuned lithium titanate nanopowder for high-rate electrochemical energy storage. Batter. Supercaps **1**, 11–26 (2018). https://doi.org/10.1002/batt.201700007
187. Hugenschmidt, M.B., Gamble, L., Campbell, C.T.: The interaction of H_2O with a TiO_2(110) surface. Surf. Sci. **302**, 329–340 (1994). https://doi.org/10.1016/0039-6028(94)90837-0
188. Henderson, M.A.: Evidence for bicarbonate formation on vacuum annealed TiO_2(110) resulting from a precursor-mediated interaction between CO_2 and H_2O. Surf. Sci. **400**, 203–219 (1998). https://doi.org/10.1016/S0039-6028(97)00863-7
189. Besselmann, S., Freitag, C., Hinrichsen, O., et al.: Temperature-programmed reduction and oxidation experiments with V_2O_5/TiO_2 catalysts. Phys. Chem. Chem. Phys. **3**, 4633–4638 (2001). https://doi.org/10.1039/B105466J
190. Setvin, M., Hulva, J., Parkinson, G.S., et al.: Electron transfer between anatase TiO_2 and an O_2 molecule directly observed by atomic force microscopy. Proc. Natl. Acad. Sci. USA **114**, E2556–E2562 (2017). https://doi.org/10.1073/pnas.1618723114

191. Ma, Y., Wang, X., Jia, Y., et al.: Titanium dioxide-based nanomaterials for photocatalytic fuel generations. Chem. Rev. **114**, 9987–10043 (2014). https://doi.org/10.1021/cr500008u
192. Huang, S.Y., Kavan, L., Exnar, I., et al.: Rocking chair lithium battery based on nanocrystalline TiO_2 (anatase). J. Electrochem. Soc. **142**, L142–L144 (1995). https://doi.org/10.1149/1.2048726
193. Jiang, C., Wei, M., Qi, Z., et al.: Particle size dependence of the lithium storage capability and high rate performance of nanocrystalline anatase TiO_2 electrode. J. Power Sources **166**, 239–243 (2007). https://doi.org/10.1016/j.jpowsour.2007.01.004
194. Yang, Z.G., Choi, D., Kerisit, S., et al.: Nanostructures and lithium electrochemical reactivity of lithium titanites and titanium oxides: a review. J. Power Sources **192**, 588–598 (2009). https://doi.org/10.1016/j.jpowsour.2009.02.038
195. Deng, D., Kim, M.G., Lee, J.Y., et al.: Green energy storage materials: nanostructured TiO_2 and Sn-based anodes for lithium-ion batteries. Energy Environ. Sci. **2**, 818–837 (2009). https://doi.org/10.1039/B823474D
196. Dawson, J.A., Robertson, J.: Improved calculation of Li and Na intercalation properties in anatase, rutile, and TiO_2(B). J. Phys. Chem. C **120**, 22910–22917 (2016). https://doi.org/10.1021/acs.jpcc.6b08842
197. Tsai, P.-C., Hsu, W.-D., Lin, S.-K.: Atomistic structure and Ab initio electrochemical properties of $Li_4Ti_5O_{12}$ defect spinel for Li ion batteries. J. Electrochem. Soc. **161**, A439–A444 (2014). https://doi.org/10.1149/2.095403jes
198. Ohzuku, T., Ueda, A., Yamamoto, N.: Zero-strain insertion material of $Li[Li_{1/3}Ti_{5/3}]O_4$ for rechargeable lithium cells. J. Electrochem. Soc. **142**, 1431–1435 (1995). https://doi.org/10.1149/1.2048592
199. Kostlánová, T., Dědeček, J., Krtil, P.: The effect of the inner particle structure on the electronic structure of the nano-crystalline Li–Ti–O spinels. Electrochim. Acta **52**, 1847–1856 (2007). https://doi.org/10.1016/j.electacta.2006.07.048
200. Jhan, Y.R., Duh, J.G.: Electrochemical performance and low discharge cut-off voltage behavior of ruthenium doped $Li_4Ti_5O_{12}$ with improved energy density. Electrochim. Acta **63**, 9–15 (2012). https://doi.org/10.1016/j.electacta.2011.12.014
201. Kim, C., Norberg, N.S., Alexander, C.T., et al.: Mechanism of phase propagation during lithiation in carbon-free $Li_4Ti_5O_{12}$ battery electrodes. Adv. Funct. Mater. **23**, 1214–1222 (2013). https://doi.org/10.1002/adfm.201201684
202. Asahi, R., Taga, Y., Mannstadt, W., et al.: Electronic and optical properties of anatase TiO_2. Phys. Rev. B **61**, 7459–7465 (2000). https://doi.org/10.1103/PhysRevB.61.7459
203. Yeh, H.L., Tai, S.H., Hsieh, C.M., et al.: First-principles study of lithium intercalation and diffusion in oxygen-defective titanium dioxide. J. Phys. Chem. C **122**, 19447–19454 (2018). https://doi.org/10.1021/acs.jpcc.8b06540
204. Scanlon, D.O., Dunnill, C.W., Buckeridge, J., et al.: Band alignment of rutile and anatase TiO_2. Nat. Mater. **12**, 798–801 (2013). https://doi.org/10.1038/nmat3697
205. Burdett, J.K., Hughbanks, T., Miller, G.J., et al.: Structural-electronic relationships in inorganic solids: powder neutron diffraction studies of the rutile and anatase polymorphs of titanium dioxide at 15 and 295 K. J. Am. Chem. Soc. **109**, 3639–3646 (1987). https://doi.org/10.1021/ja00246a021
206. Shi, L.-B., Wang, Y.P.: A study on native defects and magnetic properties in undoped rutile TiO_2 using LDA and LDA + U_{Op} + U_{Tid} methods. J. Magn. Magn. Mater. **405**, 1–8 (2016). https://doi.org/10.1016/j.jmmm.2015.12.045
207. Morgan, B.J., Madden, P.A.: Lithium intercalation into TiO_2(B): a comparison of LDA, GGA, and GGA + Udensity functional calculations. Phys. Rev. B **86**, 035147 (2012). https://doi.org/10.1103/PhysRevB.86.035147
208. D'Elia, D.: Elaboration and study of TiO_2 nanostructures for hydrogen generation via photolysis of water. École Nationale Supérieure des Mines de Paris (2011)
209. Feist, T.P., Davies, P.K.: The soft chemical synthesis of TiO_2 (B) from layered titanates. J. Solid State Chem. **101**, 275–295 (1992). https://doi.org/10.1016/0022-4596(92)90184-W
210. Ouyang, C.Y., Zhong, Z.Y., Lei, M.S.: Ab initio studies of structural and electronic properties of $Li_4Ti_5O_{12}$ spinel. Electrochem. Commun. **9**, 1107–1112 (2007). https://doi.org/10.1016/j.elecom.2007.01.013
211. Kellerman, D.G., Mukhina, N.A., Zhuravlev, N.A., et al.: Optical absorption and nuclear magnetic resonance in lithium titanium spinel doped by chromium. Phys. Solid State **52**, 459–464 (2010). https://doi.org/10.1134/s1063783410030030
212. Raja, M.W., Mahanty, S., Kundu, M., et al.: Synthesis of nanocrystalline $Li_4Ti_5O_{12}$ by a novel aqueous combustion technique. J. Alloys Compd. **468**, 258–262 (2009). https://doi.org/10.1016/j.jallcom.2007.12.072
213. Scharner, S., Weppner, W., Schmid-Beurmann, P.: Evidence of two-phase formation upon lithium insertion into the $Li_{1.33}Ti_{1.67}O_4$ spinel. J. Electrochem. Soc. **146**, 857–861 (1999). https://doi.org/10.1149/1.1391692
214. Wagemaker, M., Borghols, W.J.H., Mulder, F.M.: Large impact of particle size on insertion reactions. A case for anatase Li_xTiO_2. J. Am. Chem. Soc. **129**, 4323–4327 (2007). https://doi.org/10.1021/ja067733p
215. Armstrong, A.R., Armstrong, G., Canales, J., et al.: Lithium-ion intercalation into TiO_2-B nanowires. Adv. Mater. **17**, 862–865 (2005). https://doi.org/10.1002/adma.200400795
216. Shin, J.-Y., Samuelis, D., Maier, J.: Sustained lithium-storage performance of hierarchical, nanoporous anatase TiO_2 at high rates: emphasis on interfacial storage phenomena. Adv. Funct. Mater. **21**, 3464–3472 (2011). https://doi.org/10.1002/adfm.201002527
217. Rahman, M.A., Wang, X., Wen, C.: Enhanced electrochemical performance of Li-ion batteries with nanoporous titania as negative electrodes. J. Energy Chem. **24**, 157–170 (2015). https://doi.org/10.1016/S2095-4956(15)60296-0
218. Dambournet, D., Belharouak, I., Amine, K.: Tailored preparation methods of TiO_2 anatase, Rutile, Brookite: mechanism of formation and electrochemical properties. Chem. Mater. **22**, 1173–1179 (2010). https://doi.org/10.1021/cm902613h
219. Shin, J.Y., Joo, J.H., Samuelis, D., et al.: Oxygen-deficient $TiO_{2-\delta}$ nanoparticles via hydrogen reduction for high rate capability lithium batteries. Chem. Mater. **24**, 543–551 (2012). https://doi.org/10.1021/cm2031009
220. Song, H., Yun, S.W., Chun, H.H., et al.: Anomalous decrease in structural disorder due to charge redistribution in Cr-doped $Li_4Ti_5O_{12}$ negative-electrode materials for high-rate Li-ion batteries. Energy Environ. Sci. **5**, 9903–9913 (2012). https://doi.org/10.1039/C2EE22734G
221. Lu, Z., Yip, C.T., Wang, L., et al.: Hydrogenated TiO_2 nanotube arrays as high-rate anodes for lithium-ion microbatteries. ChemPlusChem **77**, 991–1000 (2012). https://doi.org/10.1002/cplu.201200104
222. Ventosa, E., Tymoczko, A., Xie, K., et al.: Low temperature hydrogen reduction of high surface area anatase and anatase/β-TiO_2 for high-charging-rate batteries. Chemsuschem **7**, 2584–2589 (2014). https://doi.org/10.1002/cssc.201402279
223. Zhang, Z., Zhou, Z., Nie, S., et al.: Flower-like hydrogenated TiO_2(B) nanostructures as anode materials for high-performance lithium ion batteries. J. Power Sources **267**, 388–393 (2014). https://doi.org/10.1016/j.jpowsour.2014.05.121
224. Zheng, J., Liu, Y., Ji, G., et al.: Hydrogenated oxygen-deficient blue anatase as anode for high-performance lithium batteries. ACS Appl. Mater. Interfaces. **7**, 23431–23438 (2015). https://doi.org/10.1021/acsami.5b07000

225. Kim, J.G., Shi, D., Kong, K.J., et al.: Structurally and electronically designed TiO_2N_x nanofibers for lithium rechargeable batteries. ACS Appl. Mater. Interfaces. **5**, 691–696 (2013). https://doi.org/10.1021/am302197y
226. Tian, H., Xin, F., Tan, X., et al.: High lithium electroactivity of boron-doped hierarchical rutile submicrosphere TiO_2. J. Mater. Chem. A **2**, 10599–10606 (2014). https://doi.org/10.1039/C4TA01438C
227. Cao, M., Tao, L., Lv, X., et al.: Phosphorus-doped TiO_2-B nanowire arrays boosting robust pseudocapacitive properties for lithium storage. J. Power Sources **396**, 327–334 (2018). https://doi.org/10.1016/j.jpowsour.2018.06.012
228. Finazzi, E., Di Valentin, C., Pacchioni, G., et al.: Excess electron states in reduced bulk anatase TiO_2: comparison of standard GGA, GGA + U, and hybrid DFT calculations. J. Chem. Phys. **129**, 154113 (2008). https://doi.org/10.1063/1.2996362
229. Kong, L.M., Zhu, B.L., Pang, X.Y., et al.: First-principles study on TiO_2-B with oxygen vacancies as a negative material of rechargeable lithium-ion batteries. Acta Phys. Chim. Sin. **32**, 656–664 (2016). https://doi.org/10.3866/pku.whxb201512292
230. Zhang, Y., Ding, Z.Y., Foster, C.W., et al.: Oxygen vacancies evoked blue TiO_2(B) nanobelts with efficiency enhancement in sodium storage behaviors. Adv. Funct. Mater. (2017). https://doi.org/10.1002/adfm.201700856
231. Dalton, A.S., Belak, A.A., Van der Ven, A.: Thermodynamics of lithium in TiO_2(B) from first principles. Chem. Mater. **24**, 1568–1574 (2012). https://doi.org/10.1021/cm203283v
232. Arrouvel, C., Parker, S.C., Islam, M.S.: Lithium insertion and transport in the TiO_2-B anode material: a computational study. Chem. Mater. **21**, 4778–4783 (2009). https://doi.org/10.1021/cm900373u
233. Zhang, Y.F., Lin, W., Li, Y., et al.: A theoretical study on the electronic structures of TiO_2: effect of hartree–fock exchange. J. Phys. Chem. B **109**, 19270–19277 (2005). https://doi.org/10.1021/jp0523625
234. Yuan, T., Cai, R., Shao, Z.P.: Different effect of the atmospheres on the phase formation and performance of $Li_4Ti_5O_{12}$ prepared from ball-milling-assisted solid-phase reaction with pristine and carbon-precoated TiO_2 as starting materials. J. Phys. Chem. C **115**, 4943–4952 (2011). https://doi.org/10.1021/jp111353e
235. Samin, A., Kurth, M., Cao, L.: Ab initio study of radiation effects on the $Li_4Ti_5O_{12}$ electrode used in lithium-ion batteries. AIP Adv. (2015). https://doi.org/10.1063/1.4917308
236. Morgan, B.J., Watson, G.W.: GGA + U description of lithium intercalation into anatase TiO_2. Phys. Rev. B **82**, 144119 (2010). https://doi.org/10.1103/PhysRevB.82.144119
237. Spreafico, C., VandeVondele, J.: Excess electrons and interstitial Li atoms in TiO_2 anatase: properties of the (101) interface. J. Phys. Chem. C **119**, 15009–15018 (2015). https://doi.org/10.1021/acs.jpcc.5b04103
238. Södergren, S., Siegbahn, H., Rensmo, H., et al.: Lithium intercalation in nanoporous anatase TiO_2 studied with XPS. J. Phys. Chem. B **101**, 3087–3090 (1997). https://doi.org/10.1021/jp9639399
239. Augustsson, A., Henningsson, A., Butorin, S.M., et al.: Lithium ion insertion in nanoporous anatase TiO_2 studied with RIXS. J. Chem. Phys. **119**, 3983–3987 (2003). https://doi.org/10.1063/1.1591735
240. Henningsson, A., Rensmo, H., Sandell, A., et al.: Electronic structure of electrochemically Li-inserted TiO_2 studied with synchrotron radiation electron spectroscopies. J. Chem. Phys. **118**, 5607–5612 (2003). https://doi.org/10.1063/1.1545086
241. Richter, J.H., Henningsson, A., Karlsson, P.G., et al.: Electronic structure of lithium-doped anatase TiO_2 prepared in ultrahigh vacuum. Phys. Rev. B **71**, 235418 (2005). https://doi.org/10.1103/PhysRevB.71.235418
242. Brant, A.T., Giles, N.C., Halliburton, L.E.: Insertion of lithium ions into TiO_2 (rutile) crystals: an electron paramagnetic resonance study of the Li-associated Ti^{3+} small polaron. J. Appl. Phys. **113**, 053712 (2013). https://doi.org/10.1063/1.4790366
243. Koudriachova, M.V., Harrison, N.M., de Leeuw, S.W., et al.: Density-functional simulations of lithium intercalation in rutile. Phys. Rev. B **65**, 235423 (2002). https://doi.org/10.1103/physrevb.65.235423
244. Legrain, F., Malyi, O., Manzhos, S.: Insertion energetics of lithium, sodium, and magnesium in crystalline and amorphous titanium dioxide: a comparative first-principles study. J. Power Sources **278**, 197–202 (2015). https://doi.org/10.1016/j.jpowsour.2014.12.058
245. Liu, D.T., Ouyang, C.Y., Shu, J., et al.: Theoretical study of cation doping effect on the electronic conductivity of $Li_4Ti_5O_{12}$. Phys. Status Solidi B Basic Solid State Phys. **243**, 1835–1841 (2006). https://doi.org/10.1002/pssb.200541404
246. Zhong, Z., Ouyang, C., Shi, S., et al.: Ab initio studies on $Li_{4+x}Ti_5O_{12}$ compounds as anode materials for lithium-ion batteries. ChemPhysChem **9**, 2104–2108 (2008). https://doi.org/10.1002/cphc.200800333
247. Das, S.K., Gnanavel, M., Patel, M.U.M., et al.: Anamolously high lithium storage in mesoporous nanoparticulate aggregation of Fe^{3+} doped anatase titania. J. Electrochem. Soc. **158**, A1290–A1297 (2011). https://doi.org/10.1149/2.029112jes
248. Grosjean, R., Fehse, M., Pigeot-Remy, S., et al.: Facile synthetic route towards nanostructured Fe–TiO_2 (B), used as negative electrode for Li-ion batteries. J. Power Sources **278**, 1–8 (2015). https://doi.org/10.1016/j.jpowsour.2014.12.032
249. Zhang, W., Gong, Y., Mellott, N.P., et al.: Synthesis of nickel doped anatase titanate as high performance anode materials for lithium ion batteries. J. Power Sources **276**, 39–45 (2015). https://doi.org/10.1016/j.jpowsour.2014.11.098
250. Luebke, M., Shin, J., Marchand, P., et al.: Highly pseudocapacitive Nb-doped TiO_2 high power anodes for lithium-ion batteries. J. Mater. Chem. A **3**, 22908–22914 (2015). https://doi.org/10.1039/c5ta07554h
251. Thi, T.V., Rai, A.K., Gim, J., et al.: Effect of Mo^{6+} doping on electrochemical performance of anatase TiO_2 as a high performance anode material for secondary lithium-ion batteries. J. Alloys Compd. **598**, 16–22 (2014). https://doi.org/10.1016/j.jallcom.2014.02.019
252. Wang, Y., Xu, M., Peng, Z., et al.: Direct growth of mesoporous Sn-doped TiO_2 thin films on conducting substrates for lithium-ion battery anodes. J. Mater. Chem. A **1**, 13222–13226 (2013). https://doi.org/10.1039/c3ta13198j
253. Wang, H., Xi, L., Tucek, J., et al.: Synthesis and characterization of tin titanate nanotubes: precursors for nanoparticulate Sn-doped TiO_2 anodes with synergistically improved electrochemical performance. Chemelectrochem **1**, 1563–1569 (2014). https://doi.org/10.1002/celc.201402188
254. Jung, H.G., Yoon, C.S., Prakash, J., et al.: Mesoporous anatase TiO_2 with high surface area and controllable pore size by F-Ion doping: applications for high-power Li-Ion battery anode. J. Phys. Chem. C **113**, 21258–21263 (2009). https://doi.org/10.1021/jp908719k
255. Goriparti, S., Miele, E., Prato, M., et al.: Direct synthesis of carbon-doped TiO_2-bronze nanowires as anode materials for high performance lithium-ion batteries. ACS Appl. Mater. Interfaces. **7**, 25139–25146 (2015). https://doi.org/10.1021/acsami.5b06426
256. Xiao, Y., Hu, C., Cao, M.: Compositing amorphous TiO_2 with N-doped carbon as high-rate anode materials for lithium-ion batteries. Chem. Asian J. **9**, 351–356 (2014). https://doi.org/10.1002/asia.201301183

257. Yang, Y., Ji, X., Jing, M., et al.: Carbon dots supported upon N-doped TiO_2 nanorods applied into sodium and lithium ion batteries. J. Mater. Chem. A **3**, 5648–5655 (2015). https://doi.org/10.1039/c4ta05611f
258. Zhang, Y., Fu, Q., Xu, Q., et al.: Improved electrochemical performance of nitrogen doped TiO_2-B nanowires as anode materials for Li-ion batteries. Nanoscale **7**, 12215–12224 (2015). https://doi.org/10.1039/c5nr02457a
259. Chen, C., Zhang, B., Miao, L., et al.: Binding TiO_2-B nanosheets with N-doped carbon enables highly durable anodes for lithium-ion batteries. J. Mater. Chem. A **4**, 8172–8179 (2016). https://doi.org/10.1039/c6ta01955b
260. Lai, C., Yuan, X.C., Cao, X.L., et al.: Enhanced high-rate capability of the C-N-doped TiO_2 as anode material for lithium-ion battery. Electrochem. Solid State Lett. **15**, A65–A67 (2012). https://doi.org/10.1149/2.023205esl
261. Gao, Y., Wang, C., Hu, P., et al.: Carbon-incorporated, nitrogen-doped branch-like TiO_2 nanostructure towards superior lithium storage performance. J. Alloys Compd. **787**, 944–951 (2019). https://doi.org/10.1016/j.jallcom.2019.02.169
262. Bi, Z., Paranthaman, M.P., Guo, B., et al.: High performance Cr, N-codoped mesoporous TiO_2 microspheres for lithium-ion batteries. J. Mater. Chem. A **2**, 1818–1824 (2014). https://doi.org/10.1039/c3ta14535b
263. Kumar, V.S.P., Deshpande, P.A.: DFT reveals concentration-dependent cathodic/anodic behaviour of lithiated titania. Mater. Res. Express (2018). https://doi.org/10.1088/2053-1591/aad5bc
264. Liu, X.D., Jiang, E.Y., Li, Z.Q., et al.: Electronic structure and optical properties of Nb-doped anatase TiO_2. Appl. Phys. Lett. (2008). https://doi.org/10.1063/1.2949070
265. Peng, H.W., Li, J.B., Li, S.S., et al.: First-principles study of the electronic structures and magnetic properties of 3d transition metal-doped anatase TiO_2. J. Phys. Condens. Matter (2008). https://doi.org/10.1088/0953-8984/20/12/125207
266. Shirley, R., Kraft, M., Inderwildi, O.R.: Electronic and optical properties of aluminium-doped anatase and rutile TiO_2 from ab initio calculations. Phys. Rev. B (2010). https://doi.org/10.1103/physrevb.81.075111
267. Yu, Q.H., Jin, L., Zhou, C.G.: Ab initio study of electronic structures and absorption properties of pure and Fe^{3+} doped anatase TiO_2. Sol. Energy Mater. Sol. Cells **95**, 2322–2326 (2011). https://doi.org/10.1016/j.solmat.2011.03.048
268. Zhang, R.S., Liu, Y., Gao, Q., et al.: First-principles study on the electronic and optical properties of F- and Nb-doped anatase TiO_2. J. Alloys Compd. **509**, 9178–9182 (2011). https://doi.org/10.1016/j.jallcom.2011.06.105
269. Li, C., Zhao, Y.F., Gong, Y.Y., et al.: Band gap engineering of early transition-metal-doped anatase TiO(2): first principles calculations. Phys. Chem. Chem. Phys. **16**, 21446–21451 (2014). https://doi.org/10.1039/c4cp03587a
270. Han, Y.X., Yang, C.L., Wang, M.S., et al.: Enhancing the visible-light absorption of TiO_2 with the use of key N Co, and Na dopant concentrations. Sol. Energy Mater. Sol. Cells **132**, 94–100 (2015). https://doi.org/10.1016/j.solmat.2014.08.027
271. Pan, J.W., Li, C., Zhao, Y.F., et al.: Electronic properties of TiO_2 doped with Sc, Y, La, Zr, Hf, V, Nb and Ta. Chem. Phys. Lett. **628**, 43–48 (2015). https://doi.org/10.1016/j.cplett.2015.03.056
272. Yang, X.Y., Min, Y.X., Li, S.B., et al.: Conductive Nb-doped TiO_2 thin films with whole visible absorption to degrade pollutants. Catal. Sci. Technol. **8**, 1357–1365 (2018). https://doi.org/10.1039/c7cy02614e
273. Yu, Z.J., Zhang, X.F., Yang, G.L., et al.: High rate capability and long-term cyclability of $Li_4Ti_{4.9}V_{0.1}O_{12}$ as anode material in lithium ion battery. Electrochim. Acta **56**, 8611–8617 (2011). https://doi.org/10.1016/j.electacta.2011.07.051
274. Hao, Y.J., Lai, Q.Y., Lu, J.Z., et al.: Effects of dopant on the electrochemical properties of $Li_4Ti_5O_{12}$ anode materials. Ionics **13**, 369–373 (2007). https://doi.org/10.1007/s11581-007-0111-1
275. Li, X., Qu, M.Z., Yu, Z.L.: Structural and electrochemical performances of $Li_4Ti_{5-x}Zr_xO_{12}$ as anode material for lithium-ion batteries. J. Alloys Compd. **487**, L12–L17 (2009). https://doi.org/10.1016/j.jallcom.2009.07.176
276. Kim, J.G., Park, M.S., Hwang, S.M., et al.: Zr^{4+} doping in $Li_4Ti_5O_{12}$ anode for lithium-ion batteries: open Li^+ diffusion paths through structural imperfection. Chemsuschem **7**, 1451–1457 (2014). https://doi.org/10.1002/cssc.201301393
277. Tian, B.B., Xiang, H.F., Zhang, L., et al.: Niobium doped lithium titanate as a high rate anode material for Li-ion batteries. Electrochim. Acta **55**, 5453–5458 (2010). https://doi.org/10.1016/j.electacta.2010.04.068
278. Zhong, Z.: Synthesis of Mo^{4+} substituted spinel $Li_4Ti_{5-x}Mo_xO_{12}$. Electrochem. Solid-State Lett. **10**, A267–A269 (2007). https://doi.org/10.1149/1.2784142
279. Jhan, Y.R., Lin, C.Y., Duh, J.G.: Preparation and characterization of ruthenium doped $Li_4Ti_5O_{12}$ anode material for the enhancement of rate capability and cyclic stability. Mater. Lett. **65**, 2502–2505 (2011). https://doi.org/10.1016/j.matlet.2011.04.060
280. Zhang, Q.Y., Verde, M.G., Seo, J.K., et al.: Structural and electrochemical properties of Gd-doped $Li_4Ti_5O_{12}$ as anode material with improved rate capability for lithium-ion batteries. J. Power Sources **280**, 355–362 (2015). https://doi.org/10.1016/j.jpowsour.2015.01.124
281. Song, K., Seo, D.-H., Jo, M.R., et al.: Tailored oxygen framework of $Li_4Ti_5O_{12}$ nanorods for high-power Li ion battery. J. Phys. Chem. Lett. **5**, 1368–1373 (2014). https://doi.org/10.1021/jz5002924
282. Yi, T.F., Yang, S.Y., Li, X.Y., et al.: Sub-micrometric $Li_{4-x}Na_xTi_5O_{12}$ ($0\leqslant x\leqslant=0.2$) spinel as anode material exhibiting high rate capability. J. Power Sources **246**, 505–511 (2014). https://doi.org/10.1016/j.jpowsour.2013.08.005
283. Chen, C.H., Vaughey, J.T., Jansen, A.N., et al.: Studies of Mg-substituted $Li_{4-x}Mg_xTi_5O_{12}$ spinel Electrodes ($0 \leq x \leq 1$) for Lithium Batteries. J. Electrochem. Soc. **148**, A102–A104 (2001). https://doi.org/10.1149/1.1344523
284. Zhang, Q.Y., Zhang, C.L., Li, B., et al.: Preparation and electrochemical properties of Ca-doped $Li_4Ti_5O_{12}$ as anode materials in lithium-ion battery. Electrochim. Acta **98**, 146–152 (2013). https://doi.org/10.1016/j.electacta.2013.03.006
285. Wu, H.B., Chang, S., Liu, X.L., et al.: Sr-doped $Li_4Ti_5O_{12}$ as the anode material for lithium-ion batteries. Solid State Ionics **232**, 13–18 (2013). https://doi.org/10.1016/j.ssi.2012.10.027
286. Du, G.D., Sharma, N., Peterson, V.K., et al.: Br-doped $Li_4Ti_5O_{12}$ and composite TiO_2 anodes for Li-ion batteries: synchrotron *X*-ray and in situ neutron diffraction studies. Adv. Funct. Mater. **21**, 3990–3997 (2011). https://doi.org/10.1002/adfm.201100846
287. Long, W.M., Wang, X.Y., Yang, S.Y., et al.: Electrochemical properties of $Li_4Ti_{5-2x}Ni_xMn_xO_{12}$ compounds synthesized by sol-gel process. Mater. Chem. Phys. **131**, 431–435 (2011). https://doi.org/10.1016/j.matchemphys.2011.09.071
288. Zhang, Q., Lu, H., Zhong, H., et al.: W^{6+} & Br^- codoped $Li_4Ti_5O_{12}$ anode with super rate performance for Li-ion batteries. J. Mater. Chem. A **3**, 13706–13716 (2015). https://doi.org/10.1039/C5TA02784E
289. Huang, S.H., Wen, Z.Y., Gu, Z.H., et al.: Preparation and cycling performance of Al^{3+} and F^- co-substituted compounds $Li_4Al_xTi_{5-x}F_yO_{12-y}$. Electrochim. Acta **50**, 4057–4062 (2005). https://doi.org/10.1016/j.electacta.2004.12.036
290. Liu, Z.X., Sun, L.M., Yang, W.Y., et al.: The synergic effects of Na and K co-doping on the crystal structure and electrochemical properties of $Li_4Ti_5O_{12}$ as anode material for lithium ion battery.

Solid State Sci. **44**, 39–44 (2015). https://doi.org/10.1016/j.solidstatesciences.2015.04.002
291. Duan, H., Li, J., Du, H.D., et al.: Tailoring native defects and zinc impurities in $Li_4Ti_5O_{12}$: insights from first-principles study. J. Phys. Chem. C **119**, 5238–5245 (2015). https://doi.org/10.1021/acs.jpcc.5b00829
292. Yang, Z., Wang, J., Zhang, Q., et al.: Doping the $Li_4Ti_5O_{12}$ lattice with extra-large anions. Mater. Express **5**, 457–462 (2015). https://doi.org/10.1166/mex.2015.1259
293. Cho, H., Son, H., Kim, D., et al.: Impact of Mg-doping site control in the performance of $Li_4Ti_5O_{12}$ Li-ion battery anode: first-principles predictions and experimental verifications. J. Phys. Chem. C **121**, 14994–15001 (2017). https://doi.org/10.1021/acs.jpcc.7b01475
294. Koudriachova, M.V., Harrison, N.M., de Leeuw, S.W.: Effect of diffusion on lithium intercalation in titanium dioxide. Phys. Rev. Lett. **86**, 1275–1278 (2001). https://doi.org/10.1103/PhysRevLett.86.1275
295. Brohan, L., Marchand, R.: Properties physiques des bronzes $MxTiO_2$ (B). Solid State Ionics **9–10**, 419–424 (1983). https://doi.org/10.1016/0167-2738(83)90269-2
296. Armstrong, A.R., Arrouvel, C., Gentili, V., et al.: Lithium coordination sites in Li_xTiO_2(B): a structural and computational study. Chem. Mater. **22**, 6426–6432 (2010). https://doi.org/10.1021/cm102589x
297. Wagemaker, M., Kearley, G.J., van Well, A.A., et al.: Multiple Li positions inside oxygen octahedra in lithiated TiO_2 anatase. J. Am. Chem. Soc. **125**, 840–848 (2003). https://doi.org/10.1021/ja028165q
298. Arrouvel, C., Peixoto, T.C., Valerio, M.E.G., et al.: Lithium migration at low concentration in TiO_2 polymorphs. Comput. Theor. Chem. **1072**, 43–51 (2015). https://doi.org/10.1016/j.comptc.2015.09.002
299. Panduwinata, D., Gale, J.D.: A first principles investigation of lithium intercalation in TiO_2-B. J. Mater. Chem. **19**, 3931–3940 (2009). https://doi.org/10.1039/B902683E
300. Zeng, T., Ji, P., Hu, X., et al.: Nano-Sn doped carbon-coated rutile TiO_2 spheres as a high capacity anode for Li-ion battery. RSC Adv. **6**, 48530–48536 (2016). https://doi.org/10.1039/C6RA04672J
301. Liang, K., Chen, X., Guo, Z., et al.: Lithium intercalation and diffusion in TiO_2 nanotubes: a first-principles investigation. Phys. Chem. Chem. Phys. **18**, 24370–24376 (2016). https://doi.org/10.1039/c6cp03830a
302. Olson, C.L., Nelson, J., Islam, M.S.: Defect chemistry, surface structures, and lithium insertion in anatase TiO_2. J. Phys. Chem. B **110**, 9995–10001 (2006). https://doi.org/10.1021/jp0572611
303. Ziebarth, B., Klinsmann, M., Eckl, T., et al.: Lithium diffusion in the spinel phase $Li_4Ti_5O_{12}$ and in the rocksalt phase $Li_7Ti_5O_{12}$ of lithium titanate from first principles. Phys. Rev. B **89**, 174301–174307 (2014). https://doi.org/10.1103/PhysRevB.89.174301
304. Chen, Y.C., Ouyang, C.Y., Song, L.J., et al.: Lithium ion diffusion in $Li_{4+x}Ti_5O_{12}$: from ab initio studies. Electrochim. Acta **56**, 6084–6088 (2011). https://doi.org/10.1016/j.electacta.2011.04.077
305. Yildirim, H., Greeley, J.P., Sankaranarayanan, S.K.: The effect of concentration on Li diffusivity and conductivity in rutile TiO_2. Phys. Chem. Chem. Phys. **14**, 4565–4576 (2012). https://doi.org/10.1039/c2cp22731b
306. Henkelman, G., Arnaldsson, A., Jonsson, H.: A fast and robust algorithm for Bader decomposition of charge density. Comput. Mater. Sci. **36**, 354–360 (2006). https://doi.org/10.1016/j.commatsci.2005.04.010
307. Sanville, E., Kenny, S.D., Smith, R., et al.: Improved grid-based algorithm for Bader charge allocation. J. Comput. Chem. **28**, 899–908 (2007). https://doi.org/10.1002/jcc.20575
308. Tang, W., Sanville, E., Henkelman, G.: A grid-based Bader analysis algorithm without lattice bias. J. Phys.: Condens. Matter **21**, 084204 (2009). https://doi.org/10.1088/0953-8984/21/8/084204
309. Pazhamalai, P., Krishnamoorthy, K., Mariappan, V.K., et al.: Blue TiO_2 nanosheets as a high-performance electrode material for supercapacitors. J. Colloid Interface Sci. **536**, 62–70 (2019). https://doi.org/10.1016/j.jcis.2018.10.031
310. Armstrong, A.R., Armstrong, G., Canales, J., et al.: TiO(2)-B nanowires. Angew. Chem. Int. Ed. Engl. **43**, 2286–2288 (2004). https://doi.org/10.1002/anie.200353571
311. Pérez-Flores, J.C., Baehtz, C., Kuhn, A., et al.: Hollandite-type TiO_2: a new negative electrode material for sodium-ion batteries. J. Mater. Chem. A **2**, 1825–1833 (2014). https://doi.org/10.1039/c3ta13394j
312. Zhang, M., MacRae, A.C., Liu, H., et al.: Communication–investigation of anatase-TiO_2 as an efficient electrode material for magnesium-ion batteries. J. Electrochem. Soc. **163**, A2368–A2370 (2016). https://doi.org/10.1149/2.1091610jes
313. Saha, P., Datta, M.K., Velikokhatnyi, O.I., et al.: Rechargeable magnesium battery: current status and key challenges for the future. Prog. Mater Sci. **66**, 1–86 (2014). https://doi.org/10.1016/j.pmatsci.2014.04.001
314. Gan, Q., He, H., Zhao, K., et al.: Plasma-induced oxygen vacancies in urchin-like anatase titania coated by carbon for excellent sodium-ion battery anodes. ACS Appl. Mater. Interfaces. **10**, 7031–7042 (2018). https://doi.org/10.1021/acsami.7b13760
315. Chen, X., Liu, L., Huang, F.: Black titanium dioxide (TiO_2) nanomaterials. Chem. Soc. Rev. **44**, 1861–1885 (2015). https://doi.org/10.1039/c4cs00330f
316. Fan, L.Z., Chi, S.S., Wang, L.N., et al.: Synthesis of TiOx nanotubular arrays with oxygen defects as high-performance anodes for lithium-ion batteries. ChemElectroChem **2**, 421–426 (2015). https://doi.org/10.1002/celc.201402331
317. Zhang, J., Wang, Y., Wu, J., et al.: Remarkable supercapacitive performance of TiO_2 nanotube arrays by introduction of oxygen vacancies. Chem. Eng. J. **313**, 1071–1081 (2017). https://doi.org/10.1016/j.cej.2016.11.004
318. Shen, L., Uchaker, E., Zhang, X., et al.: Hydrogenated $Li_4Ti_5O_{12}$ nanowire arrays for high rate lithium ion batteries. Adv. Mater. **24**, 6502–6506 (2012). https://doi.org/10.1002/adma.201203151
319. Deng, X., Wei, Z., Cui, C., et al.: Oxygen-deficient anatase TiO_2@C nanospindles with pseudocapacitive contribution for enhancing lithium storage. J. Mater. Chem. A **6**, 4013–4022 (2018). https://doi.org/10.1039/c7ta11301c
320. Li, W., Corradini, D., Body, M., et al.: High substitution rate in TiO_2 anatase nanoparticles with cationic vacancies for fast lithium storage. Chem. Mater. **27**, 5014–5019 (2015). https://doi.org/10.1021/acs.chemmater.5b01407
321. Ma, Y., Ding, B., Ji, G., et al.: Carbon-encapsulated F-doped $Li_4Ti_5O_{12}$ as a high rate anode material for Li^+ batteries. ACS Nano **7**, 10870–10878 (2013). https://doi.org/10.1021/nn404311x
322. Anh, L.T., Rai, A.K., Thi, T.V., et al.: Improving the electrochemical performance of anatase titanium dioxide by vanadium doping as an anode material for lithium-ion batteries. J. Power Sources **243**, 891–898 (2013). https://doi.org/10.1016/j.jpowsour.2013.06.080
323. Fehse, M., Cavaliere, S., Lippens, P.E., et al.: Nb-doped TiO_2 nanofibers for lithium ion batteries. J. Phys. Chem. C **117**, 13827–13835 (2013). https://doi.org/10.1021/jp402498p
324. Bai, Y.J., Gong, C., Lun, N., et al.: Yttrium-modified $Li_4Ti_5O_{12}$ as an effective anode material for lithium ion batteries with

outstanding long-term cyclability and rate capabilities. J. Mater. Chem. A **1**, 89–96 (2013). https://doi.org/10.1039/C2TA00048B
325. Chen, J., Ding, Z., Wang, C., et al.: Black anatase titania with ultrafast sodium-storage performances stimulated by oxygen vacancies. ACS Appl. Mater. Interfaces. **8**, 9142–9151 (2016). https://doi.org/10.1021/acsami.6b01183
326. Zhao, C., Cai, Y., Yin, K., et al.: Carbon-bonded, oxygen-deficient TiO_2 nanotubes with hybridized phases for superior Na-ion storage. Chem. Eng. J. **350**, 201–208 (2018). https://doi.org/10.1016/j.cej.2018.05.194
327. Xiong, P., Zhang, X., Zhang, F., et al.: Two-dimensional unilamellar cation-deficient metal oxide nanosheet superlattices for high-rate sodium ion energy storage. ACS Nano **12**, 12337–12346 (2018). https://doi.org/10.1021/acsnano.8b06206
328. Zhang, H., Jiang, Y., Qi, Z., et al.: Sulfur doped ultra-thin anatase TiO_2 nanosheets/graphene nanocomposite for high-performance pseudocapacitive sodium storage. Energy Storage Mater. **12**, 37–43 (2018). https://doi.org/10.1016/j.ensm.2017.11.008
329. He, H., Sun, D., Zhang, Q., et al.: Iron-doped cauliflower-like rutile TiO_2 with superior sodium storage properties. ACS Appl. Mater. Interfaces. **9**, 6093–6103 (2017). https://doi.org/10.1021/acsami.6b15516
330. He, H., Huang, D., Pang, W., et al.: Plasma-induced amorphous shell and deep cation-site S doping endow TiO_2 with extraordinary sodium storage performance. Adv. Mater. **30**, e1801013 (2018). https://doi.org/10.1002/adma.201801013
331. Wu, Y., Liu, X., Yang, Z., et al.: Nitrogen-doped ordered mesoporous anatase TiO_2 nanofibers as anode materials for high performance sodium-ion batteries. Small **12**, 3522–3529 (2016). https://doi.org/10.1002/smll.201600606
332. Usui, H., Yoshioka, S., Wasada, K., et al.: Nb-doped rutile TiO_2: a potential anode material for Na-ion battery. ACS Appl. Mater. Interfaces. **7**, 6567–6573 (2015). https://doi.org/10.1021/am508670z
333. He, H., Zhang, Q., Wang, H., et al.: Defect-rich $TiO_{2-\delta}$ nanocrystals confined in a mooncake-shaped porous carbon matrix as an advanced Na ion battery anode. J. Power Sources **354**, 179–188 (2017). https://doi.org/10.1016/j.jpowsour.2017.04.035
334. Wu, Y., Jiang, Y., Shi, J., et al.: Multichannel porous TiO_2 hollow nanofibers with rich oxygen vacancies and high grain boundary density enabling superior sodium storage performance. Small (2017). https://doi.org/10.1002/smll.201700129
335. Xu, Y., Zhou, M., Wang, X., et al.: Enhancement of sodium ion battery performance enabled by oxygen vacancies. Angew. Chem. Int. Ed. Engl. **54**, 8768–8771 (2015). https://doi.org/10.1002/anie.201503477
336. Er, D., Detsi, E., Kumar, H., et al.: Defective graphene and graphene allotropes as high-capacity anode materials for Mg ion batteries. ACS Energy Lett. **1**, 638–645 (2016). https://doi.org/10.1021/acsenergylett.6b00308
337. Bo, S.-H., Grey, C.P., Khalifah, P.G.: Defect-tolerant diffusion channels for Mg^{2+} ions in ribbon-type borates: structural insights into potential battery cathodes $MgVBO_4$ and $Mg_xFe_{2-x}B_2O_5$. Chem. Mater. **27**, 4630–4639 (2015). https://doi.org/10.1021/acs.chemmater.5b01040
338. Shan, P., Gu, Y., Yang, L., et al.: Olivine $FePO_4$ cathode material for rechargeable Mg-ion batteries. Inorg. Chem. **56**, 13411–13416 (2017). https://doi.org/10.1021/acs.inorgchem.7b02150
339. Wang, Y., Xue, X., Liu, P., et al.: Atomic substitution enabled synthesis of vacancy-rich two-dimensional black TiO_{2-x} nanoflakes for high-performance rechargeable magnesium batteries. ACS Nano **12**, 12492–12502 (2018). https://doi.org/10.1021/acsnano.8b06917
340. Koketsu, T., Ma, J., Morgan, B.J., et al.: Reversible magnesium and aluminium ions insertion in cation-deficient anatase TiO_2. Nat. Mater. **16**, 1142–1148 (2017). https://doi.org/10.1038/nmat4976
341. He, Y.J., Peng, J.F., Chu, W., et al.: Black mesoporous anatase TiO_2 nanoleaves: a high capacity and high rate anode for aqueous Al-ion batteries. J. Mater. Chem. A **2**, 1721–1731 (2014). https://doi.org/10.1039/c3ta13906a
342. Li, H., Chen, Z., Tsang, C.K., et al.: Electrochemical doping of anatase TiO_2 in organic electrolytes for high-performance supercapacitors and photocatalysts. J. Mater. Chem. A **2**, 229–236 (2014). https://doi.org/10.1039/C3TA13963H
343. Lu, X., Wang, G., Zhai, T., et al.: Hydrogenated TiO_2 nanotube arrays for supercapacitors. Nano Lett. **12**, 1690–1696 (2012). https://doi.org/10.1021/nl300173j
344. Zhou, H., Zhang, Y.: Electrochemically self-doped TiO_2 nanotube arrays for supercapacitors. J. Phys. Chem. C **118**, 5626–5636 (2014). https://doi.org/10.1021/jp4082883
345. Kim, C., Kim, S., Hong, S.P., et al.: Effect of doping level of colored TiO_2 nanotube arrays fabricated by electrochemical self-doping on electrochemical properties. Phys. Chem. Chem. Phys. **18**, 14370–14375 (2016). https://doi.org/10.1039/c6cp01799a
346. Salari, M., Konstantinov, K., Liu, H.K.: Enhancement of the capacitance in TiO_2 nanotubes through controlled introduction of oxygen vacancies. J. Mater. Chem. **21**, 5128 (2011). https://doi.org/10.1039/c0jm04085a
347. Lu, X., Zeng, Y., Yu, M., et al.: Oxygen-deficient hematite nanorods as high-performance and novel negative electrodes for flexible asymmetric supercapacitors. Adv. Mater. **26**, 3148–3155 (2014). https://doi.org/10.1002/adma.201305851
348. Zhou, H., Zhang, Y.: Enhancing the capacitance of TiO_2 nanotube arrays by a facile cathodic reduction process. J. Power Sources **239**, 128–131 (2013). https://doi.org/10.1016/j.jpowsour.2013.03.114

Zhong Su is a Ph.D. candidate in the Centre for Clean Environment and Energy, the School of Environment and Science at Griffith University, Australia. Zhong was awarded his master degree and bachelor degree from Jiangsu Normal University, China in 2017 and 2014, respectively. In 2016, Zhong conducted one-year research on lithium-ion batteries as a visiting scholar at Griffith University. His research interests focus on high-energy-density Li–S batteries, high-power-density Li–I_2 batteries and design of defective oxide electrode materials.

Jiahua Liu received his Bachelor's degree in 2017 from the School of Materials Science and Engineering, Nanchang University, China. He is now a graduate student in the School of Advanced Materials (SAM), Shenzhen Graduate School, Peking University, China, under supervision of Prof. Jiaxin Zheng and Prof. Feng Pan. His research focuses on computational materials and energy materials (battery materials, photoelectric materials).

Meng Li obtained his Bachelor's degree from Beihang University in 2011 and his Master's degree in Engineering from China University of Mining and Technology in 2015. Since 2018, he has been studied theoretical and computational aspects of energy storage materials and devices as a Ph.D. candidate at Griffith University, Australia. His research interest lies in the study of electrode materials for Li and Na rechargeable batteries using computational tools.

Yuxuan Zhu received her master degree in Chemistry from Jiangsu Normal University in 2017. She is currently a Ph.D. candidate at the School of Environment and Science, Griffith University, Australia. Her research focuses on ultrahigh-resolution 3D printing technology for rechargeable batteries.

Shangshu Qian received his Bachelor and Master degrees in Chemistry from Ningbo University in 2015 and 2018, respectively. The work includes the development of new anode materials for lithium-ion batteries and the exploration of the mechanism of lithiation/delithiation. He obtained a Ph.D. scholarship from Griffith University in 2019. His main research interests are developing novel polymer-based electrolytes and their composites with ceramic-based electrolytes for solid-state batteries.

Mouyi Weng is currently a Ph.D. candidate in Prof. Feng Pan's group at Shenzhen Graduate School, Peking University, China. He received his B.S. degree from Tsinghua University in 2015. His research interests include computational materials, materials simulation algorithms and electronic structure calculation in materials.

Prof. Jiaxin Zheng received his B.Sc. degree in Physics in 2008 and Ph.D. degree in Condensed Matter Physics in 2013 from Peking University, China. Then, he joined the group of Prof. Feng Pan at the School of Advanced Materials (SAM), Shenzhen Graduate School, Peking University, China, as a postdoctoral fellow from October 2013 to October 2015. His research interests include computational materials, energy materials (battery materials, solar energy, thermoelectric materials), nanomaterials and nanoelectronics. Dr. Zheng has authored and co-authored more than 80 peer-reviewed research articles.

Dr. Yulin Zhong completed his Ph.D. in Chemistry (2010) at the National University of Singapore (NUS) and did his postdoctoral trainings at Princeton University, Massachusetts Institute of Technology and Monash University. He was awarded an ARC DECRA Fellowship in 2014 and joined Griffith University as a Senior Lecturer since 2016. His research interests include electrochemical production of 2D nanomaterials, 3D printing, smart windows and wearable devices.

Prof. Feng Pan National 1000-plan Professor, Founding Dean of School of Advanced Materials, Peking University Shenzhen Graduate School, Director of National Center of Electric Vehicle Power Battery and Materials for International Research, got B.S. from Dept. Chemistry, Peking University in 1985 and Ph.D. from Department of P&A Chemistry, University of Strathclyde, Glasgow, UK, with "Patrick D. Ritchie Prize" for the best Ph.D. in 1994. With more than a decade experience in large international incorporations, Prof. Pan has been engaged in fundamental research and product development of novel optoelectronic and energy storage materials and devices. As Chief Scientist, Prof. Pan led 8 entities in Shenzhen to win the 150 million RMB grant for the national new energy vehicles (power batteries) innovation project from 2013 to end of 2015. As Chief Scientist, Prof. Pan led 12 entities to win the national key project of material genomic engineering for solid state Li-ion batteries in China in 2016.

Prof. Shanqing Zhang obtained his Ph.D. degree in Electrochemistry in 2001 at Griffith University, Australia. Since then, he has been working on the synthesis, modification and characterization of nanostructured materials for sensing, energy conversion and energy storage devices. He has developed a series of patented and commercialized nanotechnologies for environmental monitoring based on functional nanomaterials. He was awarded as an Australia Research Council Future Fellow for the period of 2009–2013. Currently, he is leading his group conducting research on the synthesis of functional nanomaterials and functional polymers for lithium-ion batteries, sodium-ion batteries, supercapacitors and all solid-state lithium-ion batteries.